Title

Exploring Intermolecular Interactions with the Scanning Tunneling Microscope

Author

Han, Zhumin

Publication Date

2016

UNIVERSITY OF CALIFORNIA,
IRVINE

Exploring Intermolecular Interactions with the Scanning Tunneling Microscope

DISSERTATION

submitted in partial satisfaction of the requirements
for the degree of

DOCTOR OF PHILOSOPHY

in Physics

by

Zhumin Han

Dissertation Committee:
Professor Wilson Ho, Chair
Professor Ruqian Wu
Professor Philip G. Collins

2016

DEDICATION

To

My parents and Jiajia

TABLE OF CONTENTS

LIST OF FIGURES

LIST OF TABLES

ACKNOWLEDGMENTS

Foremost, I would like to express the greatest gratitude to my research advisor Professor Wilson Ho for his guidance, encouragement and support. I appreciate the great opportunity to perform frontier surface science research with the state-of-the-art scanning tunneling microscopes developed in the Ho group. I have been deeply impressed by his dedication to research and greatly benefited from his high standards of excellence. Additionally I want to thank Wilson for the trust and support he gave me to design and construct the helium liquefiers. In retrospect, that has become a rewarding experience for me to learn how to develop a large scientific instrument from scratch.

I would like to thank my committee members, Professor Ruqian Wu and Professor Philip G. Collins for their advice and encouragement. I would also like to thank Professor Ilya N. Krivorotov and Professor Reginald M. Penner for serving on my advancement committee.

Special thanks go to a few of Ho group members with whom I worked most closely during my Ph.D. studies. Freddy Toledo taught me the art of machining, construction of the microscope and operation of ultra-high vacuum instruments. Chi-lun Chiang and Chen Xu, taught me a lot about the mK STM system and also helped me construct and test the helium liquefiers from the very beginning to the final product. It was an enjoyable experience to work these people both in the lab and the machine shop. My partner Greg Czap was always available for discussion and willing to offer help. His positivity helped me through my most frustrated days.

I am fortunate to work with my wonderful colleagues and friends in the Ho group. Calvin Patel has broad interests about everything. Shaowei Li always has many ideas about experiments and instruments. I enjoyed stimulating discussions with them which provided me with lots of valuable inspiration. I want to thank Arthur Yu who shared the long journeys with me to two conferences and Weicai Cao who brought cheer and laughter to the lab. Many thanks go to Dr. Ungdon Ham, Dr. Qing Huan, Dr. Haigang Zhang, Dr. Hikari Kimura and Dr. Ying Jiang who offered me ample help and advice concerning electronics and experiments. I want to thank Han Kyu Lee, Likun Wang, Jiang Yao, Siyu Chen, Peter Wagner, Christian Kim and Dr. Wei Tao for their help and friendship.

I would also like to thank Dr. Dingwang Yuan, Dr. Jun Hu, Dr. Xinyuan Wei, Dr. Yanxing Zhang and Dr. Yuan You in Professor Ruqian Wu's group who carried out the density functional calculation for our experiments.

I would like to give special thanks to our robust home-built helium liquefiers for the steady production of liquid helium to support our experiments.

I gratefully appreciate the support for this work by the Chemical Sciences, Geo- and Bioscience Division, Office of Science, U.S. Department of Energy, under grant number DE-FG02-04ER15595.

Finally, I am greatly indebted to my parents and my wife Jiajia for their endless support, comfort and love. Without them, none of this work would have been possible.

CURRICULUM VITAE

Zhumin Han

Department of Physics & Astronomy
University of California, Irvine — Phone: 949-824-3492
4129 Frederick Reines Hall, Irvine, CA 92697 — Email: zhan@uci.edu

EDUCATION

University of California, Irvine, USA

Ph.D. in Physics — Sep. 2016

Thesis Advisor: Prof. Wilson Ho

M.S. in Physics — Dec. 2009

University of Science and Technology of China, China

B.S. in Applied Physics — July 2008

RESEARCH EXPERIENCE

University of California, Irvine - Department of Physics and Astronomy

Graduate Student Researcher — July 2009 - Present

Advisor: Prof. Wilson Ho

- Led the Helium Recycling and Liquefaction Project. Designed, constructed and tested helium purification and liquefaction hardware and software, developed the construction strategy and operating procedures. Highlighted in *Chemical & Engineering News*.
- Developed a new scanning probe microscopy technique, inelastic tunneling probe (itProbe). Visualization of the inter- and intra-molecular bonding structure with sub-Ångström spatial resolution by scanning tunneling microscope (STM). Highlighted in *UC Irvine News*, *Chemistry World* and *Microscopy and Analysis.*
- Studied non-covalent intermolecular interactions in molecular self-assemblies with itProbe, involving hydrogen bonds, halogen bonds, electrostatic and van der Waals interactions.
- Precise structural imaging of physisorbed benzene molecules on an inert metal surface, characterized the weak molecule-metal bonding by measuring the external vibrational modes by inelastic electron tunneling spectroscopy (IETS).
- Studied the intermolecular interactions through the detection of coupled vibrational modes with STM-IETS.
- Developed and implemented data processing and analysis programs.

- Designed and constructed ultra-high vacuum rated scientific instruments, including a radio frequency (up to 1.5 GHz) STM along with associated control software, e-beam sample heater, gas handling systems, metal and molecular thermal evaporators.

University of Science and Technology of China - Department of Physics
Undergraduate Research Assistant Apr. 2007 - July 2008
Advisor: Prof. Lixin He

- First principles calculation of the electronic structures of self-assembled InAs/InP and InAs/GaAs semiconductor quantum dots.

PUBLICATIONS

[12] **Z. Han**, *et al.* “The Interplay of Molecular Geometry, Vibration and Conductance in a Hybrid Molecular Junction”, in preparation (2016).

[11] **Z. Han**, *et al.* “Organizational Chirality Identification of Two-dimensional Self-assembled Molecular Structures by Domain Boundaries”, in preparation (2016).

[10] **Z. Han**, *et al.* “Development of a 55 L/day Helium Liquefaction System with Two Gifford-McMahon Cryocoolers”, in preparation (2016).

[9] **Z. Han**, *et al.* “Three-dimensional Imaging of a Single Molecule with sub-Ångström Resolution by the Inelastic Tunneling Probe”, in preparation (2016).

[8] **Z. Han**, *et al.* “Imaging Halogen Bond: Self-assembly of Hexahalogenbenzene”, *Science*, submitted (2016).

[7] **Z. Han**, *et al.* “Probing Intermolecular Coupled Vibrations by STM Inelastic Electron Tunneling Spectroscopy”, in preparation (2016).

[6] **Z. Han**, X. Wei, C. Xu, C. Chiang, Y. Zhang, R. Wu, and W. Ho “Imaging van der Waals Interactions”, *J. Am. Chem. Soc.*, submitted (2016).

[5] D. Yuan*, **Z. Han***, G. Czap, C. Chiang, C. Xu, W. Ho, and R. Wu “Quantitative Understanding of van der Waals Interactions by Analyzing the Adsorption Structure and Low-Frequency Vibrational Modes of Single Benzene Molecules on Silver”, *J. Phys. Chem. Lett.***7**, 2228-2233 (2016).

[4] C. Xu, C. Chiang, **Z. Han** and W. Ho “Nature of Asymmetry in the Vibrational Line Shape of Single-Molecule Inelastic Electron Tunneling Spectroscopy with the STM”, *Phys. Rev. Lett.* **116**, 166101 (2016).

[3] H. Wang, S. Li, H. He, A. Yu, F. Toledo, **Z. Han**, W. Ho, and R. Wu “The Trapping and Characterization of a Single Hydrogen Molecule in a Continuously Tunable Nanocavity”, *J. Phys. Chem. Lett.* **6**, 3453-3457 (2015).

[2] C. Chiang*, C. Xu*, **Z. Han*** and W. Ho “Real-space Imaging of Molecular Structure and Chemical Bonding by Single-molecule Inelastic Tunneling Probe”, *Science* **344**, 885-888 (2014).

[1] S. Li, A. Yu, F. Toledo, **Z. Han**, H. Wang, H. He, R. Wu and W. Ho "Rotational and Vibrational Excitations of a Hydrogen Molecule Trapped within a Nanocavity of Tunable Dimension", *Phys. Rev. Lett.* **111**, 146102 (2013).
* Equal Contribution

PRESENTATIONS

- 76th Physical Electronics Conference, Fayetteville, AR June 2016
  "Exploring Intermolecular Interactions by Imaging Single Bonds with the Scanning Tunneling Microscope"
- SCSMM Full-Day Symposium, Irvine, CA Apr. 2016
  "Imaging Intermolecular Interactions"
- ACS Western Regional Meeting, San Marcos, CA Nov. 2015
  "Probing Intermolecular Coupled Vibration by STM Inelastic Electron Tunneling Spectroscopy"
- 2014 APS March Meeting, Denver, CO Mar. 2014
  "Real-Space Imaging of Molecular Structure by Single-Molecule Inelastic Tunneling Probe"

HONORS & AWARDS

First Place Platform Presentation, SCSMM Symposium	Apr. 2016
Marco Vekic Memorial Award, UC Irvine	May 2010
Regents' Fellowship, UC Irvine	2008 - 2010
Outstanding Student Scholarship, USTC	2004 - 2008

ABSTRACT OF THE DISSERTATION

Exploring Intermolecular Interactions with the Scanning Tunneling Microscope

By

Zhumin Han

Doctor of Philosophy in Physics

University of California, Irvine, 2016

Professor Wilson Ho, Chair

Compared to intramolecular interactions, intermolecular interactions are relatively weak but they lay the foundation for research involving molecular recognition, self-assembly and surface adsorption in chemical and physical systems. This dissertation describes three different experimental approaches based on the detection of molecular vibrations to provide direct insights into intermolecular interactions at the sub-Ångström spatial resolution with a home built sub-Kelvin scanning tunneling microscope (STM).

First, the intermolecular interaction can be evaluated by measuring the coupled vibrational mode of two interacting molecules with STM inelastic electron tunneling spectroscopy (IETS). The measurement of intermolecular coupled vibrations with tunable vertical and lateral displacements offers a direct assessment of the short range intermolecular repulsion in three dimensions.

Second, the self-assembled molecular bonding structures can be imaged by the inelastic tunneling probe (itProbe). In itProbe, a carbon monoxide (CO) molecule is transferred onto the STM tip. The hindered translation energy of the CO-tip varies when it is positioned over different locations of the self-assembled structures. By recording the

intensity variations of the inelastic electron tunneling signal caused by the energy shift, the geometric structure of each molecule and intermolecular interactions can be imaged in real space.

Third, a sample surface can be considered as a giant molecule with infinite mass, and the binding strength of an adsorbed molecule on the surface is reflected in the external vibrations. The combination of the itProbe and IETS enable the determination of the adsorption configuration and low energy external vibrational modes of individual physisorbed benzene on an inert metal for the first time.

All the approaches mentioned above rely on resolving fine spectral features induced by intermolecular interactions. The unprecedented spectral sensitivity, energy resolution and thermal stability achieved in 600 mK create the opportunity to study these weak intermolecular interaction effects at the single molecule level, which are otherwise obscured at higher temperatures.

Chapter 1

Introduction

1.1 Background and Motivation

Intermolecular interactions are of fundamental importance to our understanding of various physical and chemical phenomena, such as molecular recognition, self-assembly, heterogeneous catalysis and surface adsorption. Vibrations of a molecule reflect its chemical bonding structure and its coupling with the surrounding environment, which in turn can be used as a probe to characterize the intramolecular and intermolecular interactions.

Measurements of intermolecular interaction at the single molecule level are highly desirable not only to facilitate direct comparison with theoretical calculations but also to reveal the rich local information which is otherwise hidden upon averaging in ensemble measurements, such as the molecular structure, orientation and coupling to the neighboring environment.

The scanning tunneling microscope (STM), which is capable of resolving single molecules and atoms on surfaces, provides a great opportunity to study chemistry at a single molecule level [1]. This year marks the 35th anniversary of STM. Ever since its invention by Binnig and Rohrer [2,3], STM has become a versatile tool to explore the "*Plenty of Room at the Bottom*" [4]. It has shown its capability not only to explore the local electronic structures of surfaces and molecules [5–7], but also to manipulate the atoms and molecules to create artificial structures [8–10]. Furthermore, the detection single molecule vibration excitation by inelastic electron tunneling spectroscopy (IETS) [11] in addition to the selective chemical bond formation [12–14] and dissociation [14,15] by tunneling electrons demonstrated the chemical sensitivity of STM and its application to surface catalytic analysis. Moreover, by choosing different tip materials (such as spin-polarized tips [16] and superconducting tips [17]) and coupling external fields to the tunneling junction (such as magnetic field [18], laser [6,19] and microwave [20,21]) have further broadened the applications of STM to study the magnetic and optical phenomena as well as their dynamics down to the atomic scale.

In principle, molecular vibrations which contain information about the intermolecular interaction can be characterized with STM-IETS down to the single molecule level. However, intermolecular interaction induced vibrational features are expected to be rather weak due to the weak non-covalent nature of the interaction. Benefiting from the unprecedented energy resolution and thermal stability achieved in 600 mK experimental temperature, these subtle intermolecular effects, such as shifts of vibrational energies and new coupled vibrational modes, become accessible from single molecule STM measurements as described in this dissertation.

Despite the great success of STM as a versatile tool for providing local electric, magnetic, vibrational and optical properties of a molecule on surface, the images of these properties are strongly correlated to the electron density distribution which is often not easily related to the geometric structure of the molecule. It is desired to image these structures directly in an attempt to clarify the relationship between structures and functions. Fortunately, the use of a molecule functionalized tip as the probe has been demonstrated to obtain this information in a few recently developed techniques.

With a carbon monoxide (CO) molecule attached on the tip, non-contact atomic force microscope (nc-AFM) has been used to resolve the covalent bonding structure of a single molecule [22,23] on a surface. Moreover, it has been applied to study hydrogen bonding networks in molecular clusters [24,25] and reveal surface chemical reaction mechanisms by imaging the reactant and products [26,27]. Atomic resolution within a molecule has also been achieved with scanning tunneling hydrogen microscopy (STHM), in which a CO, Xe, CH_4, or H_2 molecule is trapped in the tunneling junction acting as a force-to-current transducer [28–31].

Furthermore, inelastic tunneling probe (itProbe) was introduced to image the geometric structure of an adsorbed molecule on a surface with the inelastic electron tunneling features of the CO-tip as the probe [32]. As will be discussed in the later chapters, the application of itProbe to study self-assembled molecules on surfaces leads to a deeper understanding of the intermolecular bonding structure of the self-assembly and the mechanism of the itProbe technique itself.

1.2 Basic Principles of an STM

Electron tunneling is a quantum mechanical phenomenon resulting from the wave-particle nature of the electron. An electron has a finite probability to tunnel through an energy barrier which is forbidden classically. In STM, if we apply a bias voltage, V, from sample to tip, according to Bardeen approximation [33], the tunneling current can be written as

$$\begin{aligned} I = \frac{4\pi e}{\hbar} \int_{-\infty}^{\infty} & [f(E_F - eV + \varepsilon) - f(E_F + \varepsilon)] \\ & \times \rho_T(E_F - eV + \varepsilon) \rho_S(E_F + \varepsilon) |M_{TS}|^2 d\varepsilon, \end{aligned} \tag{1.1}$$

where E_F is the Fermi level of the sample; $f(\varepsilon)$ is the Fermi distribution function; $\rho_T(\varepsilon)$ and $\rho_S(\varepsilon)$ are the density of states (DOS) of the tip and the sample; M_{TS} is the tunneling matrix element which describes the spatial overlap between the tip and sample states.

Eq. 1.1 can be greatly simplified based on a few assumptions for the energy window of interest. 1. The DOS of the tip and sample have smooth variation in energy compared to $k_B T$. 2. The tunneling matrix is independent of energy level. 3. The tip has flat DOS is near the Fermi level, such as silver tip. 4. The tip state is spherically symmetric in space (s-wave).

$$I \approx \frac{4\pi e}{\hbar} \rho_T(E_F) |M_{TS}|^2 \int_0^{eV} \rho_S(E_F + \varepsilon) d\varepsilon. \tag{1.2}$$

According to Tersoff and Hamann's derivation for an s-wave tip [34,35], the tunneling matrix element M_{TS} is proportional to the sample wave function at the center of curvature of the tip $\vec{r_0}$, so that

$$M_{TS} \propto \psi_S(\vec{r_0}). \tag{1.3}$$

Finally, the tunneling current becomes

$$I \propto |\psi_S(\overrightarrow{r_0})|^2 \int_0^{eV} \rho_S(E_F + \varepsilon)d\varepsilon. \qquad (1.4)$$

The differential conductance of the tunneling junction is given by

$$\left.\frac{dI}{dV}\right|_{V=V_0} \propto |\psi_S(\overrightarrow{r_0})|^2 \rho_S(E_F + eV_0) \equiv \widetilde{\rho_S}(E_F + eV_0, \overrightarrow{r_0}), \qquad (1.5)$$

which is defined as the local density of states (LDOS) of the sample at the center of curvature of the tip for the given energy level.

Eq. 1.4 (Eq. 1.5) shows the tunneling current (conductance) as a function of tip position $\overrightarrow{r_0}$. The sample wavefunction $|\psi_S(\overrightarrow{r_0})|^2$ exponentially decays through the vacuum junction which leads to the exponential dependency of current (conductance) on the tip-sample distance. Typically the tunneling current increases by one order of magnitude for every Ångström reduction of the tip-sample distance. This essential property gives rise to the sub-Ångström spatial resolution achieved in the STM.

More importantly, differential conductance of the tunneling junction directly reflects the local electronic structure of the sample which leads to a scanning probe technique called scanning tunneling spectroscopy (STS). STS [*dI/dV* versus *V*] can be conducted to reveal the energy levels of the sample electronic states with sub-Ångström resolution. In addition, scanning the tip over the sample and recording the conductance at a certain bias leads to the visualization of the electronic states or charge density distribution at the given energy level in real space [5–7,9].

The capability to perform inelastic electron tunneling spectroscopy (IETS) [11] with the STM further extends its spectroscopic sensitivity to characterize excitations of matter. In a biased tunneling junction as illustrated in Fig. 1.1A, the electron can elastically tunnel through the vacuum barrier without losing energy which creates a straight line in *I-V* spectrum if we assume constant DOS for the tip and sample near the Fermi level. When the bias reaches a threshold ħω/e required to excite a vibrational mode, the electron gains the ability to excite the vibration and inelastically tunnel through the junction as the blue arrow indicates. The opening of the inelastic tunneling channel is accompanied with a step-like increase of conductance and a kink for the current at the threshold bias for both polarities.

The change in the current (*I*) and conductance (*dI/dV*) may be very small, so we need a lock-in amplifier to detect such small features by looking at the differential change of the conductance as a function of sample bias (d^2I/dV^2). As shown in Fig. 1.1B, the sample bias is modulated with $\sqrt{2}V_M\mathrm{Sin}(\omega_0 t)$ from the lock-in amplifier in addition to the DC voltage and the tunneling current $I[V+\sqrt{2}V_M\mathrm{Sin}(\omega_0 t)]$ is fed into the lock-in. It can be shown that the first and second harmonics from the lock-in amplifier are proportional to *dI/dV* and d^2I/dV^2 respectively from Taylor expansion. The resultant d^2I/dV^2 spectrum features a pair of peaks with opposite polarities for opposite sample bias at the threshold voltage as shown in Fig. 1.1E. The relative change of conductance $\Delta\sigma/\sigma_0$ can be used to characterize the STM-IETS cross-section for a specific excitation process.

The apparent peak width W observed in the d^2I/dV^2 spectrum is determined by the intrinsic width W_I and the extrinsic broadenings which include the thermal broadening W_T and modulation broadening W_M. This can be written as

$$W^2 = W_I^2 + W_T^2 + W_M^2. \tag{1.6}$$

The intrinsic width is associated with the lifetime of the excitation itself. The thermal broadening is related to the thermal smearing of electron distribution described by the

Fermi distribution and is given by $W_T = 5.4\ k_B T$ [36]. The modulation broadening is caused by the finite modulation amplitude used for lock-in detection and is formulated by $W_M = 1.7\ V_M$ [37], where V_M is the root mean square (RMS) value of the sinusoidal modulation.

By reducing the experimental temperature down to 600 mK, the thermal broadening is effectively reduced to 0.3 meV compared to 5 meV at 10 K. Additionally, lower temperature also decreases the thermal noise in the tunneling current. Thus smaller modulation amplitude is required to obtain a decent signal to noise ratio which decreases the modulation broadening. By combining these two factors, the extrinsic broadenings are greatly suppressed at 600 mK which leads to an overall energy resolution of 0.6 meV achieved in our STM-IETS measurement.

1.3 Imaging Molecular Bonding Structures

The imaging of the molecular bonding structures with atomic resolution highlights the one of the most exciting achievements in the scanning probe community over the last decade. Here I will briefly discuss the development of the itProbe technique and compare with other aforementioned high-resolution scanning probe techniques including nc-AFM and STHM.

High energy resolution STM-IETS indicates significant energy shifts for the low energy vibrations of CO molecule on surfaces [38,39]. Especially for the CO hindered translational (HT) mode, the vibrational energy of CO on Au(110) and Cu(100) surface varies more than 50% within 1.5 Å travel of the tip-sample distance [38]. This indicates that the CO vibration is very sensitive to coupling with the local environment, which in turn can be used as a probe to reveal the corrugation of this coupling over space.

This observation led to the development of itProbe technique in 2013. A CO molecule is transferred on the tip in the experiment. When the CO-tip is placed over different locations of a cobalt phthalocyanine (CoPc) molecule on Ag(110) surface, the vibrational energy of the CO-tip HT mode varies from 1.2 meV to 3.2 meV. By mapping the variation of d^2I/dV^2 intensity caused by the CO HT energy shift, the geometric structure of the CoPc molecule is visualized in the real space [32].

Later we have applied this technique to image a few other organic molecules on surface, including both cyclic and acyclic molecules as shown in Fig. 1.2. All covalent bonds inside these molecules are highlighted with ~ 0.1 Å spatial resolutions. As will be shown in Chapter 3 to Chapter 5, the HT mode of the CO-tip can be modeled as a simple harmonic oscillator and its vibrational energy is determined by the curvature of its vibrational potential well. The interaction between the CO-tip and the surface molecule leads to a corrugated potential energy surface (PES) that modifies the CO vibrational well differently at different sites. Specifically, over the bonds and atom positions inside the molecule are associated with a positive local curvature in the PES that reduces the overall curvature of the CO vibrational well and causes a redshift of CO vibrational energy, whereas the negative PES curvature inside a carbon ring blueshifts the CO HT energy. Therefore by imaging the of d^2I/dV^2 intensity at a reduced energy from background, we can highlight the atom and bond locations.

In a nc-AFM equipped with a q-Plus sensor [40], the tip is mounted on a quartz tuning fork and oscillates at the resonant frequency (20-30 kHz) with a constant amplitude. The interaction between the tip and sample causes shifts of the oscillation frequency Δf on the order of a few Hz. The quartz tuning fork with high spring constant (~1800 N/m) allows the AFM to work with small oscillation down to 0.2 Å which greatly enhances its sensitivity to short range forces. For small oscillation amplitude, Δf is proportional to the tip-sample force gradient in the tip oscillation direction to a good approximation. Besides the conventional AFM that tip oscillates normal to the surface, lateral force microscopy (LFM) [41] is also available to detect the forces parallel to the surface.

To make an analogy of itProbe with AFM, the itProbe acts like a “self-adaptive” LFM as shown in Chapter 5. The itProbe technique employs the CO HT vibration as a microscopic force sensor that oscillates with much smaller amplitude and higher frequency compared to an nc-AFM. In addition, the relative frequency shifts due to tip-sample interaction in itProbe are also much higher than nc-AFM. The long range attractive forces between the tip and metal substrate are embedded in the nc-AFM measurement while this type of long range interaction is essentially absent for itProbe as well as LFM. Furthermore, instead of providing the lateral force gradient only along the tip oscillation direction, itProbe reflects the local lateral curvature of the PES as the CO HT always relaxes and oscillates along the principal axes of the PES which will be discussed more in Chapter 5.

In STHM, the tip is held at constant height and differential conductance (dI/dV) is imaged with a molecule decorated tip at a fixed sample bias [29]. Compared with itProbe, both techniques transform the interaction between the probe molecule and the adsorbates to a detectable quantity. While the biggest difference between STHM and itProbe is that the latter one provides higher energy resolution. As will be shown in Chapter 5, d^2I/dV^2 images can provide higher spatial resolution to reveal more subtle structures caused by the intermolecular PES. The differential conductance dI/dV imaging is less energy sensitive than d^2I/dV^2 imaging because dI/dV can be considered as an integration of d^2I/dV^2 from the imaging bias to Fermi level, but not all d^2I/dV^2 at different sample biases (energies) have good spatial contrast [32].

The use of a CO-tip plays a crucial role for the sharp resolution achieved among these techniques. The high resolution has been interpreted as arising from the short range Pauli repulsion from the closed shell of the CO molecule interacted with underlying molecules [22,42]. Thus the higher electron density regions where the chemical bonds locate will result in stronger repulsive forces. Furthermore, the CO tilting on the tip sharpens the image [23,43]. Hapala *et al.* developed a simple mechanical model [43,44] that successfully described the main features observed in q-Plus AFM and itProbe images. In the model, the interaction between the decorated tip (the probe) and underneath molecule is modeled as sum of pairwise Lennard-Jones potentials between the probe atom and individual atoms in the molecule. In other words, the interaction is centered on each atom in the molecule instead of the electron density accumulated regions according to covalent bonding structure or molecular orbital of the molecule. Both models give reasonable agreement with the experimental results of the molecular covalent bonding structures. That’s because the probe molecule CO has comparable size with the separation of two covalently bonded atoms. To distinguish these two models, a “sharper” probe with smaller radius is needed.

The visualization of hydrogen bonds in real space with q-Plus AFM was first reported by Qiu’s group [24]. The linkage between a hydrogen atom and the oxygen atom of two adjacent molecules is described as arising from the enhancement of electron density due to the presence of the hydrogen bond. However, this explanation of sharp contrast of this intermolecular connection has resulted in significant debate. Hapala’s mechanical model suggests that the flexibility of the CO-tip “alone” could also lead to the intermolecular linkage between the hydrogen bonded molecules [43,44] in the sense that no explicit electronic structure information is considered in the model.

Though this model has successfully reproduced most of the intra and intermolecular bonding structure images in the experiment, it must be cautious that the mechanical model relies on the choice of the van der Waals (vdW) parameters. These empirical parameters, such as vdW radius, vary for the same element in different molecules [45]. Although there is no explicit charge distribution expression in this model, the fact that the same element has variable vdW parameters in different molecules indicates these empirical parameters contain the information regarding how that atom is bonded differently with other atoms in different molecules. Or in other words, this model still contains the charge distribution information implicitly, which may overestimate the charge distribution effect outside of the molecule.

1.4 Intermolecular Interactions Probed by Molecular Vibrations

As mentioned above, it is of fundamental interest to study intermolecular interactions at the single molecule level to get a mechanistic understanding of different types of interactions which are involved in various systems.

Let's look at a simple one-dimensional harmonic model first to get some insights into how to measure the intermolecular interaction through the vibration of molecules. If we have two harmonic oscillators, their oscillation frequencies are given by their masses and spring constant, $\omega_{A0} = \sqrt{k_A/m_A}$ and $\omega_{B0} = \sqrt{k_B/m_B}$, where the k_i and m_i $(i = A\ or\ B)$ are the spring constant and mass of each oscillator, respectively. If there is some coupling k between the two oscillators, the vibration modes and energies would be modified. The resultant two vibrational modes can be written as

$$\omega_{\pm}^2 = \frac{1}{2}\left[\omega_A^2 + \omega_B^2 \pm \sqrt{(\omega_A^2 - \omega_B^2)^2 + \frac{4k^2}{m_A m_B}}\right], \tag{1.7}$$

where $\omega_A = \sqrt{(k_A + k)/m_A}$ and $\omega_B = \sqrt{(k_B + k)/m_B}$.

We can think about some special cases. In a strong coupling regime where $k \sim k_A \sim k_B \gg k_A - k_B = \Delta k$ and $m_A = m_B = m$, the two oscillators are coupled and the coupled vibration frequencies become

$$\omega_{\pm}^2 = \begin{cases} \frac{1}{2}(\omega_{A0}^2 + \omega_{B0}^2) + \frac{2k}{m} \\ \frac{1}{2}(\omega_{A0}^2 + \omega_{B0}^2) \end{cases}, \tag{1.8}$$

which correspond to an out-of-phase and in-phase coupled vibration as shown in Fig. 1.3B. The frequency dispersion with the coupling strength k is shown in Fig. 1.3B for a special case where $\Delta k = 0$ ($k_A = k_B \equiv k_0$ and $\omega_{A0} = \omega_{B0} \equiv \sqrt{k_0/m}$). It indicates that the in-phase vibrational energy is independent of the coupling strength whereas the out-of-phase vibrational energy increases as the coupling grows. This suggests that we can use the vibration to characterize the intermolecular interaction. As shown in Chapter 2, a CO-tip is coupled to another CO molecule on surface. Their low energy HT modes can be considered as harmonic oscillators and intermolecular coupled vibrational modes are detected by STM-IETS for the first time.

From Eq. 1.8, we can find that the coupled vibration mode frequency also depends on the individual oscillator frequencies. Thus if ω_{A0} and coupling k are constants, we will be able to map out the variation of ω_{B0} in three-dimensional space by adjusting displacement of the two coupled oscillator and recording the coupling vibration mode. In an on-going experiment, by imaging of the out-of-phase HT mode for the CO-tip on CO system with STM-IETS we are able to reveal the anisotropy of the CO adsorption well on Ag(110) surface.

Now let's consider a weak coupling case, where $k \sim k_A \ll k_B, m_A \ll m_B$ and $\omega_{A0} \ll \omega_{B0}$, Eq. 1.7 now becomes

$$\omega_{\pm} = \begin{cases} \omega_A = (k_A + k)/m_A \\ \omega_B \sim \omega_{B0} \end{cases}, \tag{1.9}$$

which indicates the vibrational frequency of the softer oscillator is greatly modified by the intermolecular coupling while the stiffer oscillator is not affected. This corresponds to the case that we are considering in the itProbe experiment. The CO-tip is the oscillator A and the surface adsorbates are oscillator B. The coupling strength is comparable to the CO HT vibrational mode while much weaker than the internal modes of the surface molecule. Thus the intermolecular interaction between the CO and surface molecule shifts the CO HT energy over different locations of the surface molecule by modifying the effective spring constant. The STM-IETS at 600 mK is sensitive enough to detect such small energy shifts which allow us to obtain atomic resolution of the molecular structure with the itProbe technique.

Self-assembly of molecules provides a promising bottom-up approach to realize molecular electronics with miniature functional units and scalable dimensions. It has attracted such considerable interest that it was listed as one of the top 25 critical questions for *Science*'s 125th anniversary [46]. In order to push the rationally design self-assembled systems of increasing complexity of the chemical self-assembled system and drive the self-assembly in a desired fashion, a deep understanding of molecular interactions ranging from across different length and energy scales are is required.

As mentioned earlier, the itProbe techniques create real-space images of single molecular structure on surfaces with sub-Ångström resolution which provides a great opportunity to extend its application to image the intermolecular bonding networks of self-assembled molecules. Non-covalent intermolecular interactions play a pivotal role in molecular self-assembly. We have studied a few self-assembled molecular systems which involve hydrogen bonding, halogen bonding and van der Waals (vdW) interaction as shown in Fig. 1.4. Rich intermolecular bonding structures are obtained to reveal the mechanism of intermolecular interactions as will be discussed more in later chapters.

Molecules like benzene on coinage metal surfaces have been served as the prototypes for studies of weak chemical bonds. Such a system can be considered as benzene interacting with a giant molecule (the surface) with a huge mass difference. In principle, the coupling between them can be characterized by measuring the low-energy external vibrational modes. However, these modes typically have energies less than 15 meV which make it challenging to detect with conventional ensemble techniques due to the limitation of energy resolution, sensitivity and selection rules. The enhanced spectroscopic resolution and thermal stability achieved at 600 mK enabled the detection of low-energy external vibrations of physisorbed benzene on Ag(110) by STM-IETS. Additionally, it became possible to determine its adsorption site and orientation by the itProbe [47]. Our single molecule measurements lead to an accurate benchmark for the assessment of different DFT methods that incorporate vdW interactions.

1.5 Summary of Contents

This dissertation is devoted to the studies of intermolecular interactions at single molecule level from three different perspectives. All the experiments were performed with a home built STM at 600 mK in ultra-high vacuum. The remaining chapters of this dissertation are self-contained research papers, which have been published, submitted or prepared for publication in a peer-reviewed journal.

Chapter 2: “Probing Intermolecular Coupled Vibrations by STM Inelastic Electron Tunneling Spectroscopy” by Z. Han, G. Czap, C. Xu, C. Chiang, D. Yuan, R. Wu, and W. Ho, prepared for submission to *Physical Review Letters*. This paper describes the detection of an intermolecular coupled vibration between an adsorbed CO molecule on a surface and CO-terminated tip with STM-IETS. With DFT calculation, this mode has been identified as the out-of-phase hindered translational mode of the CO dimer in the tunneling junction. The dependency of the coupled mode energy and IETS intensity on tip-sample distance are discussed.

Chapter 3: “Imaging Halogen Bond: Self-assembly of Hexahalogenbenzene” by Z. Han, G. Czap, C. Chiang, C. Xu, X. Wei, Y. Zhang, R. Wu, and W. Ho, submitted to *Science*. Real-space images of the intermolecular bonding network in the two-dimensional self-assembled hexafluorobenzene (C_6F_6) and hexabromobenzene (C_6Br_6) molecules are obtained with the itProbe technique. The different adsorption behaviors and mechanisms among the fully halogenated benzenes (C_6F_6 and C_6Br_6) and regular benzene (C_6H_6) are discussed.

Chapter 4: “Quantitative Understanding of van der Waals Interactions by Analyzing the Adsorption Structure and Low-Frequency Vibrational Modes of Single Benzene Molecules on Silver” by D. Yuan, Z. Han, G. Czap, C. Chiang, C. Xu, W. Ho, and R. Wu appearing in *The Journal of Physical Chemistry Letters*. This paper describes a combined experimental and theoretical investigation of a physisorbed benzene molecule on Ag(110) surface. The adsorption structure and low energy vibrational modes of the benzene molecule have been characterized with itProbe imaging and STM-IETS which are compared with vdW corrections incorporated DFT calculations. This work demonstrates the capability to quantitatively probe the vdW interactions between a physisorbed molecule and an inert substrate.

Chapter 5: “Three-dimensional Imaging of a Single Molecule with sub-Ångström Resolution by the Inelastic Tunneling Probe” by Z. Han, G. Czap and W. Ho, prepared to be submitted to *Physical Review Letters*. The itProbe technique is applied to image a hexabromobenzene (C_6Br_6) molecule on Ag(110) surface in three-dimensional space. The contrast in the itProbe images is related to the local curvature of the potential energy surface between the CO-tip and C_6Br_6 molecule as illustrated by a mechanical model. This work also demonstrates the unique advantages of itProbe as a miniature self-adaptive lateral force microscopy which is capable to reveal the subtle lateral corrugation of the PES over a wide range of tip-sample distance.

Chapter 6: “Development of a 55 L/day Helium Liquefaction System with Two Gifford-McMahon Cryocoolers” by Z. Han, C. Xu, C. Chiang, A. Yu, G. Czap and W. Ho, prepared to be submitted to *Review of Scientific Instruments*. This paper describes the development of an efficient small scale helium liquefaction system. The system consists of two cryogenic gas purifiers and two helium liquefiers as an integrated system which produces over 55 L of liquid helium per day to support our low temperature STM experiment. The design, operation and performance of the system are addressed.

The final chapter summarizes the dissertation and proposes a few suggestions for future research as well as instrument development.

The appendices describe a LabVIEW software for STM-IETS calibration and a split sample design for transport measurement.

Figure 1.1. Schematic diagrams of the STM-IETS mechanism and measurement setup. (A) Electron tunneling through a STM junction. Green arrow shows the elastic tunneling channel and blue arrow shows the inelastic tunneling channel. (B) Lock-in amplifier setup to detect inelastic electron tunneling signal. (C)-(E) I, dI/dV and d^2I/dV^2 spectra measured from current preamplifier (I) and lock-in amplifier (dI/dV and d^2I/dV^2).

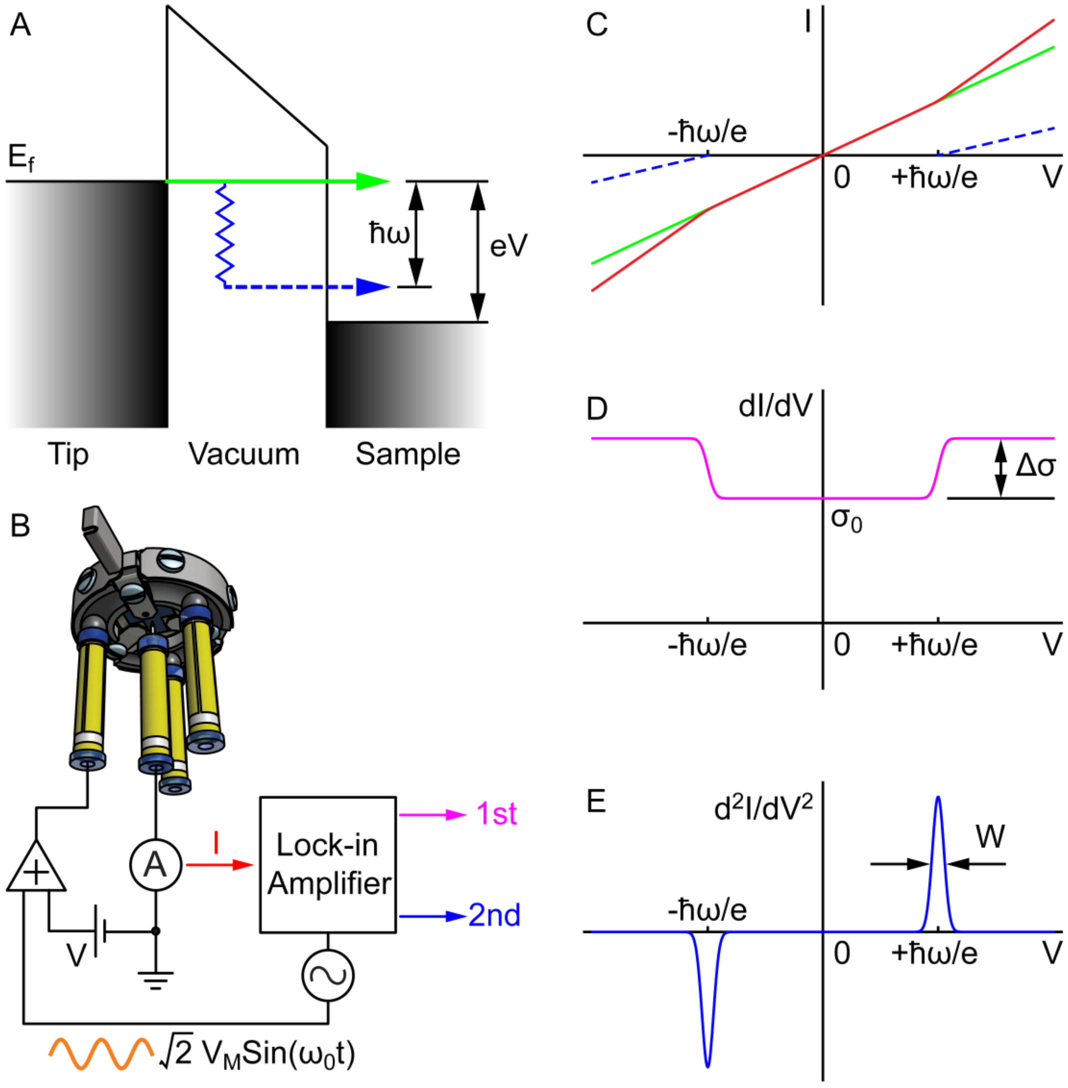
A
E_f
ħω
eV
Tip
Vacuum
Sample
B
Lock-in Amplifier
A
I
V
1st
2nd
√2 V_M Sin(ω_0 t)
C
I
-ħω/e
0
+ħω/e
V
D
dI/dV
Δσ
σ_0
-ħω/e
0
+ħω/e
V
E
d²I/dV²
W
-ħω/e
0
+ħω/e
V

Figure 1.2. Gallery of single organic molecules visualized by itProbe imaging and their structure models. itProbe images are shown in gray scale and the molecular models are displayed below the corresponding itProbe images. These molecules are (A) cobalt phthalocyanine (CoPc), (B) hexabromobenzene (C_6Br_6), (C) 1,3,5,7-cyclooctatetraene (COT, C_8H_8), (D) 1,4-phenylene diisocyanide (PDI), (E) benzene(C_6H_6) and (F) ethylene (C_2H_4).

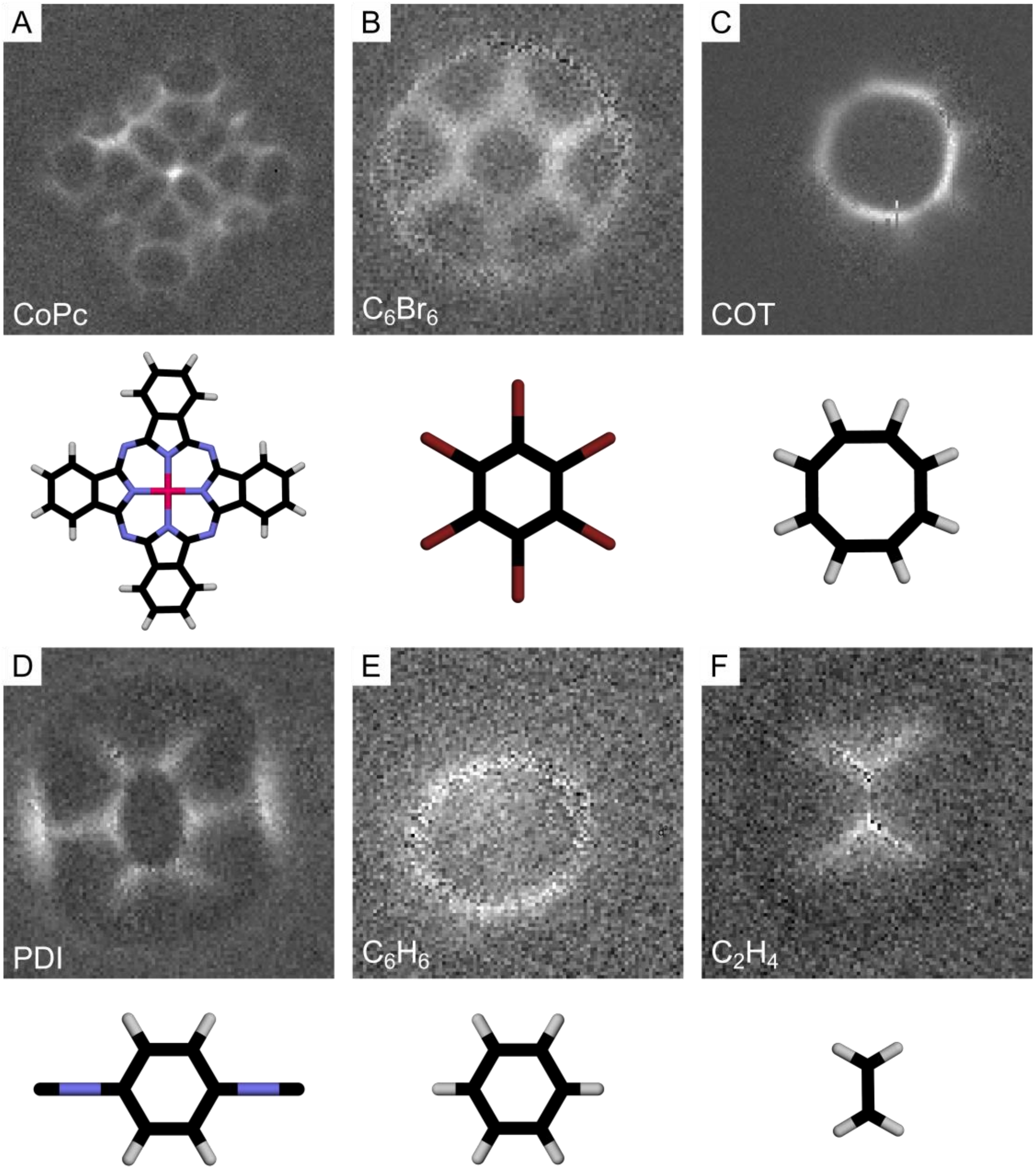
A
CoPc
B
C6Br6
C
COT
D
PDI
E
C6H6
F
C2H4

Figure 1.3. Illustration of one-dimensional coupled harmonic oscillators and coupled vibrational modes. (A) Schematic diagram of one-dimensional coupled harmonic oscillators. (B) Coupled vibrational modes and their energy dependency on the coupling strength for a special case that both oscillators are identical.

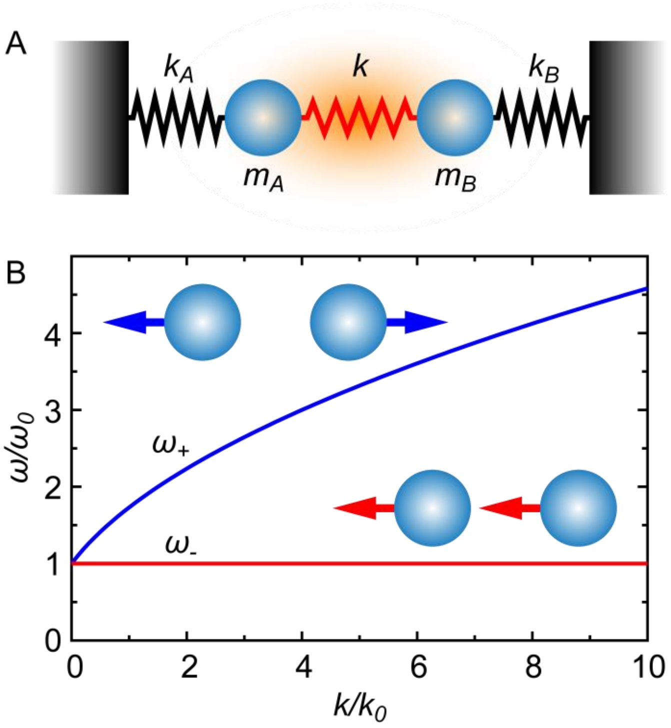
A
k_A
k
k_B
m_A
m_B
B
ω/ω_0
0
1
2
3
4
ω_+
ω_-
0
2
4
6
8
10
k/k_0

Figure 1.4. itProbe images of different molecular self-assemblies on Ag(110).

(A) 1,3-difluorobenzene ($C_6H_4F_2$) island, (B) xenon (Xe) island, (C) hexafluorobenzene (C_6F_6) island and (D) C_6Br_6 trimer.

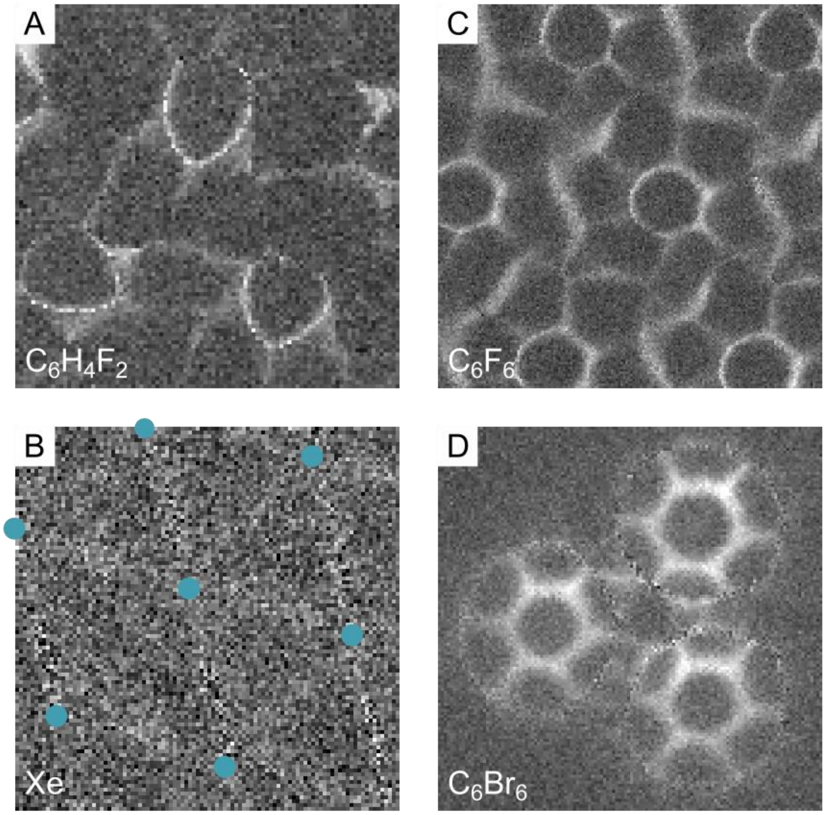
A
$C_6H_4F_2$
C
C_6F_6
B
Xe
D
C_6Br_6

Bibliography

[1] W. Ho, J. Chem. Phys. **117**, 11033 (2002).

[2] G. Binnig, H. Rohrer, C. Gerber, and E. Weibel, Appl. Phys. Lett. **40**, 178 (1982).

[3] G. Binnig, H. Rohrer, C. Gerber, and E. Weibel, Phys. Rev. Lett. **49**, 57 (1982).

[4] R. P. Feynman, Eng. Sci. **23**, 22 (1960).

[5] J. Repp, G. Meyer, S. M. Stojković, A. Gourdon, and C. Joachim, Phys. Rev. Lett. **94**, 26803 (2005).

[6] S. W. Wu, N. Ogawa, and W. Ho, Science **312**, 1362 (2006).

[7] P. Liljeroth, J. Repp, and G. Meyer, Science **317**, 1203 (2007).

[8] A. J. Heinrich, Science **298**, 1381 (2002).

[9] N. Nilius, T. M. Wallis, and W. Ho, Science **297**, 1853 (2002).

[10] G. V Nazin, X. H. Qiu, and W. Ho, Science **302**, 77 (2003).

[11] B. C. Stipe, M. A. Rezaei, and W. Ho, Science **280**, 1732 (1998).

[12] H. J. Lee and W. Ho, Science **286**, 1719 (1999).

[13] J. R. Hahn and W. Ho, Phys. Rev. Lett. **87**, 166102 (2001).

[14] Y. Jiang, Q. Huan, L. Fabris, G. C. Bazan, and W. Ho, Nat. Chem. **5**, 36 (2013).

[15] L. Lauhon and W. Ho, Phys. Rev. Lett. **84**, 1527 (2000).

[16] R. Wiesendanger, Rev. Mod. Phys. **81**, 1495 (2009).

[17] S. H. Pan, E. W. Hudson, and J. C. Davis, Appl. Phys. Lett. **73**, 2992 (1998).

[18] A. J. Heinrich, J. A. Gupta, C. P. Lutz, and D. M. Eigler, Science **306**, 466 (2004).

[19] X. H. Qiu, G. V Nazin, and W. Ho, Science **299**, 542 (2003).

[20] S. Loth, M. Etzkorn, C. P. Lutz, D. M. Eigler, and A. J. Heinrich, Science **329**, 1628 (2010).

[21] S. Baumann, W. Paul, T. Choi, C. P. Lutz, A. Ardavan, and A. J. Heinrich, Science **350**, 417 (2015).

[22] L. Gross, F. Mohn, N. Moll, P. Liljeroth, and G. Meyer, Science **325**, 1110 (2009).

[23] L. Gross, F. Mohn, N. Moll, B. Schuler, A. Criado, E. Guitián, D. Peña, A. Gourdon, and G. Meyer, Science **337**, 1326 (2012).

[24] J. Zhang, P. Chen, B. Yuan, W. Ji, Z. Cheng, and X. Qiu, Science **342**, 611 (2013).

[25] a M. Sweetman, S. P. Jarvis, H. Sang, I. Lekkas, P. Rahe, Y. Wang, J. Wang, N. R. Champness, L. Kantorovich, and P. Moriarty, Nat. Commun. **5**, 3931 (2014).

[26] D. G. de Oteyza, P. Gorman, Y.-C. Chen, S. Wickenburg, A. Riss, D. J. Mowbray, G. Etkin, Z. Pedramrazi, H.-Z. Tsai, A. Rubio, M. F. Crommie, and F. R. Fischer, Science **340**, 1434 (2013).

[27] A. Riss, A. P. Paz, S. Wickenburg, H.-Z. Tsai, D. G. De Oteyza, A. J. Bradley, M. M. Ugeda, P. Gorman, H. S. Jung, M. F. Crommie, A. Rubio, and F. R. Fischer, Nat. Chem. **8**, 678 (2016).

[28] J. I. Martínez, E. Abad, C. González, F. Flores, and J. Ortega, Phys. Rev. Lett. **108**, 246102 (2012).

[29] R. Temirov, S. Soubatch, O. Neucheva, A. C. Lassise, and F. S. Tautz, New J. Phys. **10**, 53012 (2008).

[30] C. Weiss, C. Wagner, C. Kleimann, M. Rohlfing, F. S. Tautz, and R. Temirov, Phys. Rev. Lett. **105**, 86103 (2010).

[31] C. Weiss, C. Wagner, R. Temirov, and F. S. Tautz, J. Am. Chem. Soc. **132**, 11864 (2010).

[32] C. Chiang, C. Xu, Z. Han, and W. Ho, Science **344**, 885 (2014).

[33] J. Bardeen, Phys. Rev. Lett. **6**, 57 (1961).

[34] J. Tersoff and D. R. Hamann, Phys. Rev. Lett. **50**, 1998 (1983).

[35] J. Tersoff and D. R. Hamann, Phys. Rev. B **31**, 805 (1985).

[36] J. Lambe and R. C. Jaklevic, Phys. Rev. **165**, 821 (1968).

[37] J. Klein, A. Léger, M. Belin, D. Défourneau, and M. J. L. Sangster, Phys. Rev. B **7**, 2336 (1973).

[38] C. Jiang, Vibrational Inelastic Electron Tunneling Spectroscopy of Surface Adsorbed Single Molecules at Sub-Kelvin Temperature, University of California, Irvine, 2015.

[39] L. Vitali, R. Ohmann, K. Kern, A. Garcia-Lekue, T. Frederiksen, D. Sanchez-Portal, and A. Arnau, Nano Lett. **10**, 657 (2010).

[40] F. J. Giessibl, Rev. Mod. Phys. **75**, 949 (2003).

[41] A. J. Weymouth, T. Hofmann, and F. J. Giessibl, Science **343**, 1120 (2014).

[42] N. Moll, L. Gross, F. Mohn, A. Curioni, and G. Meyer, New J. Phys. **12**, 125020 (2010).

[43] P. Hapala, G. Kichin, C. Wagner, F. S. Tautz, R. Temirov, and P. Jelínek, Phys. Rev. B **90**, 85421 (2014).

[44] P. Hapala, R. Temirov, F. S. Tautz, and P. Jelínek, Phys. Rev. Lett. **113**, 226101 (2014).

[45] W. L. Jorgensen, http://dasher.wustl.edu/ffe/distribution/params/oplsaa.prm (2008).

[46] R. F. Service, Science **309**, 95 (2005).

[47] D. Yuan, Z. Han, G. Czap, C.-L. Chiang, C. Xu, W. Ho, and R. Wu, J. Phys. Chem. Lett. **7**, 2228 (2016).

Chapter 2

Probing Intermolecular Coupled Vibrations by STM Inelastic Electron Tunneling Spectroscopy[*]

2.1 Abstract

Intermolecular interactions can induce energy shifts of molecular vibrations and can couple molecular motion. However, the detection of intermolecular coupled vibrations has not been reported thus far at the single molecule level. Here we show the detection of an intermolecular coupled vibration between an adsorbed CO molecule on a surface and CO-terminated tip with inelastic electron tunneling spectroscopy (IETS) in a sub-Kelvin scanning tunneling microscope. With density functional calculations, we identify this as the out-of-phase hindered translational mode of the CO dimer in the tunneling junction. We studied the evolution of the energy and IETS intensity of this coupled vibration as a function of tip-sample distance, which can be rationalized by the interplay between the tilting of the two CO molecules and their relative orbital alignment.

---

[*] This chapter by Z. Han, G. Czap, C. Xu, C. Chiang, D. Yuan, R. Wu and W. Ho is prepared for submission to *Physical Review Letters*.

2.2 Article

Historically, the carbon monoxide (CO) molecule has played a very important role in the development of modern surface science [1]. For the scanning probe microscopy community, it is also one of the most studied molecules. Recently, a number of scanning probe techniques have been developed which reveal organic molecular structures, such as scanning tunneling hydrogen microscopy (STHM) [2], non-contact atomic force microscopy (NC AFM) [3–5] and inelastic tunneling probe (itProbe) [6]. Functionalizing the scanning probe tip with a flexible atom or molecule is the key to obtaining the enhanced spatial resolution in these methods. In this regard, CO has become the preferred molecule. Furthermore, the adsorbed CO on surface has been studied as a model system for AFM to investigate intermolecular interactions with a CO-terminated tip using normal-force AFM [7,8] and lateral force microscopy (LFM) [9].

The vibrations of a molecule adsorbed on surface are fingerprints used to identify the nature of chemical bonding with its environment. These signatures can be characterized with STM at the single molecule level using inelastic electron tunneling spectroscopy (IETS) [10]. STM-IETS has been demonstrated to be a powerful tool for studying intermolecular interactions by measuring the energy shift of molecular vibrations [6,11,12]. However intermolecular coupled vibrations, to our knowledge, have not been reported. CO adsorbed on metal exhibits low energy hindered vibrations that are especially sensitive to interactions with its local environment. By monitoring the IETS intensity variations due to the energy shift of the CO-tip hindered translation, itProbe was devised to image the chemical structure of planar molecules on the surface [6]. In addition, CO has also served as the benchmark to study STM-IETS, such as IETS propensity rules [13,14], IETS line shape [15,16], and IETS with functionalized tip [14,17]. Therefore using a CO-tip to probe another CO on the surface creates an ideal system to study its vibrations with STM-IETS, not only for a better understanding of STM-IETS with a functionalized tip but also for new insight into intermolecular interaction between a flexible functional group and CO-tip, so as to pave the way to study non-planar molecules with laterally flexible functional groups by itProbe.

Here we demonstrate the first detection of an intermolecular coupled vibrational mode with STM-IETS. This coupled mode was induced by short range intermolecular repulsion between an adsorbed CO on the Ag(110) surface and a CO attached to the tip. Density functional calculations reveal that the novel vibrational mode is an out-of-phase hindered translation mode of the CO dimer in junction. We tuned the CO-CO intermolecular interaction by adjusting the tip-sample distance and found that the vibrational energy and IETS intensity of this coupled mode do not shift monotonically as the two CO molecules approach each other.

The experiment was performed in a home built sub-Kelvin STM at ultra-high vacuum with base pressure of 5×10^{-11} Torr. The microscope scanner was adapted from the design of a variable temperature STM [18]. Both the Ag(110) surface and the electrochemically etched silver tip were prepared by repeated Ne^+ sputtering and annealing. CO molecules were introduced to the surface at 25 K through a variable leak valve to obtain ~0.02 monolayer surface coverage. The sample was then cooled down to 600 mK for taking images and spectra.

CO molecules on Ag(110) surface were imaged as dark depressions with a metal tip as shown in Fig. 2.1(a). With a CO-terminated tip, another CO on surface was imaged as a protrusion at the center surrounded by dark lobes and a bright circular border as shown in Fig. 2.1(b). In another topography obtained at smaller tunneling gap displayed in Fig. 2.1(c), it appeared as four bright lobes at the center surrounded by a circular border. Additionally, individual surface silver atoms were resolved indicating a top-site adsorption for CO on Ag(110) surface.

The adsorption of the CO on surface or the tip apex can be verified by detecting its characteristic low energy vibrations with STM-IETS as shown in Fig. 2.1(d). The d^2I/dV^2 IETS taken with Ag tip over CO molecule and CO-tip over Ag(110) surface show three vibrational modes, besides the hindered translation (HT, ~2 meV) and hindered rotation (HR, ~20 meV) as reported before [6,17,19], another mode at 37.1 meV for the surface CO and 35.1 meV for the tip-CO was resolved. The energy is ~5 meV higher than the center of mass (CM) bouncing mode (Ag-CO stretch) compared to the reported results [20,21] and our own DFT calculation in Fig. 2.5. However, it is very close to the double of HR energy [22]. All the vibrational modes were red shifted for CO on the tip compared to CO on the substrate. The asymmetry in the IETS line shapes were consistent with a previous study of asymmetric tunneling junctions [15]. The IETS taken with the CO-tip over the center of the surface CO was shown as the bottom curve in Fig. 2.1(d). For this symmetric tunneling junction, the rising edge and falling tail of the HR mode in IETS shows symmetric line shape for opposite sample bias polarities. Intriguingly, in addition to the HT, HR and double HR modes for single CO, an extra vibrational mode at 7.6 meV emerges in the CO dimer tunneling junction.

To study the evolution of this extra vibrational mode as function different CO-CO interactions, we took a series of vibrational d^2I/dV^2 IETS in Fig. 2.2(a) by tuning the tip-sample distance. We plot the energies of the two vibrational modes below 10 meV in Fig. 2.2(c) to highlight their variation over different tip-sample separations. The lower energy mode υ_α around 1.5 meV is found to be almost independent of tip height, in contrast to the higher energy mode υ_β which shows non-monotonic variations. Mode υ_β blue shifts from 4.6 meV to 7.4 meV (ΔZ from -1.3 Å to 0.0 Å) and saturates from 0.0 Å to 0.8 Å for ΔZ. Interestingly, the energy red shifts when the tip-sample distance is further reduced.

To identify the vibrational modes (υ_α and υ_β) and clarify the evolution of their energies, we calculated the vibrational modes of the double CO tunneling junction using density functional theory with van der Waals correction. Twelve vibrational modes were calculated as listed in Fig. 2.7. Remarkably, both CO molecules tilted from vertical orientation in the same XZ plane, and all the hindered translation modes for the CO dimer are coupled (υ_9 to υ_{12}). The out-of-phase hindered translation in the CO tilting plane has the highest energy (8.1 meV) among these four vibrations. The three other modes have much lower energies (≤ 4.1 meV). Except for these four modes, all other vibrations have much higher energies (>10 meV). We therefore assign the υ_β to be the out-of-phase hindered translation in XZ plane and υ_α to be a mixture of the other three coupled hindered translations.

The calculated Z dependence of the υ_9 energy shown in Fig. 2.3(a) is in qualitative agreement with the experimental observations [Fig. 2.2(c)]. Evidently, the coupled vibrations originate from the short range intermolecular repulsion between the two CO molecules. Similar to LFM [9], the long range interaction between the macroscopic tip and surface does not contribute to the restoring force during the CO-CO lateral vibration. From Fig. 2.8 it can be found that the two CO oscillation vectors are parallel and the oscillation amplitudes of oxygen atoms ($\left|\overrightarrow{v_t^O}\right|$ and $\left|\overrightarrow{v_s^O}\right|$) are much bigger than carbons. Therefore the restoring force between two CO molecules, which is closely related to the coupled vibrational energy, is determined by the O-O distance $\left|\overrightarrow{O_tO_s}\right|$ and the relative motion of the two oxygen atoms ($\overrightarrow{v_t^O} - \overrightarrow{v_s^O}$) with respect to $\overrightarrow{O_tO_s}$. When the tip-CO is approaching the surface CO initially (Z ≥ 8.25 Å), $\left|\overrightarrow{O_tO_s}\right|$ is shortened. Simultaneously, strong intermolecular repulsion causes significant bending of the two CO molecules, and $\left|\overrightarrow{O_tO_s}\right|$ doesn't drop linearly with Z as shown in Fig. 2.3(c). The alignment between $\overrightarrow{O_tO_s}$ and $\overrightarrow{v_t^O} - \overrightarrow{v_s^O}$ is improved and the vibrational energy increases. When Z reaches 7.25 Å, the two oxygen oscillation vectors $\overrightarrow{v_t^O}$ and $\overrightarrow{v_s^O}$ obtain the best alignment with $\overrightarrow{O_tO_s}$ and the vibration energy is maximized. Furthermore, at closer tip-substrate distances (Z < 7.25 Å), the CO molecules tilt further apart causing $\left|\overrightarrow{O_tO_s}\right|$ to increase, while at the same time the alignment between $\overrightarrow{O_tO_s}$ and $\overrightarrow{v_t^O} - \overrightarrow{v_s^O}$ starts to deviate. As a consequence, the energy of the coupled vibration decreases.

In addition, the IETS intensity of υ_β also shows big variation for different tip-sample distances as displayed in Fig. 2.2(a). At some tip heights (ΔZ = 0.3, 0.5 and 0.8 Å) the IETS intensities of the υ_β mode are very weak. We plot the relative conductance change ($\Delta\sigma/\sigma$) due to the υ_β mode as a function of ΔZ in Fig. 2.4(a) to characterize inelastic electron tunneling cross-section. Based on the plot, we discern three regimes of intermolecular coupling. Regime i and iii are separated by regime ii where the IETS cross-section of υ_β is strongly suppressed.

The IETS cross-section of the double CO tunneling junction can be rationalized through IETS symmetry selection rules [23] or propensity rules [13,14]. The inelastic electron tunneling rate derives from the spatial overlap of the tip and sample states (ψ_t and ψ_s) with the deformation potential (δV_{vib}) caused by the vibration. Because the deformation potential δV_{vib} is spatially localized in the tunneling junction, thus only the local symmetries of the tip and sample states of the few most transmitting eigenchannels determine their contributions to the overall inelastic tunneling process [13,14]. The inelastic tunneling cross-section would be zero if $\psi_t\delta V_{vib}\psi_s$ is antisymmetric about any symmetry planes. Previous studies indicate the primary tunneling channels for CO-tip over surface CO have π character for both tip and sample states, however the CO tilting was not considered [14,24]. Nevertheless, the eigenchannel with p-wave tip states still dominates the conductance for a tilting tip-CO case [25]. Thus it is reasonable to assume both the tip and sample states have π character as shown in Fig. 2.4(b) for the dominant eigenchannel in the current double CO tunneling junction. The deformation potential of the υ_β is also sketched in Fig. 2.4(b) to reveal its symmetry and spatial distribution. As mentioned earlier, the oxygen atom has much larger oscillation amplitude than carbon, so the δV_{vib} is mostly localized on oxygen atoms.

With the reduction of tip-sample distance, the spatial overlap between tip and sample states is improved so that the IETS cross-section is enhanced initially in regime i. As Z is further reduced, the cross-section decreases and reaches its minimum in regime ii. This corresponds to the configuration that one lobe of the surface state is aligned with the nodal plane of the tip state as indicated by a blue dashed line in Fig. 2.4(b), so that the product of ψ_t, ψ_s, and δV_{vib} is antisymmetric about that plane, which in turn gives rise to the attenuated IETS intensity. When the tip enters regime iii, the CO tilting angle continues to increase, causing the orbital lobe of the surface CO and orbital nodal plane of the tip-CO to become misaligned, allowing the υ_β IETS feature to appear again in Fig. 2.2(a). However as the oxygen atoms are further separated in regime iii, the spatial overlap between tip and sample states where the deformation potential is the most significant is not as good as in regime i, so the IETS cross-section does not recover to the value observed in regime i.

In summary, we demonstrated the detection and identification of coupled intermolecular vibrations between a tip-CO and surface CO with STM-IETS and DFT calculations. We rationalized the evolution of the vibration energy and IETS cross-section as a function of tip-sample distance by considering the interplay between the CO bending and orbital alignment. This experimental evidence advances the understanding of the CO-tip vibration and its coupling to the local environment. It also provides deeper insights for IETS with functionalized tips. The current study suggests a promising local probe to identify non-planar chemical functional groups by detecting the coupled vibration between the CO-tip and its interacting partners, providing a useful complement to the existing high resolution scanning probe techniques that focus on planar molecules.

2.3 Supplementary Materials

DFT calculations were carried out using the plane-waved based Vienna ab initio simulation package (VASP) [26,27].The interaction between ion and core electron was treated by the projector augmented wave (PAW) method [28], and plane waves with an energy cutoff of 600 eV were used to expand the Kohn-Sham wave functions. For the vibration calculations, the adsorption geometries need to be optimized with extremely high converging thresholds, 0.003 eV/Å for force and 10^{-8} eV for total energy. The vibrational energies are determined by calculating the Hessian matrix using density functional perturbation theory (DFPT). In all calculations, we used 11×11×1 k-points mesh generated by the Monkhorst-Pack scheme [29].

We calculated the adsorption and vibration of CO on Ag(110) surface with vdW correction method (D3) [30,31]. The Ag(110) surface was modeled as a p(2×3) unit cell with a 5-layer Ag slab. The motion of the silver atom directly underneath the CO molecule was taken into account for the CO vibration calculation. The six calculated vibrational modes of CO on Ag(110) are listed in the Fig. 2.5.

To calculate the vibration of the CO-tip over CO on Ag(110) surface, the supercell is shown in Fig. 2.6. The Ag(110) substrate was modeled as a p(2×3) unit cell with a 6-layer Ag slab and the Ag tip was modeled as a silver adatom on the hollow site of Ag(110) surface. The three bottommost Ag layers of the supercell were frozen at their bulk position during geometric optimization. van der Waals functional with optB86b scheme [32] was employed for the description of intermolecular interaction between the two CO molecules in STM junction. Twelve vibrational modes were calculated for the

CO dimer in the tunneling junction. The eigenvectors and energies for these twelve modes at Z = 8.0 Å are displayed Fig. 2.7.

The calculated out-of-phase coupled hindered translational mode at different tip-sample distances are shown in Fig. 2.8 to compare with STM-IETS measurement.

Figure 2.1. STM topographies and vibrational IETS of CO on Ag(110). (a) STM constant current topography of CO molecules adsorbed on Ag(110) surface scanned with a bare Ag tip, tunneling set point is 0.1 nA and 10 mV, image size 45 Å × 45 Å. (b) and (c) Constant current topographies of the same area with a CO-terminated tip at 0.1 nA/10 mV and 0.5 nA/10 mV. The CO molecule transferred to the tip is indicated with the black arrow in (a). (d) d^2I/dV^2 STM-IETS for a bare Ag tip over Ag(110) as background (upper curves in black), Ag-tip over CO/Ag(110) (upper curves in red), CO-tip over Ag(110) (middle curves in blue) and CO-tip over CO/Ag(110) (bottom curves in green). The schematic diagrams of three corresponding tunneling junctions are displayed as insets. The spectra are magnified by 5 times to reveal the weak IETS feature near 35 meV. They are obtained with finer bias step size and more averaging passes. The sample bias is modulated by 2 mV_{RMS} at 311.11 Hz for all spectra. The tunneling gaps for the spectra are set with 0.17 nA/10 mV for Ag tip and 0.1 nA/10 mV for CO-tip.

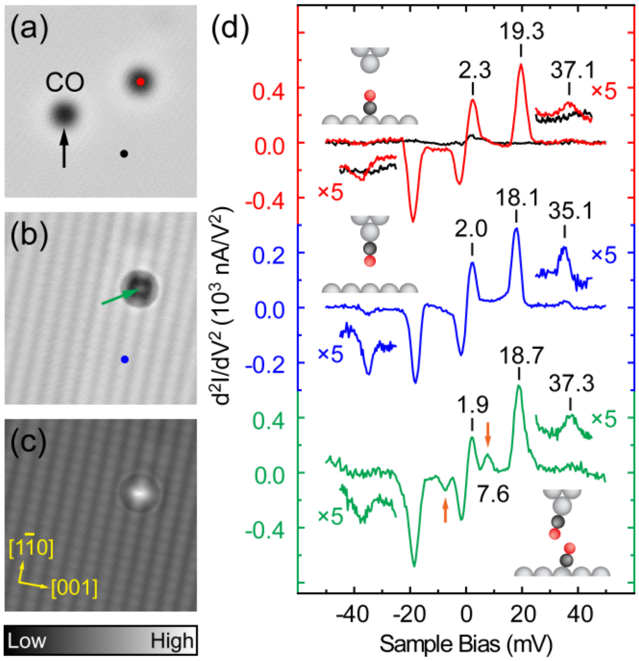
(a)
CO
(b)
(c)
[1$\bar{1}$0]
[001]
Low
High
(d)
19.3
2.3
37.1
×5
18.1
2.0
35.1
18.7
1.9
37.3
7.6
0.4
0.0
-0.4
0.2
-0.2
d^{2}I/dV^2 (10^3 nA/V^2)
-40
-20
0
20
40
Sample Bias (mV)

Figure 2.2. Z-dependent STM-IETS. (a) A series of STM-IETS taken with the CO-tip over the center of another adsorbed CO on Ag(110) at different tip-sample distances. The spectra are multiplied by different scale factors as indicated on the left side and offset vertically for better visualization. Sample bias modulation was 1.5 mV_{RMS} at 311.11 Hz. (b) Schematic diagram of CO-tip over CO on Ag(110). Z_0 is defined as the tunneling gap with I = 80 pA and V = 10 mV. For each spectrum, the tip feedback was turned off at Z_0, then the CO-tip was advanced by ΔZ to make the measurement. (c) The vibrational energies extracted from (a) versus ΔZ. The error bar of energy reflects the uncertainty from peak fitting and the error bar of ΔZ (about 0.03 Å) reflects the tip height drift during the measurement as well as the uncertainty of STM scanner ΔZ calibration. The higher energy mode υ_β is the out-of-phase coupled hindered translation as illustrated in the inset.

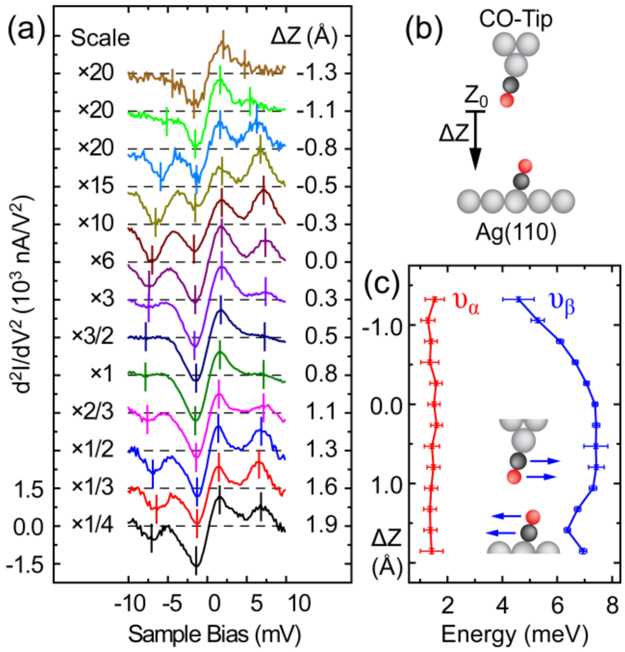
(a)
Scale
ΔZ (Å)
×20
×20
×20
×15
×10
×6
×3
×3/2
×1
×2/3
×1/2
×1/3
×1/4
-1.3
-1.1
-0.8
-0.5
-0.3
0.0
0.3
0.5
0.8
1.1
1.3
1.6
1.9
1.5
0.0
-1.5
d²I/dV² (10³ nA/V²)
-10
-5
0
5
10
Sample Bias (mV)
(b)
CO-Tip
Z₀
ΔZ
Ag(110)
(c)
υα
υβ
-1.0
0.0
1.0
ΔZ
(Å)
2
4
6
8
Energy (meV)

Figure 2.3. (a) The calculated energy of coupled vibrational mode (υ_9) versus tip-sample distance Z. The energy is maximized at Z = 7.25 Å as indicated by an arrow. (b) Schematic diagram of the coupled mode eigenvector at Z = 7.25 Å, Z is defined as the vertical distance from the bottom-most Ag atom on the tip and the top-most Ag atom on the surface. (c) Atom spacing variation of the double CO tunneling junction with Z.

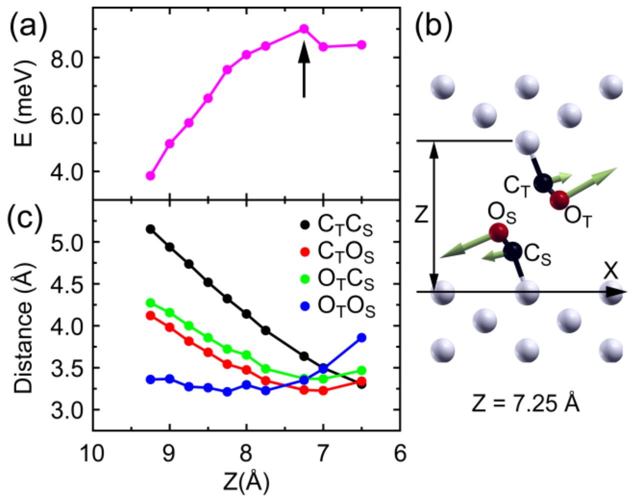
(a)
E (meV)
8.0
6.0
4.0
(b)
C_T
O_T
O_S
C_S
Z
X
Z = 7.25 Å
(c)
C_TC_S
C_TO_S
O_TC_S
O_TO_S
Distance (Å)
5.0
4.5
4.0
3.5
3.0
10
9
8
7
6
Z(Å)

Figure 2.4. (a) The relative conductance change due to mode υ_β as a function of ΔZ. The vibrational energies are also shown to reveal the correlation between energy and IETS intensity. Three coupling regimes specified by i, ii, and iii are defined based on the IETS intensity of υ_β mode. The regime ii corresponds to lowest IETS intensity. (b) Schematic diagrams to illustrate the interplay between the CO tilting angle and π orbital alignment of two CO's in the junction. The different phases of the CO orbitals are indicted by open and filled circles. The spatial distribution of the υ_β mode deformation potential δV_{vib} is depicted by color palette. Red and blue highlight the phase differences of δV_{vib}, which reflect the local symmetry of this out-of-phase coupled vibration.

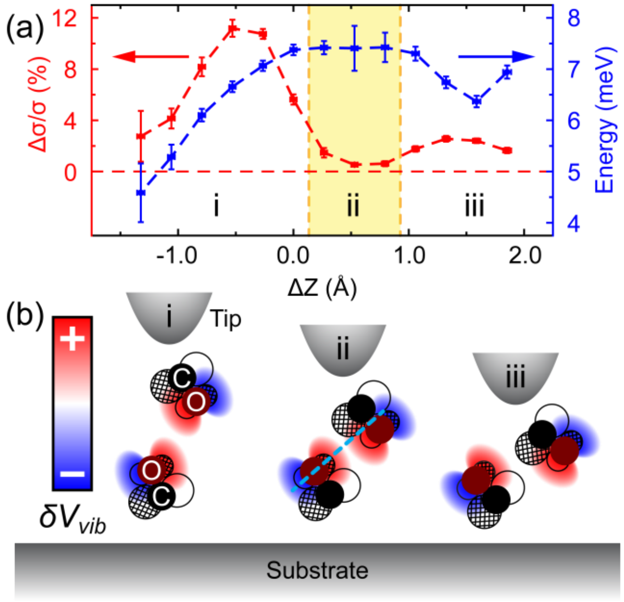
(a)
Δσ/σ (%)
12
8
4
0
Energy (meV)
8
7
6
5
4
i
ii
iii
-1.0
0.0
1.0
2.0
ΔZ (Å)
(b)
i
Tip
ii
iii
C
O
O
C
+
−
δV_vib
Substrate

Figure 2.5. The calculated vibrational modes of CO molecule on Ag(110). Six vibrational modes are identified, including one internal mode (C-O stretch) and five external modes (CM mode, two hindered rotations and two hindered translations). The vibrational energies are indicated for each mode in the unit of meV.

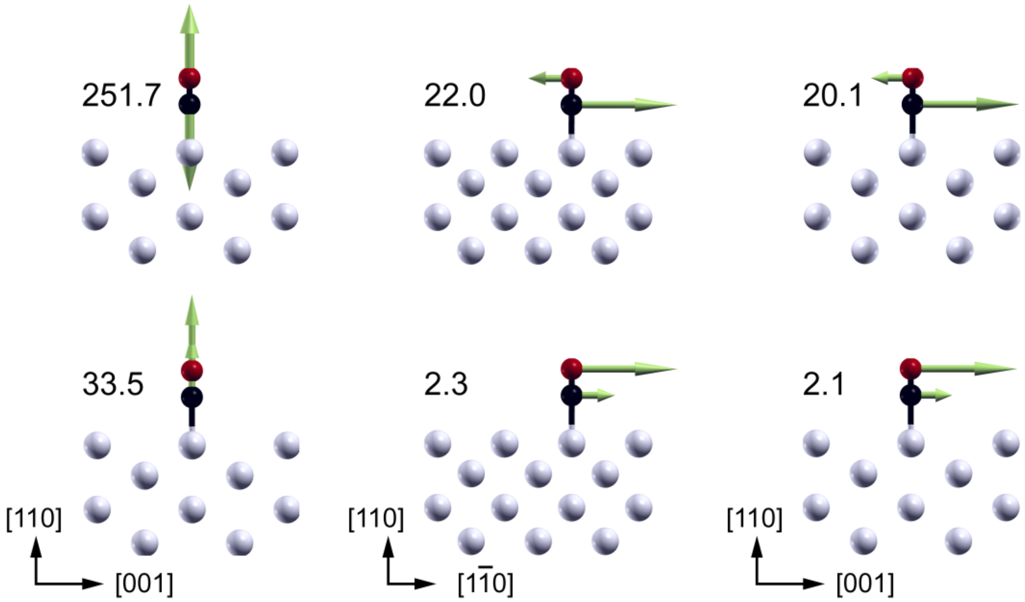
251.7
22.0
20.1
33.5
2.3
2.1
[110]
[001]
[110]
$[1\bar{1}0]$
[110]
[001]

Figure 2.6. Supercell of the CO-tip on CO/Ag(110) system used in the DFT calculation.

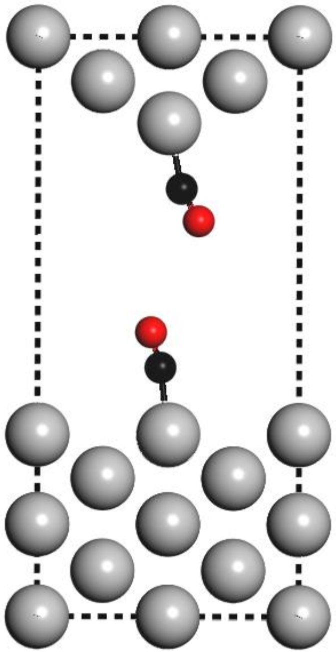

Figure 2.7. Calculated twelve normal modes of the double CO tunneling junction at a tip-sample distance Z = 8.0 Å. They are listed in the order of their vibrational energies. Two CO molecules in the tunneling junction prefer to tilt in the same XZ plane for optimized structure, X axis is along [001] direction and Z axis is along surface normal [110].

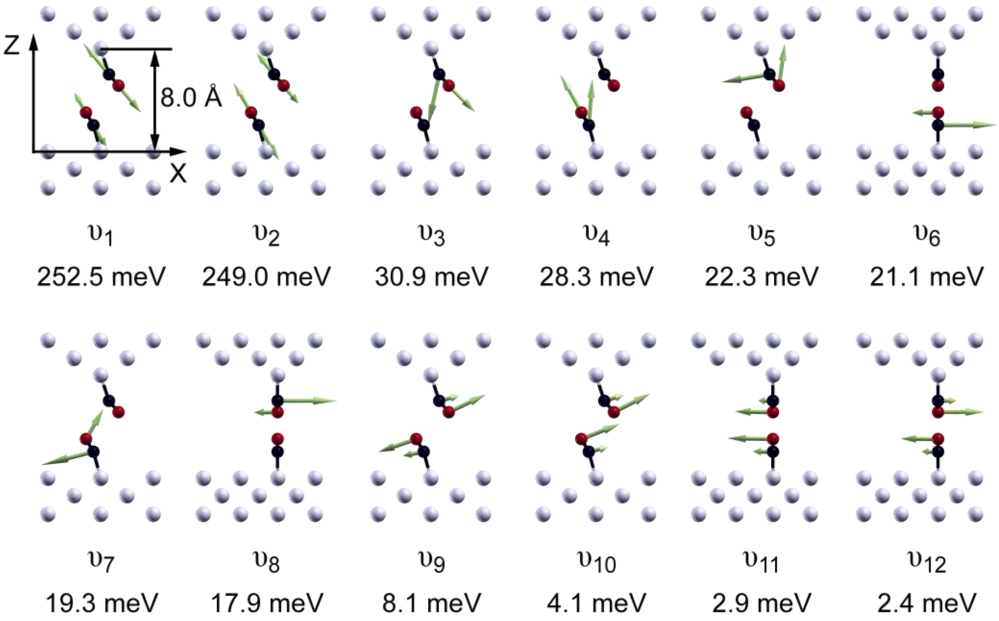
Z
X
8.0 Å
υ1
252.5 meV
υ2
249.0 meV
υ3
30.9 meV
υ4
28.3 meV
υ5
22.3 meV
υ6
21.1 meV
υ7
19.3 meV
υ8
17.9 meV
υ9
8.1 meV
υ10
4.1 meV
υ11
2.9 meV
υ12
2.4 meV

Figure 2.8. Schematic diagrams of the calculated eigenvectors for the out-of-phase coupled vibrational modes of the double CO tunneling junction at different tip-sample distances.

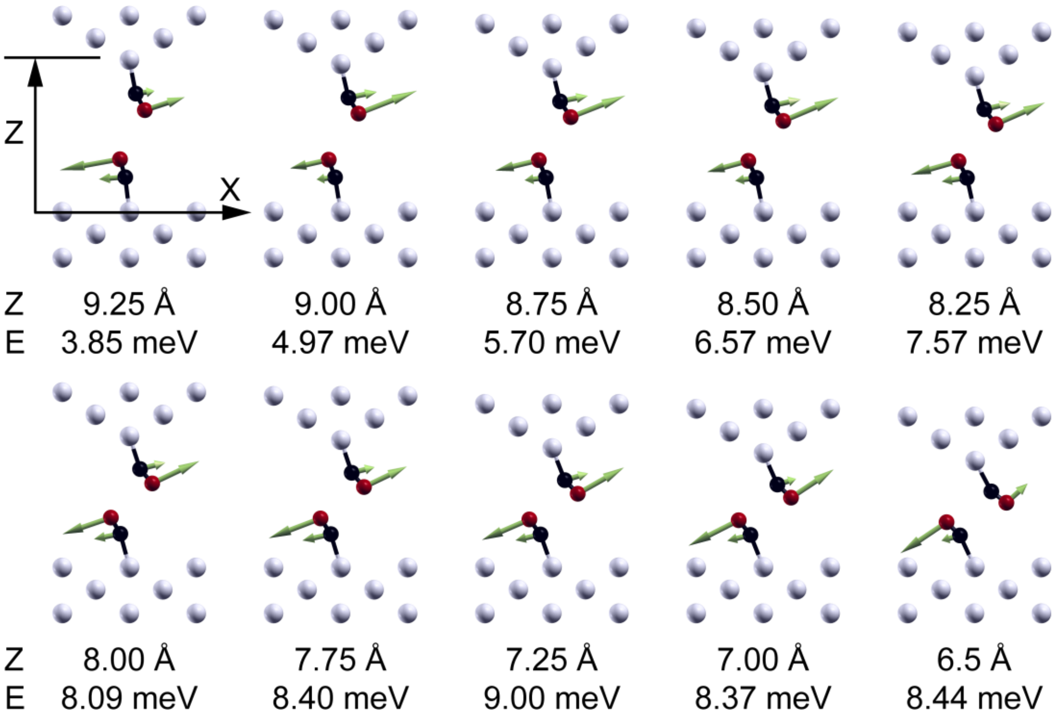
Z
X
Z 9.25 Å
E 3.85 meV
9.00 Å
4.97 meV
8.75 Å
5.70 meV
8.50 Å
6.57 meV
8.25 Å
7.57 meV
Z 8.00 Å
E 8.09 meV
7.75 Å
8.40 meV
7.25 Å
9.00 meV
7.00 Å
8.37 meV
6.5 Å
8.44 meV

Bibliography

[1] J. T. Yates, Surf. Sci. **299–300**, 731 (1994).

[2] G. Kichin, C. Weiss, C. Wagner, F. S. Tautz, and R. Temirov, J. Am. Chem. Soc. **133**, 16847 (2011).

[3] L. Gross, F. Mohn, N. Moll, P. Liljeroth, and G. Meyer, Science **325**, 1110 (2009).

[4] D. G. de Oteyza, P. Gorman, Y.-C. Chen, S. Wickenburg, A. Riss, D. J. Mowbray, G. Etkin, Z. Pedramrazi, H.-Z. Tsai, A. Rubio, M. F. Crommie, and F. R. Fischer, Science **340**, 1434 (2013).

[5] J. Zhang, P. Chen, B. Yuan, W. Ji, Z. Cheng, and X. Qiu, Science **342**, 611 (2013).

[6] C. Chiang, C. Xu, Z. Han, and W. Ho, Science **344**, 885 (2014).

[7] Z. Sun, M. P. Boneschanscher, I. Swart, D. Vanmaekelbergh, and P. Liljeroth, Phys. Rev. Lett. **106**, 46104 (2011).

[8] A. Schwarz, A. Köhler, J. Grenz, and R. Wiesendanger, Appl. Phys. Lett. **105**, 11606 (2014).

[9] A. J. Weymouth, T. Hofmann, and F. J. Giessibl, Science **343**, 1120 (2014).

[10] B. C. Stipe, M. A. Rezaei, and W. Ho, Science **280**, 1732 (1998).

[11] S. Li, D. Yuan, A. Yu, G. Czap, R. Wu, and W. Ho, Phys. Rev. Lett. **114**, 206101 (2015).

[12] J. Guo, J.-T. Lu, Y. Feng, J. Chen, J. Peng, Z. Lin, X. Meng, Z. Wang, X.-Z. Li, E.-G. Wang, and Y. Jiang, Science **352**, 321 (2016).

[13] M. Paulsson, T. Frederiksen, H. Ueba, N. Lorente, and M. Brandbyge, Phys. Rev. Lett. **100**, 226604 (2008).

[14] A. Garcia-Lekue, D. Sanchez-Portal, A. Arnau, and T. Frederiksen, Phys. Rev. B **83**, 155417 (2011).

[15] C. Xu, C. Chiang, Z. Han, and W. Ho, Phys. Rev. Lett. **116**, 166101 (2016).

[16] M. Persson, Philos. Trans. A. Math. Phys. Eng. Sci. **362**, 1173 (2004).

[17] J. R. Hahn and W. Ho, Phys. Rev. Lett. **87**, 196102 (2001).

[18] B. C. Stipe, M. A. Rezaei, and W. Ho, Rev. Sci. Instrum. **70**, 137 (1999).

[19] D. Yuan, Z. Han, G. Czap, C.-L. Chiang, C. Xu, W. Ho, and R. Wu, J. Phys. Chem. Lett. **7**, 2228 (2016).

[20] N. Lorente and H. Ueba, Eur. Phys. J. D **35**, 341 (2005).

[21] J. Oh, H. Lim, R. Arafune, J. Jung, M. Kawai, and Y. Kim, Phys. Rev. Lett. **116**, 56101 (2016).

[22] This mode has been identified to be the second harmonic of the CO HR mode in a recent high energy resolution STM-IETS meaurement. The results will be featured in a future publication.

[23] N. Lorente, M. Persson, L. J. Lauhon, and W. Ho, Phys. Rev. Lett. **86**, 2593 (2001).

[24] A. Gustafsson and M. Paulsson, Phys. Rev. B **93**, 115434 (2016).

[25] M. Corso, M. Ondráček, C. Lotze, P. Hapala, K. J. Franke, P. Jelínek, and J. I. Pascual, Phys. Rev. Lett. **115**, 136101 (2015).

[26] G. Kresse and J. Furthmüller, Phys. Rev. B **54**, 11169 (1996).

[27] G. Kresse and J. Furthmüller, Comput. Mater. Sci. **6**, 15 (1996).

[28] G. Kresse, Phys. Rev. B **59**, 1758 (1999).

[29] H. J. Monkhorst and J. D. Pack, Phys. Rev. B **13**, 5188 (1976).

[30] S. Grimme, J. Antony, S. Ehrlich, and H. Krieg, J. Chem. Phys. **132**, 154104 (2010).

[31] S. Grimme, S. Ehrlich, and L. Goerigk, J. Comput. Chem. **32**, 1456 (2011).

[32] J. Klimeš, D. R. Bowler, and A. Michaelides, J. Phys. Condens. Matter **22**, 22201 (2010).

Chapter 3

Imaging Halogen Bond: Self-assembly of Hexahalogenbenzene[*]

3.1 Abstract

The unique properties of halogens are responsible for the distinct structure and function of a broad range of molecular systems. Among the most electronegative elements, the additional variations in the size and polarizability of halogens require a different description of the intermolecular bonds they form. However, validation of various theories on the nature of halogen bonding has not been obtained. Here we use the inelastic tunneling probe to obtain real-space imaging of intermolecular bonding in the two-dimensional self-assembly of hexafluorobenzene (C_6F_6) and hexabromobenzene (C_6Br_6). Direct visualization is obtained for the surprising attraction and the pattern of bonding among the fully halogenated molecules and is contrasted with the lack of self-assembly in benzene (C_6H_6). Our results provide hitherto missing understanding of the intermolecular halogen bond.

---

[*] This chapter by Z. Han, G. Czap, C. Chiang, C. Xu, X. Wei, Y. Zhang, R. Wu, and W. Ho has been submitted to *Science*.

3.2 Article

The intermolecular halogen bond, hereafter the halogen bond, is an electrostatically driven, noncovalent interaction which has broad applications, including molecular self-assembly [1], supramolecular chemistry [2,3], crystal engineering [4,5], and drug design [6,7]. A halogen atom in a molecule is usually negatively charged. However, the anisotropic distribution of its electron density can lead to an equatorial belt of electron accumulation and an electron-depleted "σ-hole" at the pole [8,9]. The halogen bond is formed between the "σ-hole" and nucleophilic sites of adjacent molecules. However, the most electronegative and least polarizable fluorine is not expected to develop the "σ-hole" and participate in halogen bonding [8–10]. Results from non-contact atomic force microscopy suggest the C-F··· F mediated halogen bonding in a network of fully fluoro-substituted phenyleneethynylene molecules [11]. However, the rotational freedom of individual fluorinated rings is highly restricted due to the rigid chain structure in these molecules. In contrast, the hexafluorobenzene (C_6F_6) molecule has higher rotational freedom to accommodate a minimum energy configuration for the halogen bond.

The spontaneous formation of three-dimensional (3D) crystals at low temperatures suggests the likelihood of two-dimensional (2D), ordered self-assembly. However, similar molecules may display entirely different assembly behaviors on the surface. Benzene (C_6H_6) and C_6F_6 are model systems to study self-assembly of aromatic molecules. These two molecules share similar physical properties, such as polarizability, sublimation energy, quadrupole moments with similar magnitude but opposite sign, and edge-to-face structures in 3D crystals [10,12]. While C_6H_6 form a disordered 2D gas [13],

C_6F_6 self-assemble into ordered layer structures on different low-index surfaces of coinage metals [14,15]. A delocalized, nearly free electron band is formed in C_6F_6 island and has been identified as due to the hybridization of their lowest unoccupied molecular orbitals (LUMO) with superatom character [14,15]. To date, the nature of the intermolecular interactions leading to self-assembly of C_6F_6 into ordered 2D planar structures remains to be understood.

Here we carry out spectroscopic imaging of C_6H_6, C_6F_6, and hexabromobenzene (C_6Br_6) adsorbed on Ag(110) surface at 600 mK by the inelastic tunneling probe (itProbe) [16] based on the scanning tunneling microscope (STM). The contents of the images have been analyzed by DFT calculations. This series of molecules allows the investigation of the effects of bond length, atomic size and polarizability on the 2D self-assembly.

The C_6H_6 molecules adsorb randomly on the Ag(110) surface at 600 mK for coverages up to 0.35 monolayer (ML) [17], as seen in the constant current topographic images shown in Fig. 3.1A and 3.1B. Local order emerges at higher coverages (Fig. 3.1C), where molecular translation is sterically hindered. In contrast, at lower coverages, C_6F_6 form close-packed molecular islands (Fig. 3.1D) and C_6Br_6 aggregate into small clusters (Fig. 3.1E). Nevertheless, the atomic step edges of Ag(110) surface are favorable adsorption sites for all three molecules.

A CO molecule can be transferred to the tip by scanning with a small tunneling gap (e.g., 1 nA and 1 mV, corresponding to 1 MΩ gap resistance). The presence of CO on the tip is evidenced by the disappearance of this CO from the surface, a contrast change in the topography when the CO-tip is scanned over another CO molecule, an increase in the topographic image resolution, and the emergence of CO vibrations with the CO-tip positioned over the Ag surface. The ordered layer structure formed by the C_6F_6 molecules and imaged with the CO-tip is shown in Fig. 3.2A. The lattice of the first molecular layer is not fully commensurate with the rectangular symmetry of the underlying Ag(110), resulting in domain boundaries indicated with yellow dashed lines. The growth of the second molecular layer is found to initiate at these domain boundaries. A zoom in view of the boxed area in Fig. 3.2A is shown in Fig. 3.2B and overlaid with a lattice mesh of the underlying silver substrate. The atoms of the Ag(110) surface are imaged by scanning the CO-tip at a small tunneling gap (see Supplementary Fig. 3.5). Individual molecules are clearly resolved to form a nearly hexagonal close-packed lattice, with geometric deviations along the three closed-packed directions (see Table 3.2) that likely arise from interactions with the rectangular Ag(110) surface. However, the intermolecular orientations, in particular the rotational angles of the individual C_6F_6 with respect to one another, are still unresolved from the topographic images. As shown in Fig. 3.2B, the C_6F_6 molecules prefer to adsorb along the $[1\bar{1}0]$ direction but each with different local environment (see larger scan in Fig. 3.5).

In recent years, submolecular resolution of chemical structure has been achieved using a CO-tip in nc-AFM [18–20] and STM [16]. The origin of this enhanced contrast has attracted considerable experimental and theoretical treatment [21–23]. A semi-classical mechanical model has been developed which relates the contrast to the combination of short-range repulsive forces between CO and the adsorbed molecule and effects associated with CO relaxation [23]. The CO-tip in the nc-AFM probes the vertical (out of surface plane) gradient of the forces on the CO molecule, which become large and highly localized over the atoms and bonds due to short range repulsive forces. In the extension of the mechanical model to the itProbe, the lateral vibrations of the CO molecule on the tip serve as a probe of the gradient of lateral forces on the CO molecule, yielding similar contrast at small tip-sample gap [24].

The CO-tip in the itProbe is crucial for obtaining atomic resolution of the metal substrate in order to determine the adsorption site of the molecule as well as for imaging the molecular structure [16]. The hindered translational vibration of the tip-CO is sensitive to its local environment. STM inelastic electron tunneling spectroscopy (IETS) [25] of the CO-tip over selected points of the molecular layer is shown in Fig. 3.2C. The vibrational energy varies by more than 2 meV when the CO-tip is positioned over different locations of the adsorbed molecules. For example, the vibrational energy shifts from 3.4 meV in the center of the carbon ring to 1.2 meV near the edge of the ring. The short-range repulsive forces between the CO and the underlying molecule, which tend to be localized at atoms and bonds, red-shift the CO hindered translational vibration [16,24]. By monitoring the d^2I/dV^2 intensity at a chosen bias of 1.2 mV, the locations of the red-shifted CO hindered translation are imaged by the itProbe as shown in Fig. 3.2D, with the corresponding schematic diagram in Fig. 3.2E. The intermolecular features are highlighted by the red dashed lines.

The itProbe image reveals a rich network of intermolecular interactions within the C_6F_6 island. Three nearest molecules self-organize to form a triangular windmill structure similar to halogen-3 synthon in halogen bond [10,26]. Each fluorine atom in a molecule is interacting cyclically with another fluorine atom of an adjacent molecule. Each molecule rotates about 20 ° from the fluorine head-to-head configuration. Within each F-3 synthon shown in Fig. 3.2E, the fluorine atom in one molecule is not aligned with the C-F bond axis of the adjacent molecule; the C-F···F angle is not 180 °. This can be understood by considering the interaction between molecule and substrate. Calculations by DFT (Table 3.1) indicate that C_6F_6 favors the short bridge SB2 adsorption site on Ag(110) surface (Fig. 3.6), in which two C-F bonds are aligned along the $[1\bar{1}0]$ direction. The orientation of each molecule in the self-assembled island in Fig. 3.2E is almost the same as the isolated monomer, and is only rotated about 4 ° clock-wise from the SB2 configuration due to intermolecular interactions.

Comparison of the measured results with DFT calculations reveals the origin of the contrast in the itProbe image. The presence of a molecule in space is evidenced by the potential it creates from its charge density distribution. The interaction of the CO-tip with this potential yields the potential energy surface (PES) that directly relates to the shift in the CO vibrational energy. Intermolecular interactions within the island lead to additional features in the PES (Fig. 3.3A) that are absent for isolated molecules due to redistribution of the electron density. The spatial variations of the PES (Fig. 3.3A) are sensed by the CO molecule and modify the energy of the CO vibrations. Specifically, the CO hindered translational vibration can be approximated as a lateral harmonic oscillator with the vibrational energy governed by the interaction of the CO with the tip and the C_6F_6, as shown in Fig. 3.3B. The ridges and apexes in the PES are associated with regions of negative curvature that reduces the overall curvature of the CO vibrational potential well and leads to a measureable red-shift of the vibrational energy. The 2D imaging of the vibrational intensity at a reduced energy (such as 1.2 meV compared to 2.5 meV over the Ag background [16]) reveals a real-space view of the skeletal structure and intermolecular interactions. Indeed, the apexes and ridges are highlighted in the smaller principal surface curvature plot of the calculated PES in Fig. 3.7A, that shows good agreement with the itProbe image in Fig. 3.2D.

The Br···Br halogen bonds facilitate the self-assembly of bromine terminated aromatic molecules on inert surfaces [27–33], ascribed to the large polarizability of bromine. The positively polarized "σ-hole" at the pole of a bromine atom is attracted by the negatively polarized equator of a neighboring Br in a cyclic fashion, leading to the Br-3 synthon [30–32]. The adsorption of C_6Br_6 molecule on Ag(110) serves as a standard model of halogen bonding to compare with the intermolecular bonding structure of C_6F_6 islands. The C_6Br_6 molecules form small clusters on the surface, in contrast to the formation of large aggregates of C_6F_6 while isolated C_6F_6 monomers are not observed on the surface, as shown in Fig. 3.1.

The C_6Br_6 molecules are adsorbed as monomers, dimers, and triangular trimers in the topographic images of Fig. 3.4A scanned with a CO-tip. The orientation of the C_6Br_6 molecules and their intermolecular interactions within a cluster are imaged by constant height itProbe in Fig. 3.4B-D. The corresponding schematic diagrams of the molecules with the underlying Ag(110) lattice are shown in Fig 4A inset, Fig 4E and Fig 4F. Strikingly, the C_6Br_6 monomer is surrounded with a bright circular border in the itProbe image of Fig. 3.4D, which arises from the potential energy surface profile created by the large van der Waals radius of the six bromine atoms. In the itProbe images of the dimer and trimer, the circular borders are flattened toward the intermolecular region due to modification of the PES associated with the intermolecular interactions between adjacent C_6Br_6 molecules. The molecular adsorption geometry is determined from the superposition of atomically resolved substrate scan and the itProbe images over the same area (Fig. 3.5B-C). All C_6Br_6 monomers are in registry with the substrate in the SB2 adsorption site, as shown in the inset of Fig. 3.4A and from the DFT calculation.

Single C_6Br_6 molecules can be pulled away one by one from a molecular cluster by tip manipulation. The isolated molecule can be found to adsorb occasionally in another configuration with 90° rotation (LB1), as shown in Fig. 3.8. However, the molecule is less stable in the LB1 configuration. It can be disturbed during scanning and convert to and remain in the stable SB2 configuration. In the C_6Br_6 dimer, both molecules maintain nearly the SB2 adsorption configuration, except for a slight rotation and displacement toward each other, as shown in Fig. 3.4E. Surprisingly, the molecules rotate 90° in the trimer and relocate from SB2 to the LB1 adsorption configuration. The Br atoms interact cyclically to form the close-packed Br-3 synthon. Contrary to C_6F_6, the C-Br bond axis is almost perfectly aligned with the tip of the neighboring Br atom due to the relatively stronger intermolecular interaction over the interfacial interaction.

DFT calculations incorporating van der Waals correction have been employed to clarify the nature of the intermolecular interaction among halogenated benzenes in the self-assembly, as well as an ordered C_6H_6 lattice constructed artificially by tip manipulation. In our DFT calculations, we only consider the hexagonal lattice of molecules without the silver substrate. The molecules are allowed to rotate in the relaxation process. The binding energy of the C_6F_6 lattice and rotation angle θ of the optimized structures are plotted as a function of lattice constant d in Fig. 3.3D. Similar plots for lattices of C_6H_6 and C_6Br_6 are presented in Fig. 3.9. The calculated results are summarized in Table 3.2 for comparison with experiment. Evidently, the binding energy of the C_6F_6 lattice without van der Waals correction is 12 meV, which is less than 10% of the binding energy when the van der Waals correction is included (128 meV). The driving force for self-assembly of C_6F_6 molecules originates from van der Waals interactions. In addition, the optimized rotation angle (20.3°) at the most stable lattice constant matches well with the experimental value (21.2 ± 1.3°). Remarkably, the rotation angle of the molecule is nearly independent of the van der Waals correction. This independence suggests that the relative orientation of the molecules is not driven by van der Waals interaction, despite its dominant contribution to the binding energy. Instead, the neighboring C_6F_6 molecules self-arrange into a windmill fashion in order to minimize the coulomb repulsion between the fluorine groups [11]. Similarly, for the C_6H_6 and C_6Br_6 lattices, the bonding energies are also much larger with the inclusion of the van der Waals correction but the molecular orientation is similarly independent of the correction (Fig. 3.9 and Table 3.2).

It should be noted that the windmill F-3 synthon in the C_6F_6 self-assembly indicates very similar directionality of C-F···F contacts to previous studies of BPEPE-F18 [11] and C_6Br_6 trimer in this study. Traditionally, the C-F···F contacts are not classified as halogen bonds. The small polarizability of F atoms prevents the development of a "σ-hole" at the pole of the C-F bond [8–10]. However, the universal pattern of halogen-3 synthon observed in the self-assembly of hexahalogenbenzene suggests a common bonding mechanism. The halogen-3 synthon in the molecular assemblies arises from the sum of the van der Waals attraction and the electrostatic interaction between terminating halogen atoms. Molecules rotate to optimize the electrostatic interaction; it minimizes the electrostatic repulsion for the F-3 synthon and maximizes the electrostatic attraction for the Br-3 case.

Molecular self-assembly on a surface is a fine balance between the intermolecular interactions, molecule-substrate interactions, and thermal excitations. The intermolecular interactions should be sufficiently strong to compete against molecule-substrate interactions and thermal perturbations in order to form a stable assembly. On the other hand, the thermal energy also enables the molecule to overcome the local diffusion barrier on the surface and interact with each other in close proximity. The strong halogen bond in C_6Br_6 moves the molecules from the SB2 adsorption site favored by isolated molecules to the LB1 site in order to maximize the intermolecular interactions. Furthermore, once a small cluster is formed, its size is self-limited by surface diffusion and the strong intermolecular bonding prevents the cluster to dissociate for a molecule to migrate and merge into other clusters.

The binding energies are similar for C_6F_6 and C_6H_6 in their optimized lattice structures (153 meV vs 128 meV in Table 3.2), despite the difference in their optimized lattice constants of 7.7 Å for C_6F_6 and 6.8 Å for C_6H_6. This difference arises from the shorter C-H bond (1.092 Å) compared to the C-F bond (1.345 Å) and the difference in the van der Waals radius of 1.20 Å for hydrogen compared to 1.46 Å for fluorine [34]. When molecules land on the surface, they first diffuse from one site to an adjacent site. In Fig. 3.10C, the two C_6F_6 molecules are positioned at next-nearest short bridge sites along the $[1\bar{1}0]$ direction, separated by two Ag lattice constants (2a = 8.1 Å). Their binding energy is about 40 meV, estimated to be 1/3 of the binding energy of the C_6F_6 lattice with 8.1 Å lattice constant in Fig. 3.3D. In contrast, when two C_6H_6 molecules are positioned at the same lattice sites as indicated in Fig. 3.10D, the binding energy is only about 15 meV (Fig. 3.9B). Thus the C_6F_6 dimer grows into a stable self-assembled structure due to a smaller lattice mismatch with the Ag(110) surface along the $[1\bar{1}0]$ direction and higher binding energy at 8.1 Å separation compared to C_6H_6. The close-packed C_6F_6 lattice contains periodic domain boundaries, occurring at approximately every four rows of molecules, to accommodate the lattice mismatch. Close-packed islands with local order can be realized at high surface coverages or by manipulating C_6H_6 molecules one by one for form islands, as shown in Fig. 3.10A. However, these structures are not stable against small perturbation at low coverages and C_6H_6 form disordered, non-aggregated structures on the Ag(110) surface.

In conclusion, we reveal the competition of intermolecular interactions and interfacial interactions that are responsible for the different adsorption behaviors for benzene, hexafluorobenzene, and hexabromobenzene on Ag(110). We demonstrate the possibility to tune 2D self-assembly of aromatic molecules by substituting the terminal functional groups of benzene. These results provide insights for designing supramolecular architectures involving hydrogenated and halogenated aromatic molecules. Intramolecular skeletal structure and intermolecular interactions for adsorbed molecules are imaged by the itProbe. These experiments demonstrate the capability to probe the nature of chemical bonds, revealing the nuanced interplay of weak interactions such as the van der Waals forces, electrostatic repulsions, and halogen bonds between molecules.

3.3 Supplementary Materials

The experiments were conducted under ultra-high vacuum (UHV) with base pressure at 5×10^{-11} Torr, and measurements were taken with a home-built 600 mK scanning tunneling microscope cooled by a single shot He-3 cryostat. The microscope scanner design was adapted from a UHV variable temperature STM [35]. The Ag(110) sample and electrochemically etched silver tip were prepared *in situ* by Ne^+ sputtering and annealing. Benzene (C_6H_6 from Sigma-Aldrich Co.) and hexafluorobenzene molecules (C_6F_6 from Sigma-Aldrich Co.) were purified with repeated freeze-pump-thaw cycles. Carbon monoxide (CO) and one of the aromatic molecules (C_6H_6, C_6F_6, or C_6Br_6) were sequentially dosed onto the Ag(110) surface at 25 K. Separate experiments were carried out for the other two aromatic molecules. The room temperature vapor from C_6H_6 or C_6F_6 was dosed through a variable leak valve, while C_6Br_6 was deposited on the surface from a Knudsen cell thermal evaporator. Following molecular dosings, the sample with adsorbed molecules and the scanner were cooled down to 600 mK for imaging and spectroscopic measurements.

We record itProbe images in this study with different operational modes: constant current mode and constant height mode. In constant current mode, the tip height is adjusted at each pixel to maintain constant tunneling current. In constant height mode, the tip height is held constant while the current varies at each pixel. The tip can advance towards the surface by 1 to 2 Å prior to recording data at each pixel and retract by the same amount during tip movement from one pixel to the next one. This retraction reduces perturbation of the adsorbed molecule. However, if the adsorbed molecule, such as C_6Br_6

is bonded sufficiently strong to the surface, the tip height does not need to be adjusted during the entire imaging process, given that the gap does not significantly drift with the feedback off.

1. In constant current mode, the tunneling feedback is turned off at each pixel and the sample bias is ramped to the desired value for d^2I/dV^2 imaging. In Fig. 3.2D, feedback is turned off at 0.12 nA and 10 mV and the bias is set to 1.2 mV for imaging. After the data is taken at a given pixel, the bias is ramped back to 10 mV and feedback is activated again before moving to the next pixel.

2. In constant height mode, tunneling feedback is turned off at a chosen location, and the sample bias is ramped to the imaging value. Tip can be advanced towards the surface by a pre-chosen offset distance, and kept at the same height throughout the imaging. At the end of imaging, tip is retracted by the same offset distance, then the sample bias is set to the initial set point and tunneling feedback is reactivated. For example, Fig. 3.4B-D, Fig. 3.8C and Fig. 3.8F are imaged in constant height mode at 1.5 mV and feedback is turned off at the tunneling set point I = 0.1 nA and sample bias = 0.1 V at different locations. Here we list the locations where the feedback is deactivated and the tip offset distances for these five images.

Fig. 3.4B: feedback is turned off at the center of lower right molecule, tip advanced by 1.59 Å.

Fig. 3.4C: feedback is turned off at the center of upper right molecule, tip advanced by 1.46 Å.

Fig. 3.4D: feedback is turned off at the center of the molecule, tip advanced by 1.46 Å.

Fig. 3.8C: feedback is turned off at the center of the molecule, tip advanced by 1.46 Å.

Fig. 3.8F: feedback is turned off at the center of the molecule, tip advanced by 1.32 Å.

The atomic lattice of metal surfaces can be resolved in constant current topographic images with a CO-terminated tip. The tunneling set point is usually 0.5 nA (or bigger) for the tunneling current and 10 mV for the sample bias. During such small-gap scanning condition, the images for the molecules are distorted. Nevertheless, we can scan over the same area again with a larger tunneling gap, such as 0.12 nA and 60 mV, and superimpose these two images to identify the center of the molecule and obtain its adsorption site. This procedure was performed to obtain the adsorption site for molecules in C_6F_6 islands and C_6Br_6 clusters, as shown in Fig. 3.5.

Furthermore, we can zoom in on the molecule and perform itProbe measurements to reveal its orientation. By combining the itProbe image with the atomically resolved lattice scan over the same area, we can precisely determine the molecular adsorption configuration.

The experimentally determined lattice constants and molecular orientations are listed in Table 3.2 for the three benzene systems and comparisons are made to DFT calculations. As mentioned in the main text, C_6H_6 do not form close-packed lattice structure at low coverage. Even at high coverage, only close-packed molecular rows along $[2\bar{2}\bar{1}]$ and $[2\bar{2}1]$ are formed. However, we can use STM tip to manipulate the C_6H_6 molecules and assemble them into a metastable island for the determination of the molecular separation in three directions as shown in Fig. 3.10A. The manipulation of

C_6H_6 is both bias and tunneling gap dependent. Here we use 1 nA and 100 mV with bare Ag tip to assemble this island. Each benzene molecule takes the short bridge site, and CO molecule is adsorbed on the top site of Ag(110). Similar to C_6F_6 lattice, C_6H_6 also form rhombic lattice on Ag(110). The lattice constant is 8.08±0.07 Å along the [001] direction, which matches well with twice the Ag lattice constant. The lattice spacing is 6.86±0.09 Å along $[2\bar{2}\bar{1}]$ or $[2\bar{2}1]$ direction.

For C_6F_6 lattice on Ag(110), the rhombic lattice is closer to a hexagonal lattice compared to the C_6H_6 lattice, indicating a stronger intermolecular interaction than C_6H_6. Along [001] direction, the lattice spacing is 7.85±0.05 Å and changes to 6.86±0.09 Å along the other two close-packed directions. The overall intermolecular spacing is 7.62±0.18 Å, as shown in Fig. 3.3D and compared with hexagonal lattice constant in DFT calculation.

For C_6Br_6, the experimental lattice constant is measured from different intermolecular spacing of a sample of molecular clusters on the surface. The intermolecular separation in C_6Br_6 does not show directional dependence, thus only one value is shown for the experimental measurement.

The first-principles DFT calculations were carried out by using the Vienna *ab initio* simulation package (VASP) [36]. The exchange-correlation interaction among electrons was described at the level of the generalized gradient approximation (GGA) with the Perdew, Burke, and Ernzerhof functional [37]. The optimized van der Waals correction term (optB86b-vdW) [38] was invoked in the calculations of adsorption energy for isolated C_6H_6, C_6F_6, and C_6Br_6 on Ag(110) and intermolecular interactions within the molecular lattices.

To calculate the intermolecular interactions within the molecular lattices for the three benzene systems, the kinetic cutoff energy for the plane wave expansion was 700 eV, $4\times4\times2$ k-mesh grid was chosen for sampling the first Brillouin zone. The hexagonal molecular lattice was fully relaxed until the forces on all atoms were less than 0.01 eV/Å. For electronic structural optimization, the energy convergence criterion was 10^{-7} eV.

For the potential energy surface (PES) calculation of the C_6F_6 lattice, the Ag tip was modeled as a tetrahedron cluster of four Ag atoms, and a CO molecule was attached to the bottom Ag atom. Only CO molecule was allowed to fully relax, while C_6F_6 lattice and Ag tip were fixed at each tip position. The initial height of the O atom to the plane of the C_6F_6 molecule was set at 3.0 Å. The lattice constant of C_6F_6 unit cell was 7.9 Å. The vacuum layer was 20 Å. The C_6F_6 lattice unit cell was divided to 10×10 mesh, then the potential energy of the C_6F_6 lattice with the Ag-CO tip was calculated at each mesh point. Two principal curvatures could be derived at every point on a 2D surface [39]. We calculated the principal curvatures of the PES and plotted the smaller one to highlight the apexes and ridges of PES in Fig. 3.7.

To calculate the adsorption energy for isolated molecules on Ag(110) surface, the Ag(110) surface was modeled with a p(4×4) unit cell with a 4-layer Ag slab and an 18 Å thick vacuum for C_6H_6 and C_6F_6. While for C_6Br_6 adsorption, we modeled Ag(110) surface using a p(4×6) unit cell with a 3-layer Ag slab and an 18 Å thick vacuum. The two bottommost Ag layers were frozen at their bulk positions during geometric optimization. The adsorption geometries were optimized with extremely precise convergence thresholds: 0.002 eV/Å for forces and 10^{-8} eV for the total energy, and large energy cutoff of plane wave expansion (700 eV). In all calculations, we used a $2\times3\times1$

k-points mesh for C_6H_6 and C_6F_6 molecules and a 3×3×3 k-points mesh for C_6Br_6 generated by the Monkhorst-Pack scheme. The adsorption energy is defined as $E_{ads} = -(E_{mol+Ag(110)} - E_{Ag(110)} - E_{mol})$, where E_{mol} is energy of isolated single molecule of C_6H_6, C_6F_6, C_6Br_6, $E_{Ag(110)}$ is the energy of bare Ag slab, $E_{mol+Ag(110)}$ is the total energy of the single molecule adsorbed on the Ag slab. The calculated adsorption energies for these three systems are listed in Table 3.1.

For C_6H_6, the calculations show SB1 to be the strongest binding configuration, in agreement with experimental observations [17], while for C_6F_6, SB2 is the most stable configuration. Although isolated C_6F_6 monomer was not found on the surface in our experiment, the orientation of SB2 on the Ag(110) lattice matches the that for C_6F_6 in the self-assembled island. In addition, domain boundaries are developed in C_6F_6 islands to avoid hollow site adoption, which is the most unfavorable site indicated by the calculations. For C_6Br_6, the calculations show LB1 as the optimal adsorption configuration, in contrast with the SB2 configuration revealed by STM measurement. However, the energy difference between LB1 and SB2 is less than 10 meV, within the accuracy of our current calculations.

This work was supported by the Chemical Science, Geo- and Bioscience Division, Office of Science, U.S. Department of Energy, under Grant No. DE-FG02-04ER15595 (ZH) and DE-FG02-06ER15826 (CX), the Condensed Matter Physics Program, Division of Materials Research, National Science Foundation, under Grant No. DMR-1411338 (GC, CJ, XW), and the National Science Foundation Center for Chemical Innovation on Chemistry at the Space-Time Limit (CaSTL) under Grant No. CHE-1414466 (YZ). Additionally, XW received support from the China Scholarship Council and the National

Natural Science Foundation of China (Grant No. 61171011). Experiments were carried out by ZH, GC, CJ, CX, and XW, YZ performed the calculations.

Figure 3.1. Constant current STM topography of C_6H_6, C_6F_6 and C_6Br_6 molecules on the Ag(110) surface at 600 mK. (A), (B) and (C) are C_6H_6 with 0.10, 0.35 and 0.60 monolayer (ML) coverages (240 Å × 240 Å, tunneling set point: 0.1 nA, 20 mV). (D) C_6F_6 with 0.20 ML coverage (640 Å × 640 Å, tunneling set point: 0.1 nA, 0.5 V). (E) C_6Br_6 with 0.15 ML coverage (640 Å × 640 Å, tunneling set point: 0.1 nA, 0.1 V).

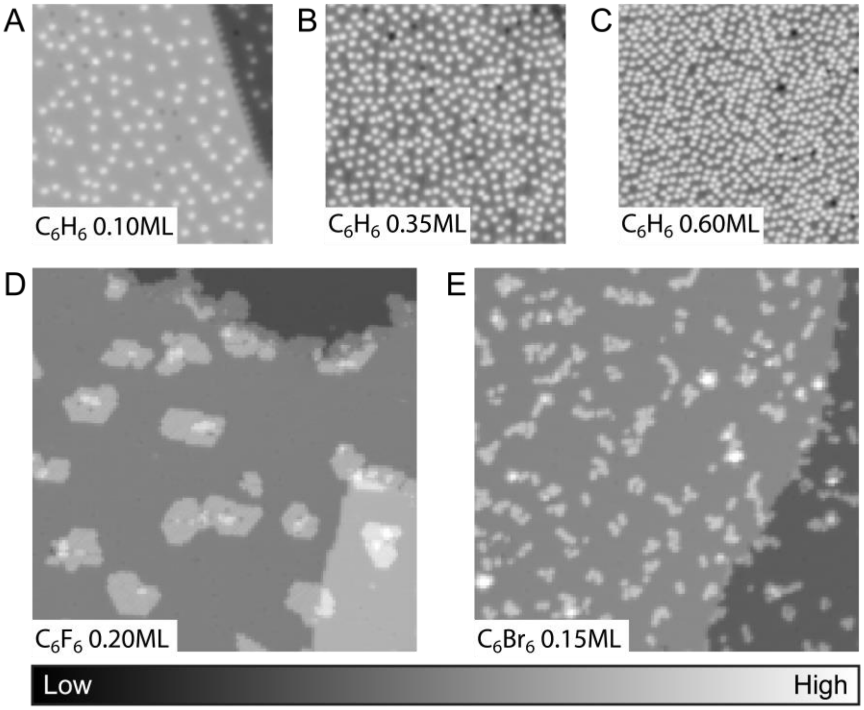
A
B
C
C_6H_6 0.10ML
C_6H_6 0.35ML
C_6H_6 0.60ML
D
E
C_6F_6 0.20ML
C_6Br_6 0.15ML
Low
High

Figure 3.2. Self-assembled C_6F_6 island on the Ag(110) surface. (A) Constant current topography of C_6F_6 island and co-adsorbed CO molecule on Ag(110) with CO-terminated tip (120 Å × 120 Å, set point: 0.1 nA, 0.1 V). Domain boundaries are indicated by yellow dashed lines. (B) Constant current topography over the blue box region in (A), the gray rectangular grid represents the underlying Ag(110) lattice with surface atoms at the line intersections (15 Å × 15 Å, set point: 0.12 nA, 60 mV). (C) Vibrational STM-IETS d^2I/dV^2 spectra of the CO-tip taken over different locations of C_6F_6 island, specified in the constant current topography shown above (15 Å × 15 Å, set point: 0.08 nA, 10 mV). For clarity, all the spectra are offset vertically by 400 nA/V^2. The peak position is shown for each spectrum. The intercept of each spectrum with the orange dashed line at 1.2 mV characterizes the intensity variation due to the shift of CO hindered translational energy. Bias voltage modulation: 1 mV_{RMS} at 311.11 Hz. Set point: 0.09 nA, 10 mV. (D) Constant current itProbe imaging at 1.2 mV over the same area as (B) (160 × 160 pixels, 15 Å × 15 Å, set point: 0.12 nA, 10 mV). (E) Schematic diagram of the skeletal structure of C_6F_6 self-assembly shown in (D) and the intermolecular bonding network highlighted with red dashed lines.

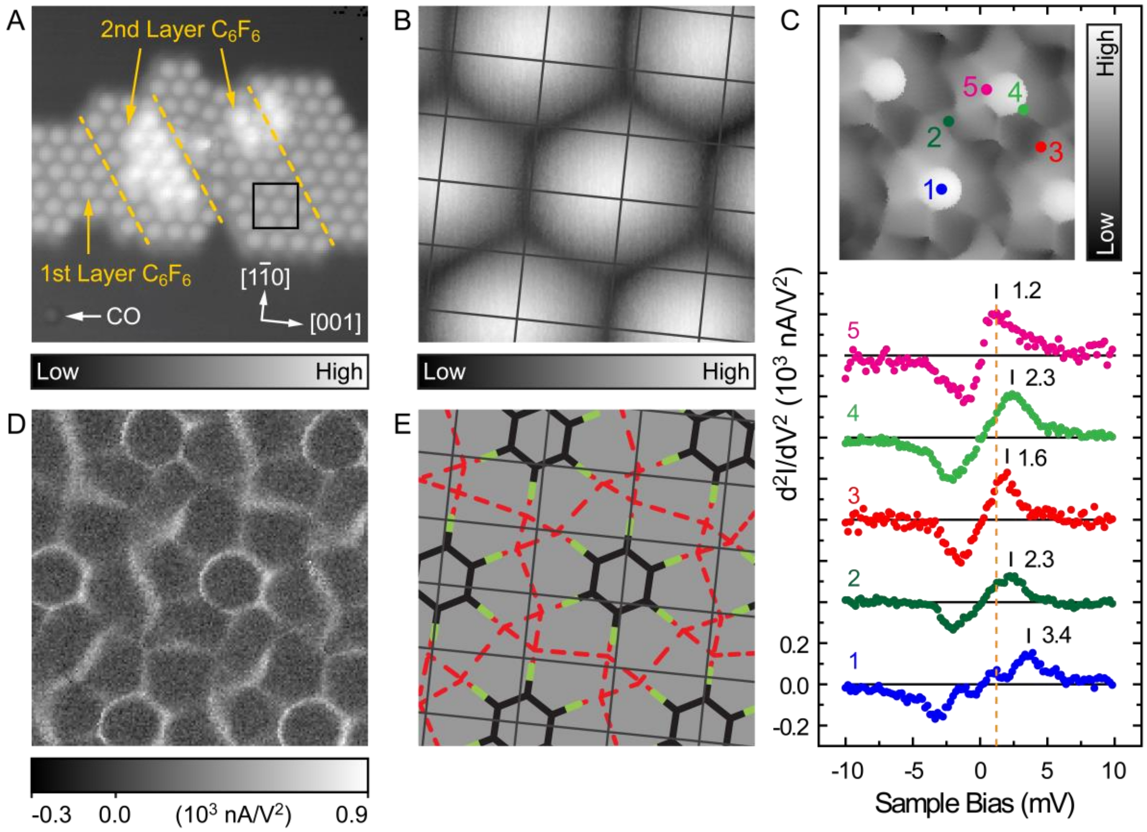
A
2nd Layer C_6F_6
1st Layer C_6F_6
CO
[1$\bar{1}$0]
[001]
Low
High
B
Low
High
C
High
Low
5
4
2
3
1
1.2
2.3
1.6
2.3
3.4
d^2I/dV^2 (10^3 nA/V^2)
0.2
0.0
-0.2
-10
-5
0
5
10
Sample Bias (mV)
D
-0.3
0.0
(10^3 nA/V^2)
0.9
E

Figure 3.3. Theoretical DFT calculations of the C_6F_6 2D hexagonal lattice. (A) The simulated 3D potential energy surface (PES) of the Ag-CO tip and underlying C_6F_6 lattice over the same area as Fig. 3.2D. The tetrahedral Ag tip is set at constant height above the C_6F_6 molecular plane and CO molecule on Ag tip is free to relax. The tip height is set at 3.0 Å from the oxygen center to C_6F_6 molecular plane before CO-tip relaxation. (B) Schematic diagram of the mechanism for itProbe, showing shift of CO-tip vibration over ridges (negative, −, curvature) and valley (positive, +, curvature) of the PES. (C) Schematic diagram of the 2D hexagonal C_6F_6 lattice with lattice constant *d*. The rotation angle θ of the molecule is measured from C-F bond direction and the line connection between the centers of two adjacent molecules. (D) Calculated bonding energy per molecule of the C_6F_6 lattice and final relaxed rotation angle θ as a function of lattice constant *d*, with and without van der Waals correction. The angle is set at 10° initially at each distance *d* prior to relaxation. For comparison, experimentally measured angle is shown as a dot with error bars.

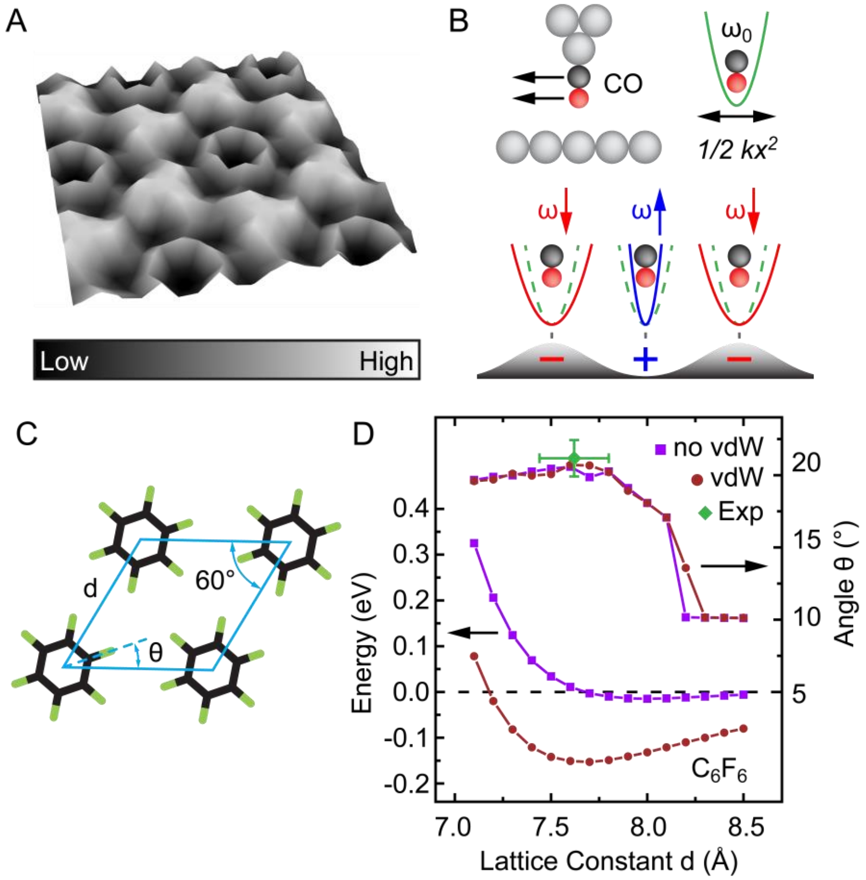
A
Low
High
B
CO
ω0
1/2 kx2
ω
ω
ω
−
+
−
C
d
60°
θ
D
no vdW
vdW
Exp
C6F6
Energy (eV)
Angle θ (°)
Lattice Constant d (Å)
0.4
0.3
0.2
0.1
0.0
-0.1
-0.2
7.0
7.5
8.0
8.5
20
15
10
5

Figure 3.4. C_6Br_6 clusters on Ag(110). (A) Constant current topography of C_6Br_6 trimer, dimer and monomer (inset) with CO-tip (64 Å × 64 Å and 12 Å × 12 Å for inset, set point: 0.1 nA, 10 mV). (B), (C) and (D) Constant height itProbe image at 1.5 mV of dimer, trimer and, monomer shown in (A). Size: 100 × 100 pixels and 18.75 Å × 18.75 Å for (B), 128 × 128 pixels and 20 Å × 20 Å for (C), 96 × 96 pixels and 12 Å × 12 Å for (D). (E) and (F) Schematic diagrams of C_6Br_6 dimer and trimer shown in (B) and (C). The rectangular grids in (A), (E) and (F) show the Ag(110) lattice resolved at close scans with a CO-tip (set point: 0.5 nA, 10 mV).

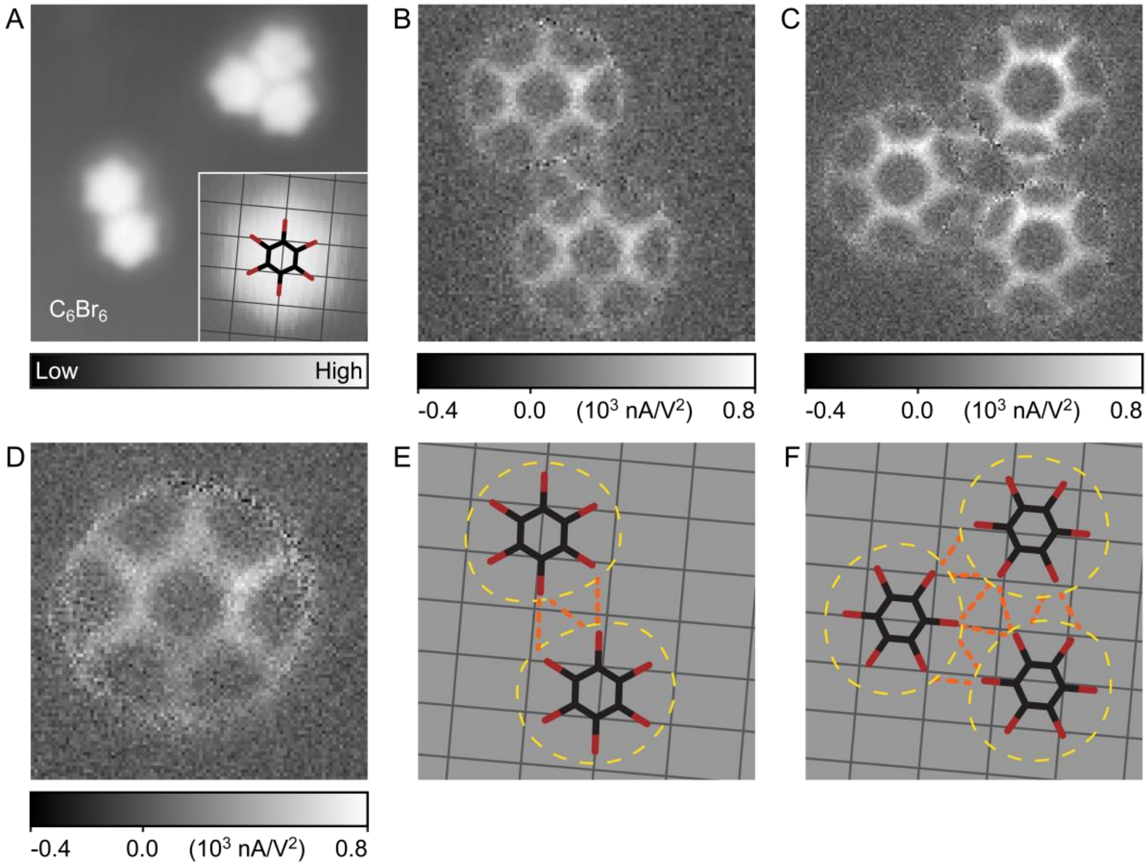
A
C6Br6
Low
High
B
-0.4
0.0
(10^3 nA/V^2)
0.8
C
-0.4
0.0
(10^3 nA/V^2)
0.8
D
-0.4
0.0
(10^3 nA/V^2)
0.8
E
F

Figure 3.5. Determination of adsorption sites for molecules in (A) C_6F_6 self-assembled island, (B) C_6Br_6 monomer, (C) C_6Br_6 dimer and trimer. Superposition of constant current topographic images at different tunneling set points to determine the adsorption sites of molecules within the C_6F_6 island. The image shown in gray scale is taken at a tunneling gap corresponding to 0.12 nA and 60 mV. The tunneling gap to resolve atoms in the Ag(110) lattice with a CO-terminated tip is set at 0.5 nA and 10 mV (the part of the image excluding the gray scale region.) The dimensions for the images are (A) 56 Å × 56 Å, (B) 40 Å × 40 Å, and (C) 64 Å × 64 Å.

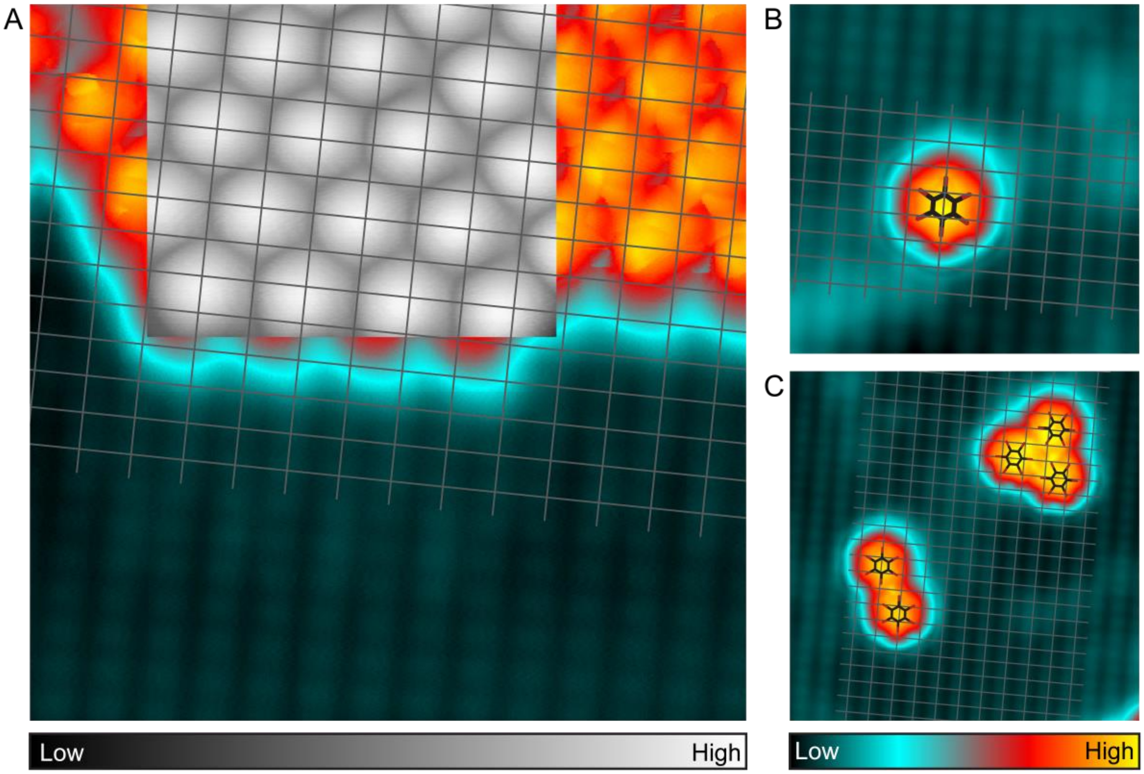
A
B
C
Low
High
Low
High

Figure 3.6. Schematic diagrams of eight high-symmetry adsorption configurations of a single C_6F_6 molecule on Ag(110). They are denoted by short bridge sites (SB1 and SB2), hollow sites (H1 and H2), top sites (T1 and T2) and long bridge sites (LB1 and LB2).

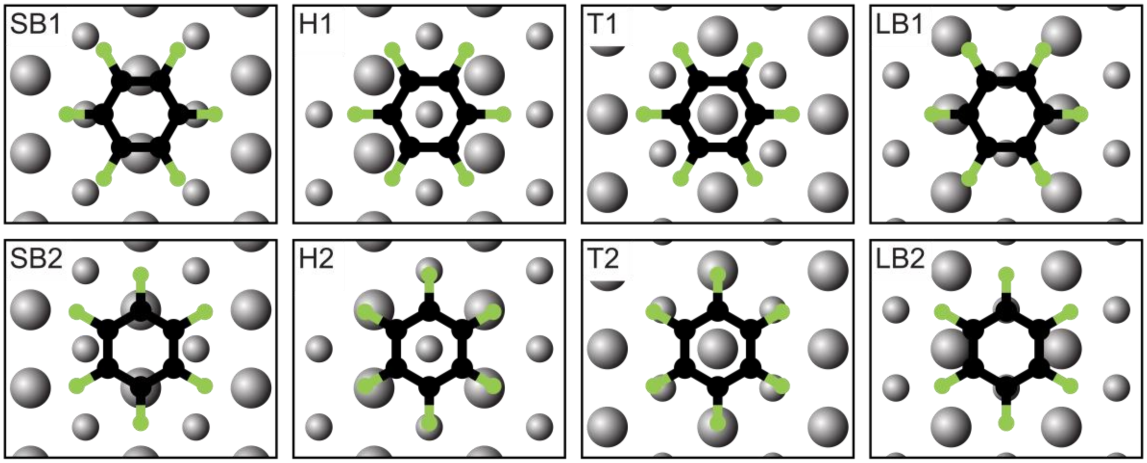
SB1
H1
T1
LB1
SB2
H2
T2
LB2

Figure 3.7. Calculation of the curvature of the potential energy surface (PES) and comparison with the itProbe image of the C_6F_6 lattice. (A) Two-dimensional plot of the smaller principal curvature of the PES in Fig. 3.3A to highlight the ridges and apexes. (B) Overlay of the schematic diagram of C_6F_6 molecules and intermolecular interactions over the curvature plot of PES (C) itProbe image of C_6F_6 island, same as the image shown in Fig. 3.2D.

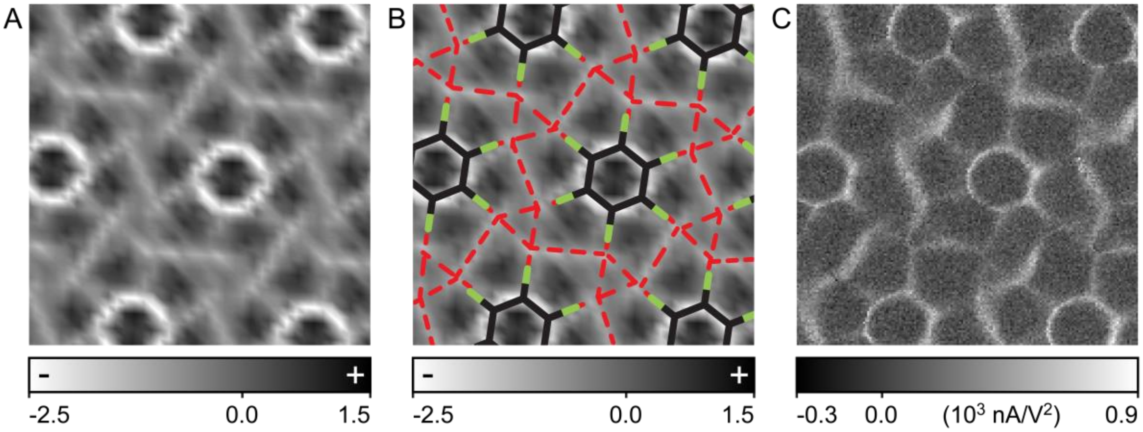A
B
C
-
+
-2.5
0.0
1.5
-
+
-2.5
0.0
1.5
-0.3
0.0
(10^3 nA/V^2)
0.9

Figure 3.8. Monomers of C_6Br_6 with different adsorption configurations on Ag(110). (A) Constant current topography of two C_6Br_6 monomers adsorbed in SB2 configuration (top) and LB1 configuration (bottom). (B) Ag(110) lattice is overlaid on top the topographic image to reveal the adsorption sites of these two molecules. (C) Constant height itProbe image of the yellow box area in (B) recorded at 1.5 mV for the LB1 molecule. Molecule switched configuration during the imaging process as indicated by the red arrow. (D) Constant current topography over the same area as (A) after the switching in (C). (E) Superposition of Ag(110) lattice and topography. (F) Constant height itProbe image of the blue box area in (E) recorded at 1.5mV on the same molecule as (C). Image sizes for (A), (B), (D) and (E) are 48 Å × 48 Å. (C) and (F) are 64 × 64 pixels and 12 Å × 12 Å. The tunneling set point for (A), (B), (D) and (E) is 0.1 nA and 0.1 V.

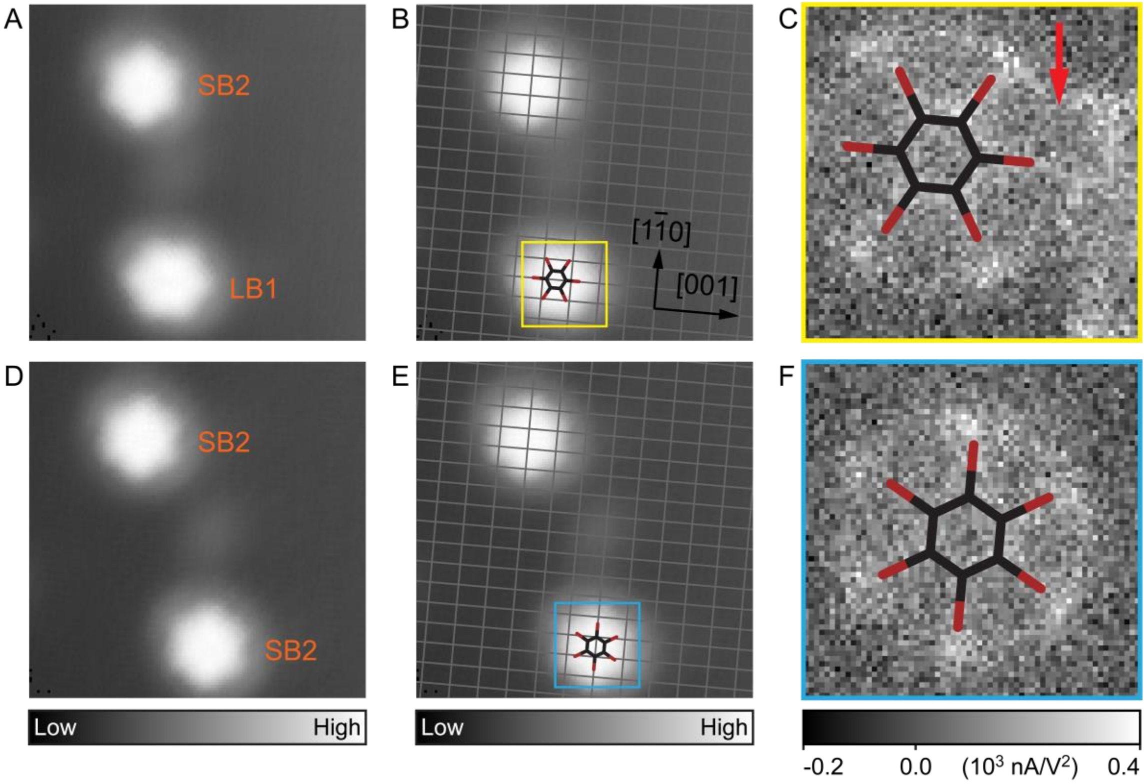
A
SB2
LB1
B
[1$\bar{1}$0]
[001]
C
D
SB2
SB2
E
F
Low
High
Low
High
-0.2
0.0
(10^3 nA/V^2)
0.4

Figure 3.9. Binding energy and molecular orientation calculation for C_6H_6 and C_6Br_6 lattices. (A) Schematic diagram of hexagonal C_6X_6 (X = H, F or Br) lattice for the calculations. The lattice constant and molecular rotation angles are denoted by d and θ, respectively. The angle $\theta = 0°$ corresponds to the orientation where C-X bond in a molecule is aligned with C-X bond of its adjacent molecules. (B) Binding energy of C_6H_6 lattice and molecular rotation angle post-relaxation, with and without van der Waals correction, as a function of lattice constant d. (C) Same calculation as (B) for the C_6Br_6 lattice. Experimentally determined d and θ are shown in green dots with error bars for direct comparison.

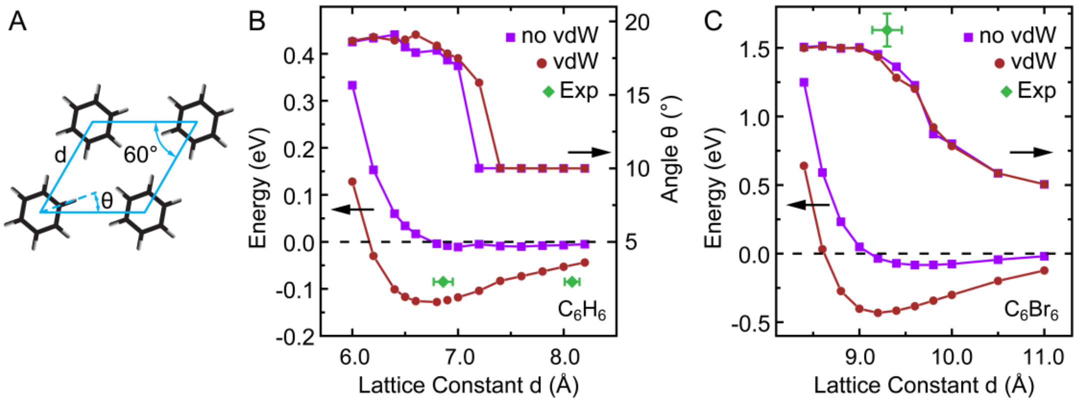
A
d
60°
θ
B
no vdW
vdW
Exp
C$_6$H$_6$
Energy (eV)
Angle θ (°)
Lattice Constant d (Å)
0.4
0.3
0.2
0.1
0.0
-0.1
-0.2
6.0
7.0
8.0
20
15
10
5
C
C$_6$Br$_6$
1.5
1.0
0.5
0.0
-0.5
9.0
10.0
11.0

Figure 3.10. (A) Constant current topography of C_6H_6 close-packed island formed molecule-by-molecule by tip manipulation: image size is 40 Å × 40 Å and tunneling set point is 0.1 nA/20 mV. (B) Superposition of Ag(110) lattice over the topography shown in (A). (C) Illustration of the interaction between two C_6F_6 molecules when they are positioned apart at twice the Ag lattice constant in the [001] direction. (D) Illustration of the interaction between two C_6H_6 molecules separated by twice the Ag lattice constant in the [001] direction. (E) Constant current topography of a C_6H_6 dimer formed by tip manipulation, the image size is 15 Å × 15 Å and the tunneling set point is 0.03 nA/10 mV. (F) Constant height itProbe image at 1.5 mV of the same area as (E). Tunneling feedback is disabled over the center of the molecule on the right side at the tunneling set point = 0.1nA/10mV. Image size is 15 Å × 15 Å and 96 pixels × 96 pixels.

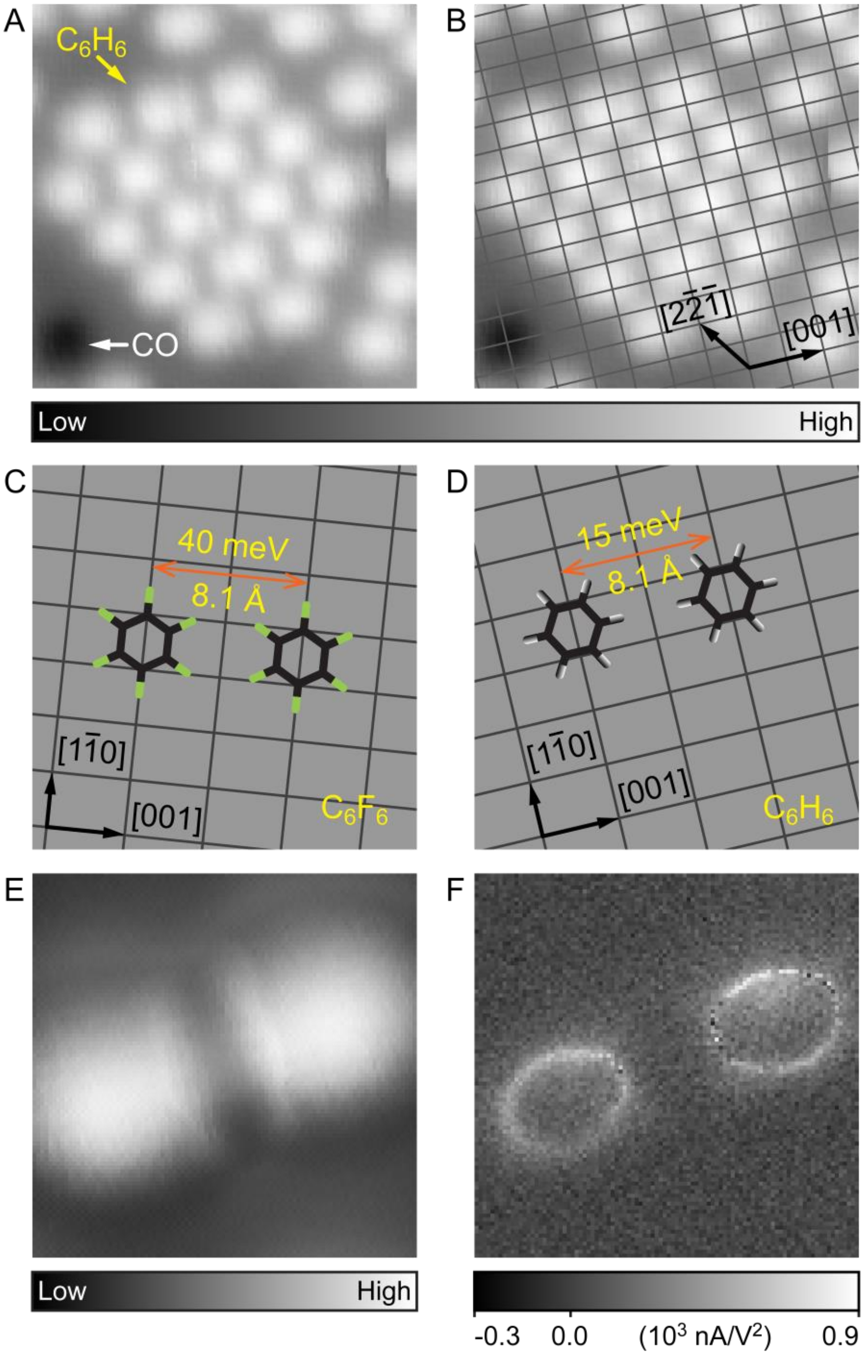
A
C_6H_6
CO
B
$[2\bar{2}\bar{1}]$
[001]
Low
High
C
40 meV
8.1 Å
$[1\bar{1}0]$
[001]
C_6F_6
D
15 meV
8.1 Å
$[1\bar{1}0]$
[001]
C_6H_6
E
F
Low
High
-0.3
0.0
(10^3 nA/V^2)
0.9

Table 3.1. Calculated adsorption energy of isolated benzene molecules C_6X_6 (X = H, F, Br) on the Ag(110) surface, in eV.

C_6X_6	SB1	SB2	LB1	LB2	H1	H2	T1	T2
C_6H_6	0.790	0.785	0.738	0.716	0.710	0.733	0.619	0.624
C_6F_6	0.785	0.790	0.743	0.731	0.695	0.698	0.734	0.728
C_6Br_6	1.470	1.531	1.541	1.448	1.358	1.437	1.492	1.460

Table 3.2. Comparison of calculated lattice constant and rotation angle of the most stable hexagonal lattice structure with experimentally determined values. C-X (X = H, F, or Br) bond length is acquired from our DFT calculation of the most stable lattice with van der Waals correction. And the van der Waals radii for H, F, and Br are also listed for comparison [34].

C_6X_6		C_6H_6	C_6F_6	C_6Br_6
Binding Energy (meV)	vdW	128	153	432
	no vdW	11	15	83
d (Å)	vdW	6.8	7.7	9.2
	no vdW	7.0	8.0	9.6
	Exp.	8.08±0.07/6.86±0.09	7.85±0.05/7.50±0.08	9.30±0.16
θ (°)	vdW	18.4	20.7	19.4
	no vdW	17.0	18.1	17.3
	Exp.	N/A	21.2±1.3	21.3±1.2
C-X (Å)		1.092	1.345	1.892
X vdW Radius (Å)		1.20	1.46	1.86

Bibliography

[1] R. F. Service, Science **309**, 95 (2005).

[2] P. Metrangolo, F. Meyer, T. Pilati, G. Resnati, and G. Terraneo, Angew. Chemie Int. Ed. **47**, 6114 (2008).

[3] L. C. Gilday, S. W. Robinson, T. A. Barendt, M. J. Langton, B. R. Mullaney, and P. D. Beer, Chem. Rev. **115**, 7118 (2015).

[4] P. Metrangolo, G. Resnati, T. Pilati, and S. Biella, in *Halogen Bond. Fundam. Appl.*, edited by P. Metrangolo and G. Resnati (Springer, Berlin, Heidelberg, 2008), pp. 105–136.

[5] A. Mukherjee, S. Tothadi, and G. R. Desiraju, Acc. Chem. Res. **47**, 2514 (2014).

[6] P. Auffinger, F. A. Hays, E. Westhof, and P. S. Ho, Proc. Natl. Acad. Sci. **101**, 16789 (2004).

[7] Y. Lu, T. Shi, Y. Wang, H. Yang, X. Yan, X. Luo, H. Jiang, and W. Zhu, J. Med. Chem. **52**, 2854 (2009).

[8] T. Clark, M. Hennemann, J. S. Murray, and P. Politzer, J. Mol. Model. **13**, 291 (2007).

[9] P. Politzer, P. Lane, M. C. Concha, Y. Ma, and J. S. Murray, J. Mol. Model. **13**, 305 (2007).

[10] J. Trnka, R. Sedlak, M. Kolář, and P. Hobza, J. Phys. Chem. A **117**, 4331 (2013).

[11] S. Kawai, A. Sadeghi, F. Xu, L. Peng, A. Orita, J. Otera, S. Goedecker, and E. Meyer, ACS Nano **9**, 2574 (2015).

[12] K. Reichenbächer, H. I. Süss, and J. Hulliger, Chem. Soc. Rev. **34**, 22 (2005).

[13] S. J. Stranick, M. M. Kamna, and P. S. Weiss, Science **266**, 99 (1994).

[14] D. B. Dougherty, M. Feng, H. Petek, J. T. Yates, and J. Zhao, Phys. Rev. Lett. **109**, 266802 (2012).

[15] J. Zhao, M. Feng, D. B. Dougherty, H. Sun, and H. Petek, ACS Nano **8**, 10988 (2014).

[16] C. Chiang, C. Xu, Z. Han, and W. Ho, Science **344**, 885 (2014).

[17] D. Yuan, Z. Han, G. Czap, C.-L. Chiang, C. Xu, W. Ho, and R. Wu, J. Phys. Chem. Lett. **7**, 2228 (2016).

[18] L. Gross, F. Mohn, N. Moll, P. Liljeroth, and G. Meyer, Science **325**, 1110 (2009).

[19] D. G. de Oteyza, P. Gorman, Y.-C. Chen, S. Wickenburg, A. Riss, D. J. Mowbray, G. Etkin, Z. Pedramrazi, H.-Z. Tsai, A. Rubio, M. F. Crommie, and F. R. Fischer, Science **340**, 1434 (2013).

[20] J. Zhang, P. Chen, B. Yuan, W. Ji, Z. Cheng, and X. Qiu, Science **342**, 611 (2013).

[21] N. Moll, B. Schuler, S. Kawai, F. Xu, L. Peng, A. Orita, J. Otera, A. Curioni, M. Neu, J. Repp, G. Meyer, and L. Gross, Nano Lett. **14**, 6127 (2014).

[22] C.-S. Guo, X. Xin, M. A. Van Hove, X. Ren, and Y. Zhao, J. Phys. Chem. C **119**, 14195 (2015).

[23] P. Hapala, G. Kichin, C. Wagner, F. S. Tautz, R. Temirov, and P. Jelínek, Phys. Rev. B **90**, 085421 (2014).

[24] P. Hapala, R. Temirov, F. S. Tautz, and P. Jelínek, Phys. Rev. Lett. **113**, 226101 (2014).

[25] B. C. Stipe, M. A. Rezaei, and W. Ho, Science **280**, 1732 (1998).

[26] T. T. T. Bui, S. Dahaoui, C. Lecomte, G. R. Desiraju, and E. Espinosa, Angew. Chemie Int. Ed. **48**, 3838 (2009).

[27] R. Strohmaier, C. Ludwig, J. Petersen, B. Gompf, and W. Eisenmenger, Surf. Sci. **318**, L1181 (1994).

[28] H. Walch, R. Gutzler, T. Sirtl, G. Eder, and M. Lackinger, J. Phys. Chem. C **114**, 12604 (2010).

[29] J. K. Yoon, W. Son, K.-H. Chung, H. Kim, S. Han, and S.-J. Kahng, J. Phys. Chem. C **115**, 2297 (2011).

[30] W. Wang, X. Shi, S. Wang, M. A. Van Hove, and N. Lin, J. Am. Chem. Soc. **133**, 13264 (2011).

[31] Q. Fan, T. Wang, L. Liu, J. Zhao, J. Zhu, and J. M. Gottfried, J. Chem. Phys. **142**, 101906 (2015).

[32] J. Shang, Y. Wang, M. Chen, J. Dai, X. Zhou, J. Kuttner, G. Hilt, X. Shao, J. M. Gottfried, and K. Wu, Nat. Chem. **7**, 389 (2015).

[33] H. Huang, Z. Tan, Y. He, J. Liu, J. Sun, K. Zhao, Z. Zhou, G. Tian, S. L. Wong, and A. T. S. Wee, ACS Nano **10**, 3198 (2016).

[34] S. Alvarez, Dalt. Trans. **42**, 8617 (2013).

[35] B. C. Stipe, M. A. Rezaei, and W. Ho, Rev. Sci. Instrum. **70**, 137 (1999).

[36] G. Kresse and J. Furthmüller, Comput. Mater. Sci. **6**, 15 (1996).

[37] J. P. Perdew, K. Burke, and M. Ernzerhof, Phys. Rev. Lett. **77**, 3865 (1996).

[38] J. Klimeš, D. R. Bowler, and A. Michaelides, J. Phys. Condens. Matter **22**, 022201 (2010).

[39] H. W. Guggenheimer, in *Differ. Geom.* (Dover Publications, New York, 1977), pp. 206–260.

Chapter 4

Quantitative Understanding of van der Waals Interactions by Analyzing the Adsorption Structure and Low-Frequency Vibrational Modes of Single Benzene Molecules on Silver[*]

4.1 Abstract

The combination of a sub-Kelvin scanning tunneling microscope (STM) and density functional calculations incorporating van der Waals (vdW) corrections has been used successfully to probe the adsorption structure and low frequency vibrational modes of single benzene molecules on Ag(110). The inclusion of optimized vdW functionals and improved C6-based vdW dispersion schemes in density functional theory is crucial for obtaining the correct adsorption structure and low-energy vibrational modes. These results demonstrate the emerging capability to quantitatively probe the van der Waals interactions between a physisorbed molecule and an inert substrate.

---

[*] This chapter by D. Yuan, Z. Han, G. Czap, C. Chiang, C. Xu, W. Ho and R. Wu has been previously published under the same title in *The Journal of Physical Chemistry Letters* **7**, 2228-2233 (2016). D.Y. and Z.H. contributed equally to this work. Copyright © 2016 American Chemical Society.

4.2 Article

Understanding of van der Waals (vdW) interactions is essential for the control of many surface processes such as physisorption, sliding friction, epitaxial growth, and molecular self-assembly [1–5]. Physisorption systems with benzene on coinage metal surfaces have been the prototypes for studies of weak van der Waals forces. Although extensive experimental results are available, particularly binding energies of benzene obtained through temperature programmed desorption (TPD) measurements [6–11], they are mostly obtained from ensemble-averaged approaches that require high molecular coverages and collect data from different adsorption configurations. Therefore, these experimental data are not adequately reliable for the establishment of the fundamental understanding of van der Waals forces between adsorbates and substrates through direct comparison with density functional theory (DFT) calculations. One example is for benzene on Ag(111): although an accuracy of 30-50 meV was claimed recently, the adsorption energy of benzene varies from 0.43 to 0.80 eV in early reports, based on fitting broad TPD curves [6–10]. Naturally, physisorption systems can be better characterized by measuring their external vibrational modes for which the energies mostly depend on the strength of weak adsorbate-substrate interactions [12,13]. Again, it is a challenging task for ensemble-averaged experiments to resolve these vibrational modes since their energies are typically smaller than 15 meV and also sensitively change with adsorption geometry, aside from other technical issues such as energy resolution and instrumental sensitivity [9,13–15].

Obviously, it is desired to probe physisorption systems at the level of single molecule with the scanning tunneling microscope (STM) that provides vibration energies using the inelastic electron tunneling spectroscopy (IETS) [16], along with rich local information such as the molecular structure, orientation and coupling to the neighboring environment. Yet, studies of the adsorption structure and vibrational properties of single benzene molecules on coinage metal surface are nontrivial because (1) benzene diffuses easily on the substrate [17] and (2) the peaks of IETS are still too broad even at 4K. Gawronski *et al.* analyzed physisorption and chemisorption of dichlorobenzene on Au(111) but failed to resolve external vibrational modes of physisorbed species [18]. Pascual *et al.* found that vibrations of benzene on Ag(110) are sensitive to the change of adsorption sites [14]. They resolved two vibrational modes at 4 and 19 meV, but it is arguable if these modes actually belong to benzene since the vibrations of carbon monoxide molecules on Ag(110) give these two energies.

In this Letter, we report results from joint first-principles calculations with mili-Kelvin STM measurements of single benzene molecules on the Ag(110) substrate. The low-energy external vibrations were measured by STM-IETS and the adsorption site and orientation of physisorbed benzene were resolved by the inelastic tunneling probe (itProbe) [19]. At the ultra-low temperature the spectroscopic resolution is improved to sub-meV for the low-energy external vibrational modes, and meaningful comparison can be made with theoretical calculations. To provide clues for the rational selection and optimization of the van der Waals corrections in density functional theory calculations, many latest vdW methods were adopted to examine the vibration energies. We demonstrate quantitative agreement between theory and experiment at the single molecule level for the understanding of weak van der Waals forces.

The experiments were carried out in a home-built, sub-Kelvin (600 mK) STM with a base pressure of 5×10^{-11} Torr. The Ag(110) surface and the electrochemically etched silver tips were prepared by cycles of Ne^+ sputtering and annealing. Benzene (C_6H_6 from Sigma Aldrich) was purified with repeated freeze-pump-thaw cycles. Carbon monoxide (CO) and submonolayer benzene molecules (~0.1ML) were sequentially deposited onto the Ag surface at 25 K. The sample and STM scanner were subsequently cooled down to 600 mK for spectroscopy and imaging. The CO-functionalized tip is crucial for obtaining high-resolution topographic and itProbe images [19]. A CO molecule was transferred to the Ag tip by scanning over the CO on the surface at a tunneling gap corresponding to 1 mV sample bias and 1 nA tunneling current. STM-IETS over clean Ag surface was performed to verify the presence of the CO on the tip by its characteristic frustrated translational and rotational modes [19].

DFT calculations were performed using the plane-wave based Vienna ab initio simulation package (VASP) [20,21]. The interaction between ion and core electrons was described by the projector augmented wave (PAW) method [22]. and plane waves with an energy cutoff of 700 eV were used to expand the Kohn-Sham wave functions. The Ag(110) surface was modeled with a $p(4 \times 4)$ unit cell with a 4-layer Ag slab and an 18 Å vacuum. The two bottommost Ag layers were frozen at their bulk positions during geometric optimization. To calculate the low-energy external modes, the adsorption geometries need to be optimized with extremely high converging thresholds: 0.002 eV/Å for forces and 10^{-8} eV for the total energy. In all calculations, we used a $2 \times 3 \times 1$ k-points mesh generated by the Monkhorst-Pack scheme [23]. Test calculations with a $4 \times 6 \times 1$

k-points mesh indicated that the energies of the low-energy modes changed by less than 0.5 meV.

Several schemes have been developed to describe the long-range dispersion interactions in DFT calculations [24–26], starting from the non-local correlation functional proposed by Dion *et al.* [24]. An alternative DFT-D approach was also proposed, by adding a C_6R^{-6} correction term to the Kohn-Sham DFT energy [27]. Depends on the way of constructing the C_6 coefficient, several versions of the DFT-D method such as DFT-D2 [27], DFT-D3 [28,29], DFT-TS [30] and DFT-TS+SCS [31,32] have been developed and tested. In this work, we employed ten different vdW-inclusive approaches (vdW-revPBE, vdW-rPW86, vdW-optPBE, vdW-optB88, and vdW-optB86b, DFT-D2, DFT-D3, DFT-D3(BJ), DFT-TS, and DFT-TS+SCS) in our DFT calculations so as to test their applicability for the description of the weak interaction between benzene and Ag.

A constant current topography in Figure 4.1a shows isolated C_6H_6 coadsorbed with CO on Ag(110). Bright elongated protrusions are C_6H_6 molecules and donut-shaped central depressions are CO molecules. The atomic contrast of the Ag(110) surface is resolved in the zoom-in view in Figure 4.1b, and in Figure 4.1c, the Ag(110) lattice is superimposed over the resolved image. By overlaying Figure 4.1c on top of Figure 4.1a and extrapolating it to extend the lattice mesh over the entire region, each CO molecule is determined to adsorb on top of an Ag atom (atop site), and each benzene molecule is centered between two nearest neighboring Ag atoms along the $[1\bar{1}0]$ direction (short-bridge site). It should be pointed out that the central bright feature of benzene in Figure 4.1b and 4.1c is caused by the CO motion on the tip when it is brought close to the benzene molecule on the surface. The asymmetric appearance is due to the slight asymmetry of the CO-tip that becomes magnified at close separation between the two molecules.

As with other low index coinage metal surfaces [33,34], benzene adsorbs flat on the Ag(110) terrace. Its orientation can be determined with the itProbe [19], as shown in Figure 4.1d. As the CO-terminated tip is positioned over the molecule, the CO molecule senses a spatially varying potential landscape, resulting in significant energy shift of its frustrated translational mode [19,35]. These energy shifts are caused by the local curvature of the potential energy surface (PES) of the adsorbed molecule and the CO on the tip. The curvature in PES is related to the gradient in the force between the CO and the adsorbed molecule.

In Figure 4.1e, the d^2I/dV^2 point spectra show spectral shift for the CO-tip over three specified points of the benzene molecule, as marked in Figure 4.1d. The vibrational excitation energy of the frustrated translation mode of CO on the tip is 2.4 meV over the Ag surface. The excitation energy redshifts to 1.7 meV when the CO-tip is positioned over the bright elongated hexagon in the itProbe image (Figure 4.1d), indicating a negative curvature in the PES. In contrast, a blue shift to 2.9 meV occurs when CO-tip is positioned inside the carbon ring, suggesting region of positive curvature in the PES. By monitoring the d^2I/dV^2 signal of the CO-tip at 1.5 mV as it scans over the benzene molecule at a fixed height, an elongated hexagon revealing the orientation of the benzene molecule is obtained in Figure 4.1d. A scaled model of a free benzene molecule is superimposed on the itProbe image. Combined with the topographic image in Figure

4.1b, the adsorption geometry of benzene on Ag(110) is identified as the SB1 configuration in Figure 4.2.

We note that the carbon ring in the itProbe image is 60%-70% larger in size than the known free benzene structure. Similar results were also reported for hydrogenated carbon rings obtained by qPlus AFM with Cu-CO tip [36,37]. The larger molecular size could be a consequence of the following effects from tip-CO interacting with adsorbed benzene: (1) The CO on the tip tilts in the presence of short-ranged attractive or repulsive forces [36–39]; (2) the charge density (and ridges in the PES) of adsorbed C_6H_6 extends beyond the benzene ring [37,40]; (3) the underlying Ag(110) surface with a rectangular unit cell influences the PES. As shown in Figure 4.1a, 4.1b, 4.1c and 4.1d, benzene molecules are all elongated along the [001] direction due to the rectangular symmetry of the underlying Ag(110) surface. This elongation can also be found in the constant charge density contour of total charge density map 4 Å above the benzene plane, as displayed in the inset of Figure 4.3a. Consistent with the itProbe image in Figure 4.1d, the spatial extent of the ridges in the charge density around the benzene molecule is slightly larger than its skeletal structure of the molecule.

Four possible adsorption sites and eight high symmetry configurations for benzene on Ag(110) in Figure 4.2 were treated by DFT. We evaluated the quality of different vdW-inclusive methods for quantitative description of the weak benzene-Ag interaction by considering five different vdW functionals and five vdW-correction methods, along with the GGA-PBE functional. The strength of the benzene-Ag interaction can be characterized by the adsorption energy, which is defined by $E_{ad}=E_{benzene/Ag(110)}-E_{Ag(110)}-E_{benzene}$, where $E_{benzene/Ag(110)}$, $E_{Ag(110)}$, and $E_{benzene}$ are the total energies of benzene on Ag(110), the clean Ag(110) slab, and the isolated benzene molecule, respectively. As shown Table 4.1, the vdW-optB86b (in fact all vdW functionals) yields the largest adsorption energy for the short bridge (SB1) geometry, in agreement with the experimental results shown in Figure 4.1, although the SB2 geometry is only a few meV higher in energy. It is not a surprise that without including vdW interaction PBE produces unreasonably low E_{ad} and large $d_{C\text{-}M}$, and hence is inadequate even for a qualitative description of the present system. The projected density of states (PDOS) from vdW calculations in Figure 4.3a show slight broadening of the π orbitals of benzene from interaction between p_z and d_z^2 orbitals. Furthermore, small electron donation from Ag and H atoms to the C-ring can be seen in Figure 4.3b and 4.3c. These suggest weak but noticeable hybridization between benzene and Ag(110), even though the vdW interaction plays the dominate role in this physisorption system. Our DFT results also show small energy barrier of tens of meV for the diffusion of benzene along the [001] direction on the substrate (cf. Figure 4.5 and discussions in Supplementary Materials). Experimentally, we found that benzene molecules can be laterally manipulated during constant current topography with sample bias greater than 60 mV.

The comparison in this study between experiment results and theoretical calculations allows the determination of the vdW approach that best describes the present physisorption system. As listed in Table 4.3, the adsorption energies and geometrical parameters for SB1 change with the choice of different vdW functionals and vdW-correction methods, as was also found in previous theoretical calculations [33]. As mentioned earlier, the adsorption energy of benzene on Ag(111) surface changes from 0.43 to 0.80 eV by TPD measurements [6–10]. compared to theoretical values of 0.52 to

1.29 eV from DFT calculations with different vdW approaches [9,10,29,33,34,41,42]. Here we compare the calculated vibrational energies of external modes with data from STM-IETS measurements to assess the accuracy of different vdW approaches.

Three vibrational features are detected by STM-IETS at 1.2 mV, 6.9 mV and 12.7 mV, as shown in Figure 4.4a. The latter two modes only appear over benzene and are attributed to the external vibrational modes of benzene on Ag(110). The 1.2 meV feature is also present in the background spectrum. However, the magnitude of this feature is enhanced over the adsorbed benzene and is attributed to the presence of a low energy vibrational mode of benzene. We want to emphasize that these three modes were not observed in a previous experiment on the same system [14], where the reported bare tip topography, molecular tip topography, and STM-IETS peaks instead are consistent with those of CO on Ag(110) [19,43,44]. Furthermore, in the Supplementary Materials we have reproduced for direct comparison similar bare tip topography, CO-tip topography, and IETS spectra of CO on Ag(110) with comparable experimental parameters as used in Ref. [14].

Calculations by DFT-vdW can capture 5-6 external vibrational modes which are listed in Table 4.2, and Table 4.3 [45]. The results are compared to STM-IETS in Figure 4.4b. The two modes at 6.9 meV and 12.7 meV are assigned to the frustrated rotational modes of benzene on Ag(110) surface, FR_y and FR_x. The translational FT_y and bouncing FT_z mode may contribute to the width of the 6.9 meV mode. The extremely low-energy vibrational excitation at 1.2 meV is most likely the FR_z mode.

Among the frustrated rotational and translational modes, the FR_x mode is calculated to have the highest energy and its comparison to the experimental peak at 12.7 meV can be effectively used to discriminate the different vdW approaches. The GGA-PBE, vdW-revPBE, vdW-rPW86 and DFT-D2 functionals in Figure 4.4b can be seen to be inaccurate for describing benzene on Ag(110) and are similarly doubtful for other physisorption systems. Better agreement is obtained for the “opt” vdW functionals (optPBE, optB88, and optB86b), using the “less repulsive” exchange functionals within the vdW-revPBE scheme [46]. With the coordination number dependent C_6 coefficients, DFT-D3 [28] can produce fairly accurate vibrational energies due to the inclusion of three-body dispersion coefficient [34], in comparison to the higher vibrational energies obtained by DFT-D3(BJ) [28]. Our calculations show that the energies of FR_x and FR_z match well with experimental values using DFT-TS [30,32]. However, the differences in energy of the external vibrational modes are less than 1.5 meV for benzene in the SB1 and SB2 geometries calculated with vdW-optB86b and DFT-D3 (see Table 4.2).

In conclusion, we demonstrate the determination of the adsorption configuration and external vibrational modes of single benzene molecules on Ag(110) using STM-IETS measurement and DFT-vdW calculation. Accurate description of weakly interacting systems requires optimized vdW functionals and improved dispersion-correction vdW methods. Sub-Kelvin itProbe and STM-IETS enable clear determination of the adsorption site, structure, and external vibrational modes at the single molecule level for theoretical analysis. The present study provides the foundation for quantitative understanding of weak vdW interaction in molecular based systems.

4.3 Supplementary Materials

Here we compare DFT results from PBE and vdW-optB86b functionals in Table 4.1. The GGA functional predicts SB2 as the ground state geometry whereas the vdW-optB86b functional gives SB1 as the ground state geometry.

We studied the diffusion energy barriers of benzene on Ag(110) using the nudged-elastic-band (NEB) simulations [47,48]. We considered four diffusion pathways, referring to the adsorption sites in Figure 4.2, *i.e.*, SB1→T1→SB1, LB1→T1→LB1, SB1→H1→SB1, and H2→LB2→H2 (see Figure 4.5). Interestingly, the barrier is zero for benzene moving between two adjacent high symmetry adsorption sites, i.e., T→SB, SB→LB, LB→H, and H→T. The diffusion barrier along each route hence comes from the difference of adsorption energies between them.

We found that the Ag top site (T) corresponds to the transition state for benzene diffusion along either the $[1\bar{1}0]$ or [001] direction and the energy barrier is 0.186 eV or 0.134 eV for the SB1→T1→SB1 or LB1→T1→LB1 pathway, respectively. However, benzene can easily diffuse in other two pathways SB1→H1→SB1 and H2→LB2→H2, and the energy barriers are as small as 0.073 eV and 0.033 eV, respectively. This qualitatively explains our STM observations: benzene molecules on the terrace of Ag(110) could be laterally manipulated with the CO-terminated Ag tip along the [001] direction perpendicular to the short-bridge atomic row during constant current scanning. Manipulation along the $[1\bar{1}0]$ direction could also occur but with more difficulty. For example, manipulation along the [001] direction with a CO-tip could be achieved at a set point of 60 mV and 100 pA, while requiring a higher electron energy at a set point of 100 mV and 100 pA along the $[1\bar{1}0]$ direction. At step edges of Ag(110) substrate, benzene molecules are much more stable, and they cannot be manipulated with the CO-tip even at a closer tip-sample distance. Moreover, the inelastic electron tunneling signals corresponding to the low-energy external modes of benzene are much less prominent for benzene adsorbed at step edges of Ag(110).

We calculated the vibrational frequencies of benzene adsorbed in the SB1 geometry on Ag(110), listed in Table 4.2, using finite differences and density functional perturbation theory. Comparisons of vibrational energies were made to benzene in the gas phase and also adsorbed in the SB2 geometry. The external vibrational energies are reorganized in Table 4.3. To reduce the computation time, we fixed the atomic positions of Ag slab during the calculation of the Hessian matrix, i.e., the matrix of the second derivatives of the energy with respect to the atomic positions. The displacement of atomic positions is ±0.01 Å for each direction. The energies of extremely low-energy modes, *i.e.*, FT_x and FR_z, strongly depend on the calculation precisions, e.g., k-points meshes, energy cutoff of plane waves, and converging thresholds. To precisely calculate the low-energy external modes, the adsorption geometries need to be optimized with extremely precise converging thresholds: 0.002 eV/Å for forces and 10^{-8} eV for the total energy. The energy cutoff of plane waves should be increased greatly, and 700 eV cutoff was used in our calculations. A mesh of $2\times3\times1$ k-points was used. We tested $4\times6\times1$ k-points mesh and the energies of the low-energy modes change by less than 0.5 meV. Nonetheless, some imaginary frequencies are obtained for the extremely low-energy modes within the numerical limitation of DFT calculation (see Table 4.2 and Table 4.3). To supplement the discussion in the text, we depict the relative amplitude and direction of each atom in benzene for different external vibrational modes on the Ag(110) substrate (see Figure 4.6).

To establish the reliability of our theoretical approach for the determination of vibrational energies of benzene, we also calculated the vibrational energies for a free benzene molecule. Among the 30 internal vibrational modes displayed in Table 4.2, the softest one has energy of 50 meV, corresponding to the deformation of the carbon ring. The vibrational energies agree well with experimental data for benzene molecules in the gas phase [49]. The weak van der Waals interaction between benzene and Ag substrate modifies the intramolecular forces and energies of the internal vibrational modes of benzene by 1~3% on Ag(110) (see Table 4.2). Similar results were reported for benzene adsorption on the Al(111) surface [11]. in contrast to the changes on the more reactive transition metals where the internal vibrational modes of benzene may shift their energies by up to 20 meV [50].

Pascual *et al.* reported the external vibrational modes of benzene (C_6H_6) on Ag(110) surface [14], which is the same system as we studied here. The properties of the "chemisorbed benzene species" on Ag(110) terrace described in that letter are very different from those obtained by our measurements in the present work. However, their data match closely the adsorption of carbon monoxide (CO) on Ag(110), both the topographic images and vibrational spectra by STM-IETS. CO is a common background gas in ultrahigh vacuum chambers, so its presence on a surface not intentionally prepared with CO is not necessarily unreasonable to expect. We dose CO molecules on Ag(110) at 25 K and show the measurements on CO/Ag(110) with bare metal tip and CO-terminated tip at 600 mK in Figure 4.7 using similar experimental settings as in the reported experiment [14].

In the bare metal tip constant current topography of the previous study [14]. “chemisorbed benzene molecules” on Ag(110) terrace were imaged as round depressions, in contrast with protrusions in our experiment. In addition, Pascual *et al.* obtained topography of the “benzene” molecule using a tip functionalized with another “benzene” molecule. These images provide atomic resolution of the surface and indicate a top-site adsorption geometry for the surface molecule. Further, the topography of the molecule shows a central bright protrusion surrounded by several dark lobes, which in turn are surrounded by a circular feature. The molecule size and contrast in the constant current topographic images over “benzene” with the bare tip and “benzene-tip” appear the same as an adsorbed CO molecule scanned with a bare metal tip [19] and CO-tip [43,44]. We reproduced these images over a CO molecule using a bare metal tip with exactly the same tunneling set point (Figure 4.7a) and CO-terminated tip with the same tunneling junction resistance (Figure 4.7b).

The on-top adsorption site mentioned above contradicts with the experimental and theoretical results of our current study (Figure 4.1 and Table 4.1) and others [33], but matches the CO adsorption site on Ag(110) [43,44], which is also shown in Figure 4.7b.

Their measured vibrational excitation energies, 4 meV and 19 meV, coincide with the reported vibrational energies of the frustrated translation and frustrated rotation of CO on Ag(110), respectively [19,44]. The 39 meV mode can be assigned to the CO bouncing mode against the surface [51,52]. In our recent STM-IETS experiment, we found three external vibrational modes of CO-Ag below 50 meV. Their energies are 2.3 meV, 19.4

meV and 37.4 meV for CO on Ag(110) with bare Ag tip, and 2.0 meV, 18.1 meV and 35.7 meV for the CO-terminated Ag tip over Ag(110). These results will be featured in a future publication. For comparison, we repeated STM-IETS measurement over CO and Ag(110) background with the same tunneling set point and bias modulation shown in Figure 4.7c. The energies of the CO hindered vibrational excitations are found at 2.9 meV and 19.7 meV, which are very close to the values obtained by Pascual *et al*., and the small differences are within their STM-IETS energy resolution.

It is also worth mentioning that the combined conductance increase $\Delta\sigma/\sigma$ of the two vibrational excitations at 4 meV and 19 meV is about 10% in their experiment, which is in good agreement with the present measurement in Figure 4.7c.While for the three external vibrational modes of benzene in our measurement shown in Figure 4.4a, the differential conductance change for each mode is around 1% or less.

Furthermore, in our experiment all the benzenes molecules on Ag(110) terrace have a low diffusion barrier even at a much lower temperature of 600 mK compare to 5 K in their experiment. We found that the benzene molecules were laterally dragged by the tip during scanning at the same set point (1.6 nA and 0.1 V) used for constant current topography in the previous experiment [14].

On the basis of these findings, we conclude that we cannot reliably compare our measured vibrational excitation energies for benzene with those found by Pascual *et al.* [14]. We are inclined to conclude that the "chemisorbed benzene" molecules they identified on Ag(110) were in fact CO molecules.

This work was supported by the National Science Foundation Center for Chemical Innovation on Chemistry at the Space-Time Limit (CaSTL) under Grant No.

CHE-1414466 (DY), the Chemical Science, Geo- and Bioscience Division, Office of Science, U.S. Department of Energy, under Grant No. DE-FG02-04ER15595 (ZH, GC) and Grant No. DE-FG02-06ER15826 (CX), and the Condensed Matter Physics Program, Division of Materials Research, National Science Foundation Grant No. DMR-1411338 (CJ). DY also acknowledges the development plan for young teacher of Hunan University and the scholarship from China Scholarship Council (CSC) under Grant No. 201208430282. Some of the calculations were performed using the National Supercomputing Center in Changsha, China.

Figure 4.1. Imaging single benzene molecules. (a) and (b) Constant current topography of benzene (protrusions) and CO (depressions) coadsorbed on Ag(110) at 600 mK, scanned with a CO-terminated tip: (a) set point: V = 10 mV and I = 20 pA, size: 80Å×80 Å, (b) zoom-in scan of the blue box in (a) with smaller tunneling gap to resolve surface Ag atoms, and (c) overlaid with dotted mesh based on the atomically resolved lattice, set point: V = 1.5 mV and I = 100 pA, size: 25 Å×25 Å. (d) Constant height itProbe image of the orange boxed area in (c). Feedback was first turned off at the center of molecule with 10 mV sample bias and 80 pA tunneling current, then d^2I/dV^2 was recorded at 1.5 mV sample bias while the tip was held at a constant height throughout the imaging process, size: 9.0 Å×9.0 Å. The itProbe image is superimposed with a scaled benzene structure. (e) STM-IETS of CO on the Ag tip recorded at constant height set as in (d). The tip was then sent to one of the three locations, indicated by the colored dots in (d), for taking the corresponding colored spectrum. Spectra are vertically displaced by 200 nA/V^2 gap for clarity. For both (d) and (e), bias voltage modulation was set to 1.5 mV_{RMS} at 311.11 Hz for recording d^2I/dV^2 signals with the lock-in amplifier. All the experimental images presented in this work are free from any nonlinear post-processing, such as filtering or smoothing.

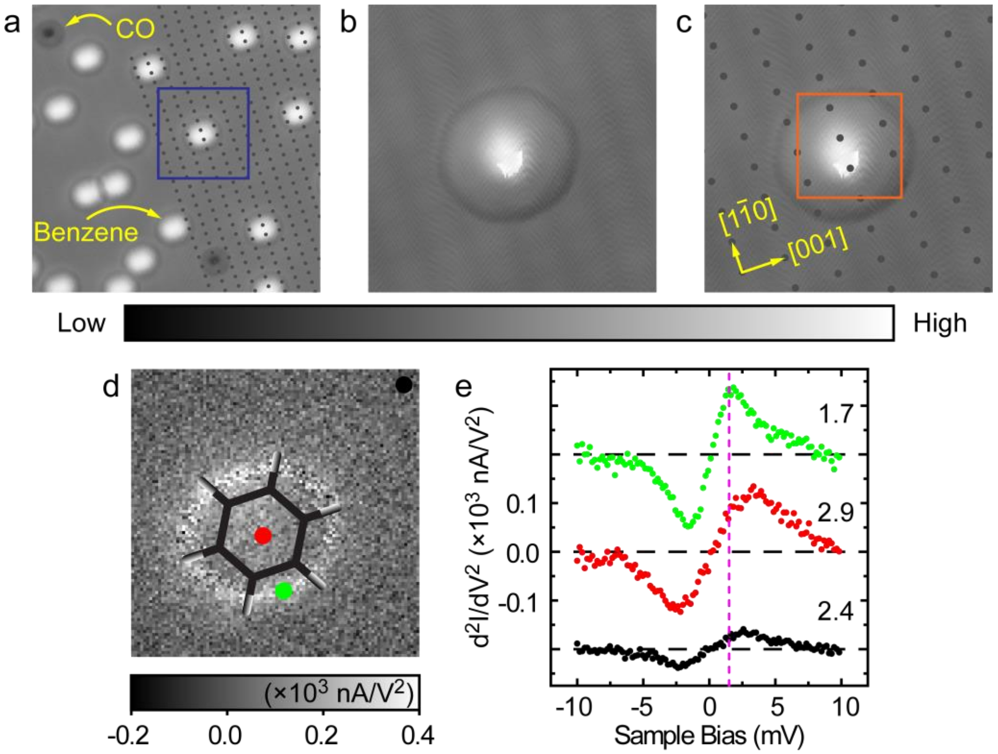
a
CO
Benzene
b
c
[1$\bar{1}$0]
[001]
Low
High
d
(×10^3 nA/V^2)
-0.2
0.0
0.2
0.4
e
d^{2}I/dV^2 (×10^3 nA/V^2)
1.7
2.9
2.4
0.1
0.0
-0.1
-10
-5
0
5
10
Sample Bias (mV)

Figure 4.2. Schematics of the eight high-symmetry configurations of adsorbed benzene on Ag(110), grouped as short bridge site (SB1 and SB2), long bridge site (LB1 and LB2), hollow site (H1 and H2), and top site (T1 and T2). Ag atoms in the subsurface layer (small gray balls), Ag atoms in the surface layer (large gray balls), C atoms (black balls), and H atoms (white balls).

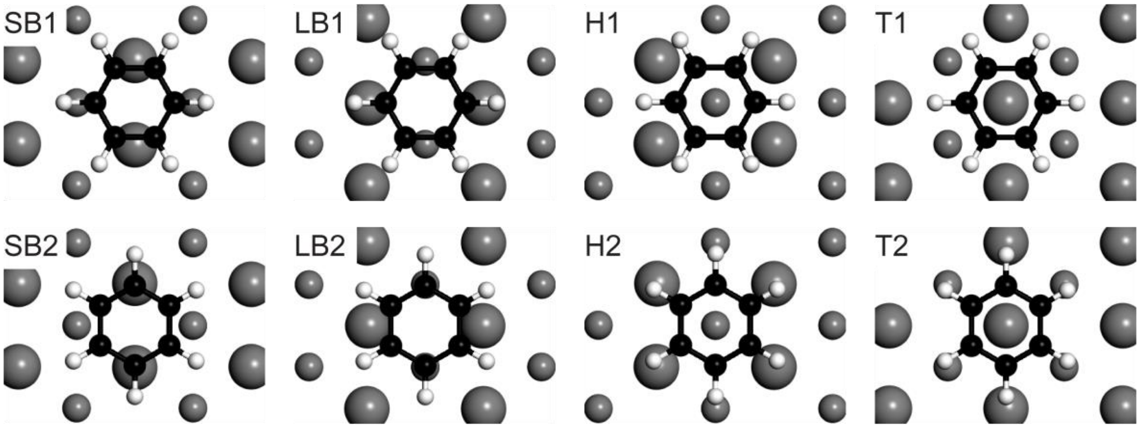
SB1
LB1
H1
T1
SB2
LB2
H2
T2

Figure 4.3. DFT calculations. (a) The projected density of states (PDOS) of π orbitals (red area) and σ orbitals (yellow area) of the adsorbed benzene molecule on Ag(110), and d-states of the Ag surface (green curve), calculated by vdW-optB86b functional. Inset shows the total charge density contour plot 4Å above the plane of benzene and overlaid with its gas phase structure; image size is 8.0 Å×8.0 Å. (b) Top view and (c) side view of the charge density difference $\Delta\rho = \rho_{\text{benzene/Ag(110)}} - \rho_{\text{Ag(110)}} - \rho_{\text{benzene}}$: charge accumulation (pink) and depletion (blue). The value of the isosurfaces of charge density difference is 0.01 e/Å^3.

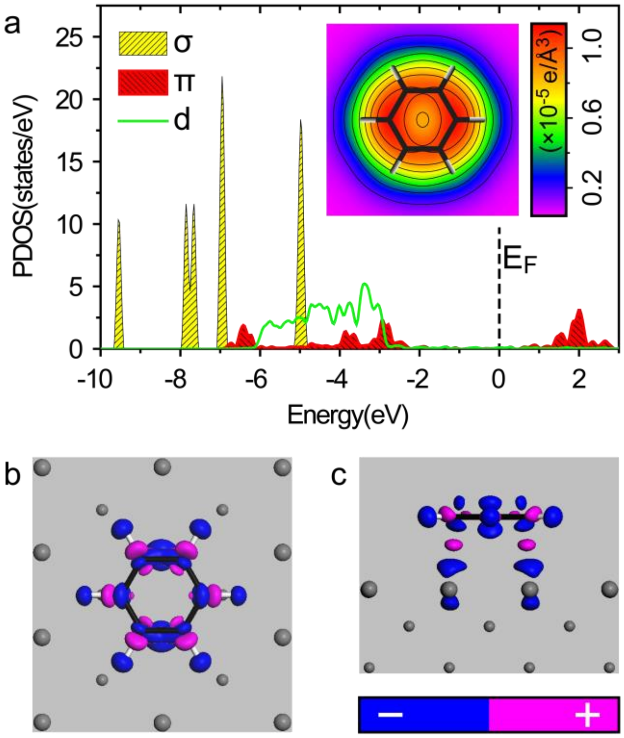

Top View

Side View

Figure 4.4. Analysis of single benzene molecule vibrations on Ag(110). (a) STM-IETS vibrational spectroscopy at 600 mK measured with a bare metal tip: over the molecule (top curve in green), Ag surface (background, middle curve in black), and background-subtracted spectrum (bottom curve in red). Set point: V = 10.0 mV and I = 0.3 nA, and the sample bias was modulated with 1.5 mV_{RMS} at 311.11 Hz for lock-in detection. Taking the average value of the peak and dip energy positions as the vibrational excitation energy: 1.2 mV, 6.9 mV and 12.7 mV, and the corresponding average full width at half maximum (FWHM): 2.0 mV, 3.2 mV and 3.8 mV. (b) Comparison of calculated external vibrational modes from Table 4.3 with STM-IETS measurement for benzene adsorption in the SB1 configuration on Ag(110). The color dots are the calculated results with different functionals, the orange lines are the vibrational energies from STM-IETS measurement, and yellow shaded areas depict the FWHM of the vibrational features. The characteristics of the external normal modes of benzene are described in Figure 4.6.

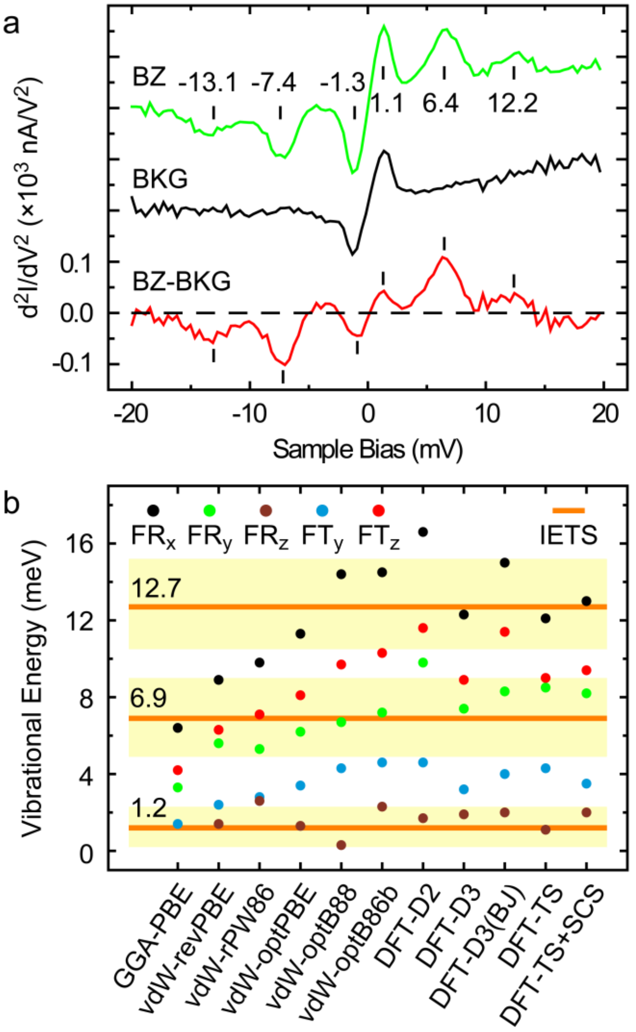
a
BZ
-13.1
-7.4
-1.3
1.1
6.4
12.2
BKG
BZ-BKG
0.1
0.0
-0.1
d^{2}I/dV^2 (×10^3 nA/V^2)
-20
-10
0
10
20
Sample Bias (mV)
b
FR$_x$
FR$_y$
FR$_z$
FT$_y$
FT$_z$
IETS
16
12
8
4
0
12.7
6.9
1.2
Vibrational Energy (meV)
GGA-PBE
vdW-revPBE
vdW-rPW86
vdW-optPBE
vdW-optB88
vdW-optB86b
DFT-D2
DFT-D3
DFT-D3(BJ)
DFT-TS
DFT-TS+SCS

Figure 4.5. The diffusion paths and barriers of benzene on Ag(110) considered in this study and calculated by vdW-optB86b. In panel (a), the short bridge $[1\bar{1}0]$ direction and the long bridge [001] direction on the Ag(110) surface are shown.

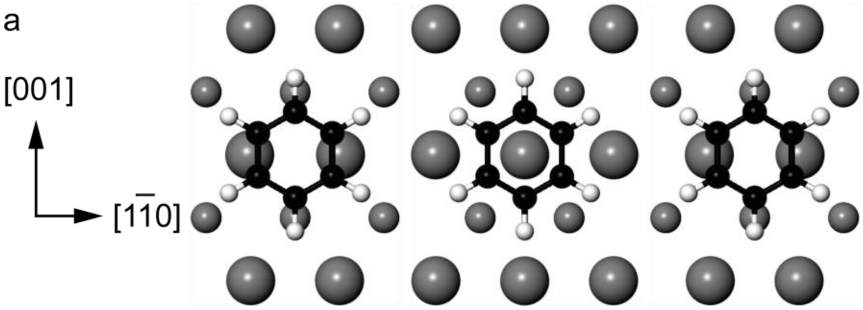

Path1: SB1 → T1 → SB1
Diffusion Barrier: 0.186 eV

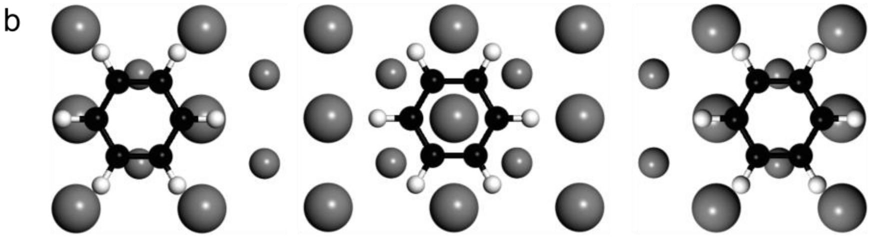

Path2: LB1 → T1 → LB1
Diffusion Barrier: 0.134 eV

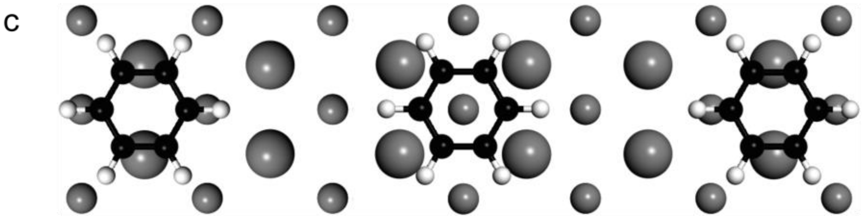

Path3: SB1 → H1 → SB1
Diffusion Barrier: 0.073 eV

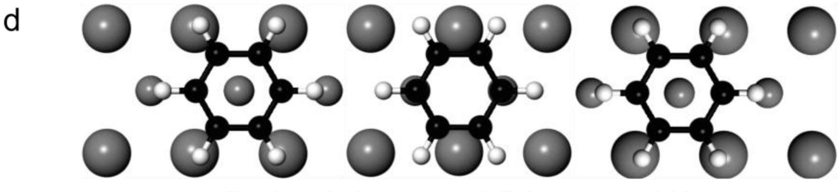

Path4: H2 → LB2 → H2
Diffusion Barrier: 0.033 eV

Figure 4.6. Normal external vibrational modes of SB1 benzene adsorbed on the Ag(110) surface. FR_x, FR_y, and FR_z are the frustrated rotational modes with the rotation axis in the $[001]$ (long bridge), $[1\bar{1}0]$ (short bridge), and $[110]$ direction, respectively. FT_x and FT_y are the frustrated translational modes along long and short bridge direction, respectively. FT_z is the frustrated translational mode normal to substrate plane. The lines capped with arrows represent the normal vectors of external modes of benzene. The subsurface Ag atoms are removed for clarity in the top view of the FR_z mode.

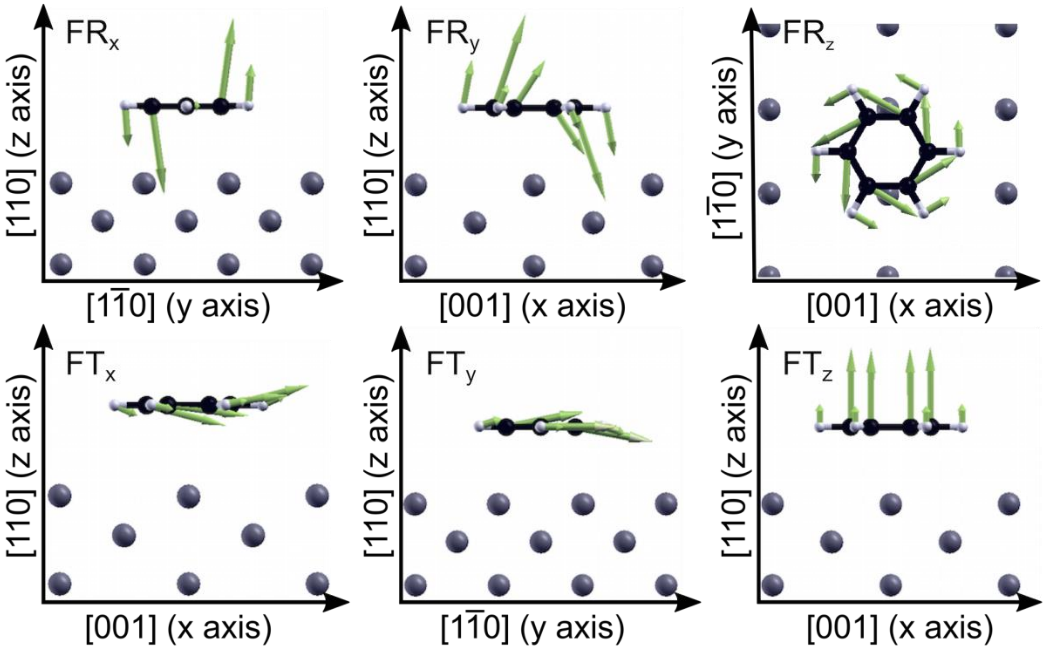
FR$_x$
[110] (z axis)
[1$\bar{1}$0] (y axis)
FR$_y$
[110] (z axis)
[001] (x axis)
FR$_z$
[1$\bar{1}$0] (y axis)
[001] (x axis)
FT$_x$
[110] (z axis)
[001] (x axis)
FT$_y$
[110] (z axis)
[1$\bar{1}$0] (y axis)
FT$_z$
[110] (z axis)
[001] (x axis)

Figure 4.7. Topography and IETS of CO on Ag(110). (a) Constant current STM topography of CO on Ag(110) with a bare silver tip, tunneling set point: I = 1.6 nA, sample bias = 100 mV, size: 20 Å × 20 Å. (b) Atomic resolved constant current topography of the same CO molecule with a CO-terminated tip and overlaid with the grid representing the underneath Ag(110) lattice, set point: I = 0.5 nA, sample bias = 30 mV, size: 20 Å × 20 Å. (c) d^2I/dV^2 spectra of CO on Ag(110) (red solid line) and Ag(110) background (blue dashed line) recorded with a bare silver tip. Set point: I = 1.6 nA, sample bias = 100 mV, bias modulation = 3 mV_{RMS} at 471 Hz. The differential conductance increase for the two inelastic vibrational excitations at ±2.9 mV and ±19.7 mV is about 4% and 6%, respectively. All the measurements in this figure are taken at 600 mK.

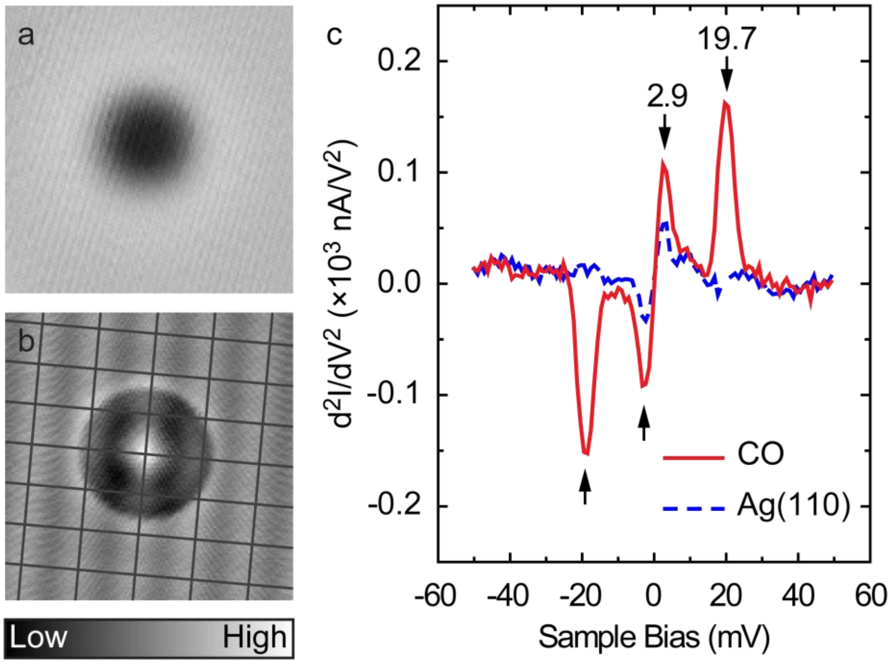
a
b
Low
High
c
19.7
2.9
CO
Ag(110)
0.2
0.1
0.0
-0.1
-0.2
d^{2}I/dV^2 (×10^3 nA/V^2)
-60
-40
-20
0
20
40
60
Sample Bias (mV)

Table 4.1. The adsorption energy (E_{ad}) and the shortest perpendicular distance between carbon and Ag atoms (d_{C-M}) for benzene adsorption on different sites of the Ag(110) surface.

Adsorption Configuration	GGA-PBE		vdW-optB86b	
	E_{ad}(eV)	d_{C-M} (Å)	E_{ad}(eV)	d_{C-M} (Å)
SB1	−0.121	3.06	−0.851	2.61
SB2	−0.126	3.04	−0.848	2.62
LB1	−0.098	3.07	−0.799	2.68
LB2	−0.107	3.06	−0.779	2.67
H1	−0.099	3.08	−0.778	2.67
H2	−0.112	3.07	−0.812	2.62
T1	−0.057	3.29	−0.665	2.83
T2	−0.059	3.30	−0.673	2.84

Table 4.2. The vibrational energies (in meV) were calculated by different DFT methods for the 30 internal modes and 6 external modes of adsorbed benzene in the SB1 geometry. For comparison, the vibrational energies of free gas phase benzene molecule and benzene adsorbed in the SB2 geometry (values in parenthesis) are also shown. Blank entries imply no real vibrational energy was calculated.

Mode	Free benzene	Benzene on Ag(110) surface				
	GGA-PBE	GGA-PBE	vdW-revPBE	vdW-rPW86	vdW-optPBE	vdW-optB88
1	388.1	388.1	386.4	387.6	385.6	385.5
2	386.9	387.1	385.5	386.7	384.8	384.8
3	386.9	387.1	385.4	386.6	384.7	384.7
4	385.0	385.5	383.9	385.2	383.3	383.5
5	385.0	385.4	383.7	385.1	383.2	383.5
6	383.8	384.3	382.7	384.1	382.2	382.6
7	197.0	195.9	194.2	194.0	194.4	195.5
8	197.0	195.4	193.7	193.5	193.8	194.8
9	181.8	181.3	183.0	184.2	182.1	182.5
10	181.8	181.1	182.7	183.9	181.8	182.1
11	166.3	166.1	169.0	171.0	167.6	167.6
12	165.7	165.7	161.3	160.1	163.3	165.1
13	144.5	144.5	146.1	146.7	145.3	145.2
14	144.5	144.2	145.9	146.5	145	144.8
15	141.6	141.8	144.3	145.2	143.4	143.4
16	128.5	128.2	127.8	127.9	127.8	128.4
17	128.5	127.7	127.2	127.2	127.0	127.4
18	123.2	123.1	124.3	125.7	123.8	124.3
19	123.1	122.2	122.4	123.5	121.8	122.8
20	122.4	121.9	120.5	120.4	120.9	121.9
21	118.8	118.3	119.0	119.9	118.2	119.3
22	118.8	118.3	118.8	119.8	118.2	118.8
23	103.8	104.3	105.2	105.9	105.0	105.9
24	103.8	103.4	104.1	104.7	103.6	103.5
25	87.2	86.0	85.5	86.0	85.1	85.7
26	82.4	83.3	84.5	85.0	84.6	85.4
27	74.4	74.0	75.0	75.9	74.5	74.9
28	74.3	73.9	74.7	75.8	74.3	74.8
29	49.0	47.7	48.8	49.3	48.2	48.8
30	49.0	47.6	48.6	49.1	48.0	48.2
FR$_x$		6.4	8.9	9.8	11.3	14.4
FR$_y$		3.3	5.6	5.3	6.2	6.7
FR$_z$			1.4	2.6	1.3	0.3
FT$_x$				1.4		
FT$_y$		1.4	2.4	2.8	3.4	4.3
FT$_z$		4.2	6.3	7.1	8.1	9.7

Table 4.2 (continued)

Mode	Benzene on Ag(110) surface					
	vdW-optB86b	DFT-D2	DFT-D3	DFT-D3(BJ)	DFT-TS	DFT-TS+SCS
1	383.9(384.0)	386.7	387.7(387.3)	387.7	389.1	388.3
2	383.3(383.5)	386.4	386.8(386.7)	386.8	388.5	387.5
3	383.1(382.9)	385.4	386.8(386.1)	386.7	388.2	387.5
4	381.9(382.2)	385.1	385.3(385.3)	385.3	387.2	386.5
5	381.8(381.3)	383.4	385.3(384.4)	385.3	386.9	386.2
6	380.8(380.7)	383.0	384.3(383.7)	384.3	386.0	385.5
7	194.3(194.3)	193.7	195.1(194.9)	194.7	195.3	195.4
8	193.4(193.3)	192.5	194.4(194.1)	194.0	194.6	194.4
9	180.9(180.6)	179.9	181.0(180.7)	180.9	181.3	183.0
10	180.5(180.4)	179.4	180.7(180.4)	180.6	180.9	181.4
11	166.0(165.5)	165.0	165.6(165.6)	165.6	166.2	167.2
12	165.0(165.2)	164.8	165.6(165.2)	165.5	165.8	165.3
13	144.4(144.2)	142.8	144.9(144.6)	144.6	144.1	145.1
14	143.9(143.4)	142.2	144.4(144.0)	144.0	143.6	144.4
15	142.3(141.9)	140.0	142.6(142.3)	142.1	141.5	142.5
16	127.6(127.2)	127.0	128.2(127.8)	128.0	128.1	128.8
17	126.6(126.8)	125.7	127.3(127.3)	127.2	127.2	127.8
18	123.0(123.0)	122.3	123.2(123.1)	123.5	123.2	124.4
19	120.9(121.0)	121.0	121.9(121.8)	122.0	121.8	122.6
20	120.8(120.6)	120.2	121.9(121.5)	121.4	121.2	122.0
21	117.3(117.4)	117.4	118.3(118.2)	117.7	117.8	118.3
22	117.2(116.2)	116.9	118.1(117.4)	117.6	117.3	118.0
23	104.8(104.0)	104.8	105.1(104.5)	104.7	104.3	105.2
24	102.8(102.7)	102.4	103.4(103.4)	103.1	103.3	103.3
25	84.7(84.4)	84.7	85.6(85.5)	85.5	85.3	85.4
26	84.5(84.4)	84.5	84.4(84.3)	84.2	84.4	84.6
27	73.8(73.8)	73.3	74.0(74.0)	74.1	73.8	75.2
28	73.6(73.6)	73.1	73.9(73.8)	74.0	73.7	74.3
29	47.8(48.1)	48.4	48.2(48.5)	48.4	47.9	47.9
30	47.5(47.2)	48.1	47.8(47.7)	47.9	47.5	47.7
FR_x	14.5(15.3)	16.6	12.3(13.8)	15.0	12.1	13.0
FR_y	7.2(6.6)	9.8	7.4(7.4)	8.3	8.5	8.2
FR_z	2.3(2.2)	1.7	1.9(2.0)	2.0	1.1	2.0
FT_x						
FT_y	4.6(4.6)	4.6	3.2(3.2)	4.0	4.3	3.5
FT_z	10.3(10.6)	11.6	8.9(9.6)	11.4	9.0	9.4

Table 4.3. Energies of the 6 external vibrational modes (in meV), adsorption energy (E_{ad}, in eV), and the shortest perpendicular distance separating the carbon and Ag atoms (d_{C-M}, in Å) for benzene adsorbed with SB1 configuration on the Ag(110) surface. Blank entries imply no real vibrational energy was calculated. The characteristics of the external normal modes of benzene are described in Figure 4.6.

DFT Method	FR$_x$	FR$_y$	FR$_z$	FT$_x$	FT$_y$	FT$_z$	E_{ad}	d_{C-M}
GGA-PBE	6.4	3.3		1.4	1.4	4.2	−0.121	3.06
vdW-revPBE	8.9	5.6	1.4		2.4	6.3	−0.523	3.07
vdW-rPW86	9.8	5.3	2.6		2.8	7.1	−0.519	3.04
vdW-optPBE	11.3	6.2	1.3		3.4	8.1	−0.718	2.80
vdW-optB88	14.4	6.7	0.3		4.3	9.7	−0.805	2.69
vdW-optB86b	14.5	7.2	2.3		4.6	10.3	−0.851	2.61
DFT-D2	16.6	9.8	1.7		4.6	11.6	−0.970	2.56
DFT-D3	12.3	7.4	1.9		3.2	8.9	−0.781	2.77
DFT-D3(BJ)	15.0	8.3	2.0		4.0	11.4	−0.861	2.71
DFT-TS	12.1	8.5	1.1		4.3	9.0	−0.840	2.71
DFT-TS+SCS	13.0	8.2	2.0		3.5	9.4	−0.937	2.74

Bibliography

[1] F. Abild-Pedersen, J. Greeley, F. Studt, J. Rossmeisl, T. R. Munter, P. G. Moses, E. Skúlason, T. Bligaard, and J. K. Nørskov, Phys. Rev. Lett. **99**, 016105 (2007).

[2] A. Gerlach, C. Bürker, T. Hosokai, and F. Schreiber, in *Mol. Interface*, edited by N. Koch, N. Ueno, and A. T. S. Wee (Wiley-VCH Verlag GmbH & Co. KGaA, Weinheim, Germany, 2013), pp. 153–172.

[3] J. Krim, Adv. Phys. **61**, 155 (2012).

[4] F. S. Tautz, Prog. Surf. Sci. **82**, 479 (2007).

[5] S. V Aradhya, M. Frei, M. S. Hybertsen, and L. Venkataraman, Nat. Mater. **11**, 872 (2012).

[6] X.-L. Zhou, M. E. Castro, and J. M. White, Surf. Sci. **238**, 215 (1990).

[7] T. J. Rockey, M. Yang, and H.-L. Dai, J. Phys. Chem. B **110**, 19973 (2006).

[8] V. G. Ruiz, W. Liu, E. Zojer, M. Scheffler, and A. Tkatchenko, Phys. Rev. Lett. **108**, 146103 (2012).

[9] W. Liu, V. G. Ruiz, G.-X. Zhang, B. Santra, X. Ren, M. Scheffler, and A. Tkatchenko, New J. Phys. **15**, 053046 (2013).

[10] W. Liu, F. Maaß, M. Willenbockel, C. Bronner, M. Schulze, S. Soubatch, F. S. Tautz, P. Tegeder, and A. Tkatchenko, Phys. Rev. Lett. **115**, 036104 (2015).

[11] R. Duschek, F. Mittendorfer, R. I. R. Blyth, F. P. Netzer, J. Hafner, and M. G. Ramsey, Chem. Phys. Lett. **318**, 43 (2000).

[12] G. Witte, Surf. Sci. **502-503**, 405 (2002).

[13] G. Witte, H. Range, J. P. Toennies, and C. Wöll, Phys. Rev. Lett. **71**, 1063 (1993).

[14] J. I. Pascual, J. J. Jackiw, Z. Song, P. S. Weiss, H. Conrad, and H.-P. Rust, Phys. Rev. Lett. **86**, 1050 (2001).

[15] R. Ryberg, in *Adv. Chem. Phys.*, edited by K. P. Lawley (John Wiley & Sons, Inc., Hoboken, NJ, USA, 1989), pp. 1–44.

[16] B. C. Stipe, M. A. Rezaei, and W. Ho, Science **280**, 1732 (1998).

[17] P. Han, B. A. Mantooth, E. C. H. Sykes, Z. J. Donhauser, and P. S. Weiss, J. Am. Chem. Soc. **126**, 10787 (2004).

[18] H. Gawronski and K. Morgenstern, Phys. Rev. B **89**, 125420 (2014).

[19] C. Chiang, C. Xu, Z. Han, and W. Ho, Science **344**, 885 (2014).

[20] G. Kresse and J. Furthmüller, Phys. Rev. B **54**, 11169 (1996).

[21] G. Kresse and J. Furthmüller, Comput. Mater. Sci. **6**, 15 (1996).

[22] G. Kresse, Phys. Rev. B **59**, 1758 (1999).

[23] H. J. Monkhorst and J. D. Pack, Phys. Rev. B **13**, 5188 (1976).

[24] M. Dion, H. Rydberg, E. Schröder, D. C. Langreth, and B. I. Lundqvist, Phys. Rev. Lett. **92**, 246401 (2004).

[25] J. Klimeš, D. R. Bowler, and A. Michaelides, J. Phys. Condens. Matter **22**, 022201 (2010).

[26] K. Lee, É. D. Murray, L. Kong, B. I. Lundqvist, and D. C. Langreth, Phys. Rev. B **82**, 081101 (2010).

[27] S. Grimme, J. Comput. Chem. **27**, 1787 (2006).

[28] S. Grimme, S. Ehrlich, and L. Goerigk, J. Comput. Chem. **32**, 1456 (2011).

[29] S. Grimme, J. Antony, S. Ehrlich, and H. Krieg, J. Chem. Phys. **132**, 154104 (2010).

[30] A. Tkatchenko and M. Scheffler, Phys. Rev. Lett. **102**, 073005 (2009).

[31] A. Tkatchenko, R. A. DiStasio, R. Car, and M. Scheffler, Phys. Rev. Lett. **108**, 236402 (2012).

[32] T. Bučko, S. Lebègue, J. Hafner, and J. G. Ángyán, Phys. Rev. B **87**, 064110 (2013).

[33] J. Matos, H. Yildirim, and A. Kara, J. Phys. Chem. C **119**, 1886 (2015).

[34] W. Reckien, M. Eggers, and T. Bredow, Beilstein J. Org. Chem. **10**, 1775 (2014).

[35] P. Hapala, R. Temirov, F. S. Tautz, and P. Jelínek, Phys. Rev. Lett. **113**, 226101 (2014).

[36] L. Gross, F. Mohn, N. Moll, B. Schuler, A. Criado, E. Guitián, D. Peña, A. Gourdon, and G. Meyer, Science **337**, 1326 (2012).

[37] N. Moll, B. Schuler, S. Kawai, F. Xu, L. Peng, A. Orita, J. Otera, A. Curioni, M. Neu, J. Repp, G. Meyer, and L. Gross, Nano Lett. **14**, 6127 (2014).

[38] M. P. Boneschanscher, S. K. Hämäläinen, P. Liljeroth, and I. Swart, ACS Nano **8**, 3006 (2014).

[39] Z. Sun, M. P. Boneschanscher, I. Swart, D. Vanmaekelbergh, and P. Liljeroth, Phys. Rev. Lett. **106**, 046104 (2011).

[40] C.-S. Guo, M. A. Van Hove, X. Ren, and Y. Zhao, J. Phys. Chem. C **119**, 1483 (2015).

[41] J. Carrasco, W. Liu, A. Michaelides, and A. Tkatchenko, J. Chem. Phys. **140**, 084704 (2014).

[42] W. Liu, A. Tkatchenko, and M. Scheffler, Acc. Chem. Res. **47**, 3369 (2014).

[43] H. J. Lee and W. Ho, Science **286**, 1719 (1999).

[44] J. R. Hahn and W. Ho, Phys. Rev. Lett. **87**, 196102 (2001).

[45] Note that motions of Ag atoms are excluded in our calulations for the vibrational energies. This should be fine for the FRx and FRy modes due to the large mass of Ag; however, enegies of the FT and FRz modes (1.2 meV) should be viewed cautiously.

[46] J. Klimeš, D. R. Bowler, and A. Michaelides, Phys. Rev. B **83**, 195131 (2011).

[47] G. Henkelman, B. P. Uberuaga, and H. Jónsson, J. Chem. Phys. **113**, 9901 (2000).

[48] G. Henkelman and H. Jónsson, J. Chem. Phys. **113**, 9978 (2000).

[49] H. Ibach and D. L. Mills, *Electron Energy Loss Spectroscopy and Surface Vibrations* (Academic Press, New York, 1982).

[50] C. Morin, D. Simon, and P. Sautet, J. Phys. Chem. B **107**, 2995 (2003).

[51] N. Lorente and H. Ueba, Eur. Phys. J. D **35**, 341 (2005).

[52] J. Oh, H. Lim, R. Arafune, J. Jung, M. Kawai, and Y. Kim, Phys. Rev. Lett. **116**, 056101 (2016).

Chapter 5

Three-dimensional Imaging of a Single Molecule with sub-Ångström Resolution by the Inelastic Tunneling Probe[*]

5.1 Abstract

The interaction between two molecules defines a potential energy surface (PES) in space. This PES contains rich information about the molecules, such as the structure, chemical bonding, reactivity, and diffusion energy barrier. Here we show sub-Ångström resolution imaging of a hexabromobenzene molecule on Ag(110) surface with a CO-functionalized tip through inelastic tunneling probe (itProbe). By tuning the tip-sample distance, we obtain three-dimensional images of the PES landscape between the CO and hexabromobenzene, which display distinct features over different tip heights. A mechanical model is applied successfully to explain the contrast in the images which are directly correlated to the lateral curvature of the PES. The present study also highlights the unique advantages of itProbe as a self-adaptive lateral force microscopy which reveals the subtle lateral corrugation of the PES over a wide range of tip-sample distance.

---

[*] This chapter by Z. Han, G. Czap and W. Ho is prepared for submission to *Physical Review Letters*.

5.2 Article

Recent advancements in scanning probe techniques took a giant leap towards atomic resolution of organic molecules on surfaces by means of non-contact atomic force microscopy (nc-AFM) [1], scanning tunneling hydrogen microcopy (STHM) [2], and inelastic tunneling probe (itProbe) [3] with a molecule-functionalized tip. The atomic contrast originates from the site-dependent variation of detected signals (such as force gradient, tunneling current and molecular vibration) in response to the short-range interaction between the probe molecule and the adsorbates on surfaces. These techniques have been applied to clarify organic molecular structures, intra and intermolecular interactions and chemical reactions at the single molecule level [1–9].

In addition, the three-dimensional (3D) potential energy surface (PES) between the probe molecule and the surface molecule can be constructed by integration of the deconvoluted normal force in nc-AFM experiments [10,11]. The lateral force or lateral variation of the PES can be obtained from the numerical derivative of the 3D PES [10], but this approach suffers from considerable noise [12]. Alternatively, lateral force microscopy (LFM) has been applied to directly sense the chemical forces parallel to the surface. It reveals finer lateral corrugation of the PES which is challenging for indirect normal force AFM measurement [12]. However, this type of LFM only measures the lateral force along the tip oscillation direction, which typically cannot be tuned during the imaging along the surface plane. Therefore if the tip oscillation is not aligned with the symmetry axis of the surface objects, significant distortion would be expected before any correction or post-processing.

In this letter, we study a single hexabromobenzene (C_6Br_6) molecule on Ag(110) surface using the itProbe technique [3] as a function of tip-sample distance to visualize the lateral corrugation in the PES between the molecule and a CO-decorated tip in 3D space. We introduce itProbe as a "self-adaptive LFM" which adjusts its oscillation direction according to the potential energy profile and directly senses the local lateral curvature of the PES. A mechanical model based on the one developed by Hapala *et al.* [13,14] is applied to interpret the contrast mechanism of constant height itProbe and conductance images over a large range of tip-sample separation. The simulations indicate that the electrostatic interaction between the molecules is critical to model the CO relaxations on the tip correctly. We also find that it is necessary to scale the itProbe intensity with the conductance map to correctly reproduce the experimental results.

The experiment was conducted in a home-built sub-Kelvin scanning tunneling microscope (STM) under ultrahigh vacuum with base pressure of 5×10^{-11} Torr. The design of microscope scanner was adopted from Ref. [15]. The Ag(110) crystal and the electrochemically etched silver tip were prepared by repeated Ne^+ sputtering-annealing cycles. C_6Br_6 molecules were thermally evaporated from a Knudsen cell onto the surface held at 25 K, followed by CO dosing. Both the sample and scanner were subsequently cooled to 600 mK for all the STM measurements.

Fig. 5.1(a) and 1(b) show the constant current STM topographic images of an isolated C_6Br_6 molecule scanned with a bare metal tip and CO-tip at the same tunneling set point. The image resolution is enhanced with CO-tip such that the hexagonal outline of the molecule is more well-defined as shown in Fig. 5.1(b). Additionally the center of the molecule is imaged as a small depression [Fig. 5.1(b) and Fig. 5.3(a)] in contrast with a protrusion [Fig. 5.1(a)] with the metallic tip. The molecule orientation and structure can be reassembled from the closer tunneling set point scan shown in Fig. 5.1(c). The molecule appears as a donut with a bigger depression in the center and a bright band around it. The six dark lines across the bright band indicate the location of C-Br bonds. In nc-AFM measurements [1,5,6] a dark halo surrounding a molecule induced by the electrostatic and van der Waals interactions is commonly found. Here a sharp border is observed along the periphery of the molecule as indicated with a blue arrow. This is associated with the boundary that the CO on the tip starts to bend in response to the attractive interaction with the C_6Br_6 and majority of the electrons tunnel to the C_6Br_6 instead of directly to the substrate. With the itProbe technique [3], we resolve the six-member ring and six C-Br bonds clearly in both d^2I/dV^2 channel [Fig. 5.1(d)] and dI/dV channel [Fig. 5.1(e)], which are consistent with Fig. 5.1(c). In addition to the covalent bonding structure, a bright circle around the molecule is also highlighted in Fig. 5.1(d). Combined with the topographic image with atomically resolved Ag(110) lattice in Fig. 5.1(d), the isolated C_6Br_6 adsorbs on short bridge site of Ag(110) and two C-Br bonds are aligned with $[1\bar{1}0]$ direction as illustrated in Fig. 5.1(g).

The origin of the itProbe image contrast is manifested in the spatially resolved STM inelastic tunneling spectroscopy (IETS) [16] with the CO-tip over different sites of the C_6Br_6 molecule in Fig. 5.2. CO hindered translation (HT) can be modeled as a harmonic oscillator and its energy is determined by the curvature of the vibrational potential well [14]. The variation of potential energy between the CO-tip and C_6Br_6 modifies the curvature and leads to the different HT energies of the CO-tip over space. At the repulsive ridges and apexes of the PES, the local curvature is negative therefore the overall curvature for the CO vibrational well is reduced. As a result, CO vibrational energies red shift over site 1, 3, 4, 5 and 6 in Fig. 5.2. In contrast, the attractive valleys of the PES are associated with positive local curvatures and CO-vibrational energies blue shift, such as at sites 0 and 2. Hence mapping the d^2I/dV^2 signal at a reduced energy such as 1.5 mV highlights the locations associated with negative curvatures in the PES. Within a certain z range, the itProbe images resemble the molecular structure.

To investigate the evolution of itProbe images with different tip-sample separations in order to probe the lateral corrugation of the PES in three-dimensional space, we obtained a series of constant height itProbe images by tuning the tip-sample separation as shown in Fig. 5.3. When the tip is far away from the surface, only six bright dots are visible in Fig. 5.3(c) and (d). As the tip-sample distance is reduced, covalent molecular bonding structure, including a hexagonal carbon ring and six C-Br bonds, starts to appear in the imaging [Fig. 5.3(e-g)]. Strikingly, there is a bright ring surrounding the molecule where no covalent bonds are present. The imaged hexagon is bigger than the physical size as indicated in the model in Fig. 5.3(b). When the tip-sample distance is further reduced, the hexagon becomes increasingly larger. In addition, the image contrast inverts from depression to protrusion at the center of the hexagon in Fig. 5.3(o) and (p). Similar contrast inversion has also been observed with nc-AFM [4,17]. Eventually the central feature converts to a ring as shown in Fig. 5.3(q-r) which has not been reported previously. The constant height dI/dV images are also shown in Fig. 5.3 to assist with the analysis. Compared with dI/dV, d^2I/dV^2 shows higher spatial resolution and reveals more subtle structures. The intensity of d^2I/dV^2 at the chosen imaging bias (1.5 mV) has the largest spatial contrast [3] while dI/dV can be considered as the integration of d^2I/dV^2

from the Fermi level to the imaging bias which contains other less spatially varying components that degrade the overall contrast.

The mechanical model developed by Hapala *et al*. [14] is employed to investigate the z-dependent contrast in the itProbe images. Instead of using a lateral spring [14] to model the tip-CO in their previous paper, a more appropriate torsional spring model [12] is used here to account for the larger CO tilting angle at small tip-sample separations. Previous studies indicate that the electrostatic forces are essential to understand the contrast in itProbe/nc-AFM images of polar molecules, although the sensitivity of CO to electrostatic forces is now in question [14,18,19]. Without electrostatic interactions with the CO, a C_6Br_6 molecule can be considered as a superposition of two concentric hexagons, one for carbon and the other for bromine. The simulated images without electrostatic interactions in Fig. 5.5(e) show the covalent bonding structure of C_6Br_6 when tip is relatively far away ($Z_{CO} \geq 3.15$ Å). At smaller tip heights, another hexagon connecting the bromine atoms appears when $Z_{CO} = 3.0$ Å and a bright dot emerges at the center. However, the size of the C-hexagon doesn't show significant variation over different tip heights.

We fit the charge value on the oxygen atom and use either the Hartree potential from density function theory calculation [20] or the potential created by point charge model to account for the electrostatic contribution [14]. Both models successfully reproduce the bright circular feature around the molecule in Fig. 5.4(a) and Fig. 5.5. In the experiment, both the d^2I/dV^2 and dI/dV images at $\Delta Z \geq 1.32$ Å exhibit a clear boundary [Fig. 5.3(e-g) and (j-x)]. This is consistent with the abrupt CO tilting angle changes as shown in the simulation [Fig. 5.4(d) and Fig. 5.7(a-b)]. The bright boundary indicates the repulsive interaction presented to the CO molecule and associated negative curvature of the PES, thus CO tilts away from the boundary and the CO vibrational energy is also reduced. As shown in Fig. 5.5, the repulsive interaction between the negatively charged CO and Br is enhanced when the negative charge on CO increases and the bright circle becomes more prominent. In addition, the model also correctly captures the center hexagon expansion when tip-sample distance is reduced. This is possibly induced by the attraction between the positively charged carbon ring and the negatively charged CO molecule that increase the CO bending towards the center of C_6Br_6. Furthermore, a center ring feature and bifurcation at the bromine atom are also reproduced in Fig. 5.5(a) and (c) when $Z_{CO} \leq 2.6$ Å as observed in Fig. 5.3(q-r).

Detailed analysis of the CO vibrational eigenvector and relaxation from the mechanical model explore the interplay between them. The CO molecule relaxes along the steepest PES gradient (principle axis) and its HT eigenvector rotates and eigenenergy shifts. As shown in Fig. 5.4(e) and Fig. 5.7(c), the eigenvector associated with higher vibrational energy is always along the CO bending direction, and the lower energy eigenvector is perpendicular to the bending direction. Thus the CO HT energies directly reflect the local curvatures of the PES along the principal axes. Similar to LFM [12], the CO hindered translation is only affected by the local lateral intermolecular interactions and not sensitive to the long-range van der Waals interaction between the tip and silver substrate. Therefore the itProbe technique acts as a LFM that self-orients to the local landscape of the PES and rotates its oscillation direction to reveal its lateral curvature along the principal axis.

Despite the success that the simple torsional spring model has in capturing some of the major features discussed above, at close tip-sample distance the contrast outside the molecule is exaggerated. In the previous work [14], the IETS peak amplitude is weighed equally at each pixel and the intensity of itProbe is solely determined by the shift of CO vibrational energy from the imaging bias. However, the d^2I/dV^2 intensity is also proportional to the conductance of the tunneling junction. Therefore the original simulation [raw itProbe image in Fig. 5.4(a)] overestimates the intensity where the tunneling conductance is suppressed, especially for the locations where CO has sudden relaxation towards the center of C_6Br_6. We therefore chose to simulate the *dI/dV* images [Fig. 5.4(b) and Fig. 5.6(a-b)] to compare with experiment and scaled the raw itProbe images by the STM image as shown in Fig. 5.4(c). Excellent agreement between calculation and experiment has been achieved for both the *dI/dV* and d^2I/dV^2 images at all tip heights. The *dI/dV* images are selected from the angular independent (s-wave) and dependent (p-wave) model [13] simulations shown in Fig. 5.6(a) and (b). In the s-wave model, the simulated images display a depression in the molecular center and six bright lobes over C-Br bonds when the tip is far away ($Z_{CO} \geq 3.3$ Å). As the tip-sample distance is shortened ($Z_{CO} = 3.15$ and 3.0 Å), the hexagonal carbon ring becomes a protrusion which is a typical feature in STHM [2,7,8] and matches Fig. 5.3(s-t). Furthermore, the C-Br bonds are shown as depressions and the connections between the adjacent Br atoms are shown as protrusions. This image contrast inversion is comparable to those observed in atom manipulation or scanning point contact microscopy measurements [21–23]. The CO relaxes away from the Br atoms [Fig. 5.7(b)] so that the conductance is reduced the over C-Br bonds and enhanced between the Br atoms because more tunneling sites are present. For closer tip-sample distance ($Z_{CO} \leq 2.6$ Å) the p-wave model gives better agreement in that the molecular center is shown as a bright circle while s-wave model generates much bigger signal outside the molecule to compared with experiments [Fig. 5.3(g-k) and Fig. 5.6(b)]. Overall, at big tip-sample separations the CO-tip behaves as an s-wave tip while p-wave tunneling has to be considered for small separations as the CO tilting angle increases. These results are consistent with the picture that a CO tip exhibits both s-wave and p-wave tunneling behavior [24], which may have a hitherto unexplored height dependence. Further improvement can be implemented by considering the IETS cross section variation of the different tunneling sites and vibration eigenvector directions.

In summary, we have demonstrated that the itProbe technique can be used as a "self-adaptive" lateral force microscopy to visualize the lateral corrugation of the PES between the surface objects and probe particle in 3D space. The images yield feature-rich contrast which can serve as a calibration standard for the selection of proper model and more reliable fitting parameters. A torsional spring tip-CO model was applied to illustrate the contrast mechanism in simultaneous d^2I/dV^2 and dI/dV images over a wide tip-sample separation and excellent agreement is reached with experimental observations. Inclusion of the electrostatic interaction is shown to have a significant impact on the simulation accuracy. Scaling the IETS intensity by the conductance greatly improves the agreement with experiment and provides an opportunity for the model to reach quantitative agreement even at close tip-sample distance. Furthermore, the dI/dV simulation suggests a transition of the tunneling behavior for the CO-to-molecule junction from s-wave like to p-wave like as the CO-tip approaches the molecule.

5.3 Supplementary Materials

The model uses the same physical description of the tip as Hapala *et al.* [13,14], except that the lateral spring has been replaced by a torsional spring [12] with force given by $kR\theta$, where k is the spring constant, R is the distance between oxygen atom to the metal tip and θ is the bending angle of CO with respect to the tip axis (surface normal). The tip stiffness or spring constant is set by

$$\hbar\omega = \hbar\sqrt{k/m_O} = 2.4\ \text{meV}, \tag{5.1}$$

where m_O is the mass of oxygen atom and $\hbar\omega$ is CO hindered translational vibration energy on the silver tip directly measured from STM-IETS with the CO-tip positioned over the bare substrate.

The interaction between the CO-tip and hexabromobenzene molecule is describe by a pairwise Lennard-Jones (LJ) potential and electrostatic interaction.

As with Hapala's model, the particular form of the LJ potential used here is

$$V = \sum_{i=Atoms\ in\ C_6Br_6} E_{Oi}\left[\left(\frac{R_{eq}}{r_{Oi}}\right)^{12} - 2\left(\frac{R_{eq}}{r_{Oi}}\right)^{6}\right], \tag{5.2}$$

where r_{Oi} is the distance between oxygen atom on the CO to the i^{th} atom in the C_6Br_6 molecule, the heteroatom coefficients are computed using $E_{Oi} = \sqrt{E_O E_i}$ and $R_{eq} = R_O + R_i$. The coordinates of carbon and bromine atoms are directly from DFT calculation of the relaxed C_6Br_6 molecule on the short bridge site of Ag(110) surface [20]. The vdW parameters for different elements are listed below.

Oxygen in CO: $E_O = 9.106$ meV, $R_O = 1.661$ Å as Hapala uses in his model [14]. A 4 eV artificial LJ term glues the oxygen atom to a spherical surface around the metal tip atom, with this radius = 3.14 Å measured from oxygen to terminated Ag atom on the tip from DFT calculation.

We use the OPLS vdW parameters of C and Br in bromobenzene [25].

Carbon in C_6Br_6: $E_C = 3.035$ meV and $R_C = 1.99237$ Å;

Bromine in C_6Br_6: $E_{Br} = 20.38$ meV and $R_{Br} = 1.94747$ Å .

The Hartree potential is calculated from the DFT simulation of a relaxed C_6Br_6 molecule on the short bridge site of Ag(110) surface without CO-tip, where the Hartree LOCPOT is used without exchange correlation and without van der Waals correction [20]. The grid of points in the Hartree potential is cropped to a three-dimensional (3D) box that is slightly bigger than the total 3D space probed by the simulation (which is 12 Å × 12 Å × 1.3 Å). A Gaussian charge density with full width at half maximum (FWHM) of 1Å is used to simulate the charge density distribution of the oxygen atom. A charge value of -0.2 e was found to have good agreement with experiment using this Gaussian width.

Alternatively, electrostatic interaction can be modeled as pairwise point-charge interaction between individual atoms in C_6Br_6 and CO molecule. The point charge values on the individual atoms in the C_6Br_6 molecule are +0.2 e for carbon and -0.2 e for bromine [25]. We note that the simulated results shown in Fig. 5.5(a) are in good agreement with experiment as well. The point-charge value of CO is taken as a fitting parameter. The best fitted value is -0.04 e for the point-charge model.

The effective charge on CO is one of the most important fitting parameters in Hapala's mechanical model for incorporating the electrostatic interaction between the probe molecule and the surface molecule. However the reported charge values for CO show large variations among different studies, from -0.4e [14] to -0.05e [18] and 0e [19,26]. In our itProbe measurements, the images exhibit a wealth of distinct features which evolve as a function of tip height. Instead of comparing the simulated itProbe images with experiment at only one tip height [14], here we compare all tip height images to get the best charge value for more reliable fitting. We also explicitly calculate the LJ potential/force at each pixel rather than interpolating between pre-computed grid points in order to avoid missing subtle contrast features that arise from sharp changes in the PES.

As mentioned in Ref. [14], the relaxation of CO is crucial to get the real vibrational energy for CO molecules at all sites. Here the O atom of the CO is relaxed using the FIRE algorithm as used previously [13,14]. The O is relaxed until there is a net force lower than 10^{-7} eV/A. There is no relaxation of the C_6Br_6 atoms and Ag atoms are not included in the mechanical model.

itProbe images are simulated by taking the computed vibrational eigenvalues and using only the two smaller eigenvalues (the biggest eigenvalue corresponds to a tip-CO bouncing mode which we exclude as nonphysical due to the artificial LJ force used to bind the CO to the tip). The two d^2I/dV^2 peaks are then simulated as Gaussians with FWHM = 1.7 meV at the eigenvalue positions, which implicitly assumes the STM-IETS peak broadening is dominated by the 1 mV_{RMS} sample bias modulation for the imaging at 600 mK. At each pixel, the itProbe signal strength is obtained by sampling both eigenvalue Gaussians at the imaging bias (1.5 meV). The zero bias anomaly [3,27] and the positive/negative bias interference of the low bias peaks are not included.

For the constant height STM image simulation, we adapt the mechanical model [13] to calculate the conductance, both angular independent and dependent models. At low sample bias, such as 1.5 mV in our experiment, the current (*I*) image and conductance (*dI/dV*) image are almost identical except that *dI/dV* images are much less noisy since they are filtered through lock-in amplifier, so we show the *dI/dV* in Fig. 5.3 instead of *I*. The model assumes the conductance is the sum of all tunneling channel contributions from the probe particle to the each atom on the surface molecule, with Ag(110) surface atoms neglected, such that

$$dI/dV(\vec{R}) \propto T_{Ag\ to\ CO}\left(\vec{R},\overrightarrow{r_O}\right) \sum_{i=Atoms\ in\ C_6Br_6} T_{CO\ to\ i}(\overrightarrow{r_O},\overrightarrow{r_\iota}), \qquad (5.3)$$

where $T_{Ag\ to\ CO}$ and $T_{CO\ to\ i}$ are the tunneling probability from terminated Ag atom to the CO molecule on the tip and from the CO molecule to the i^{th} atom in the C_6Br_6 molecule. To account the difference in local density of states over carbon and bromine atom at the same tip height, we introduce a fitting parameter h to compensate the difference of effective radius for carbon and bromine atoms. The tunneling probability from CO to atom in the C_6Br_6 molecule is then given by

$$T(\overrightarrow{r_1},\overrightarrow{r_2}) \propto e^{-2\beta(|\overrightarrow{r_1}-\overrightarrow{r_2}|-h)}. \qquad (5.4)$$

We assume the β is the same for both for tip to CO and CO to C_6Br_6. The h is fitted to be 0.6 Å and β is fitted to be 1.25 $Å^{-1}$ to get the best agreement with experimental result.

One of the main qualitative conclusions from this is that multiplication of a simulated itProbe image with the corresponding STM model image gives much better agreement primarily because the IETS signal needs to be damped outside the molecule as seen in experiment.

Figure 5.1. STM images of an isolated C_6Br_6 molecule on Ag(110). Constant current STM topographies obtained with a bare metal tip for (a) and CO-tip for (b), (c) and (f). The tunneling set points are 0.1 nA/ 0.1V for (a) and (b), 0.1 nA/10 mV for (c) and 0.5 nA/10 mV for (f). The surface silver atoms are resolved in (f) to determine the adsorption site of C_6Br_6 molecule. (d) and (e) are d^2I/dV^2 and dI/dV itProbe images acquired simultaneously at 1.5 mV. The tunneling feedback loop is turned off over the center of the molecule at 0.1 nA and 0.1 V which is denoted as Z_0 throughout the paper. The sample bias is ramped to 1.5 mV and then the tip is advanced towards the surface by 1.46 Å and kept the same height for the imaging process. The sample bias is modulated with 1 mV_{RMS} sine wave at 311.11 Hz. 96 pixels × 96 pixels. (g) Schematic diagram of the C_6Br_6 adsorption on Ag(110) surface. The image sizes are 20 Å × 20 Å for (a-c), 12 Å × 12 Å for (d-e) and 36 Å × 32 Å for (f).

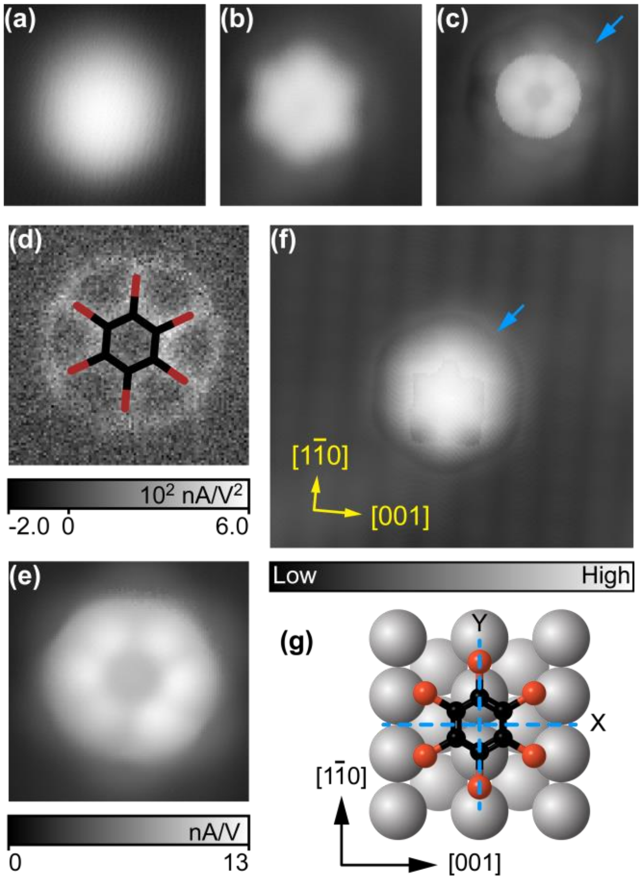
(a)
(b)
(c)
(d)
10^2 nA/V^2
-2.0
0
6.0
(f)
[1$\bar{1}$0]
[001]
Low
High
(e)
nA/V
0
13
(g)
Y
X
[1$\bar{1}$0]
[001]

Figure 5.2. Spatially resolved CO-tip d^2I/dV^2 vibrational spectra. The spectra are taken with the same tip-sample height as the inset. Feedback is disabled at Z_0 and the tunneling gap is reduced by 1.46 Å. Subsequently, the tip is sent to the locations labeled by 0 through 7 in the inset [Fig. 5.1(e)] to take spectra. Sample bias modulation is set at 311.11 Hz and 1 mV_{RMS}.

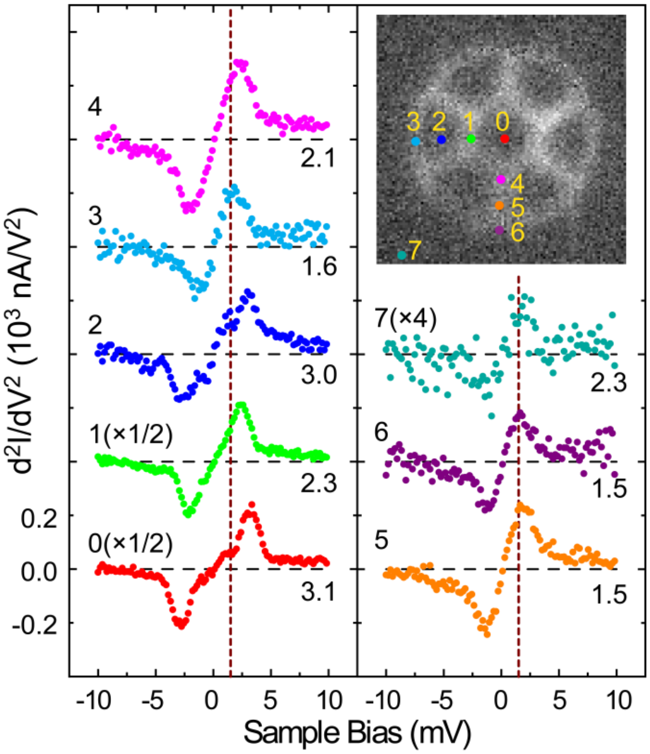
d²I/dV² (10³ nA/V²)
0.2
0.0
-0.2
4
2.1
3
1.6
2
3.0
1(×1/2)
2.3
0(×1/2)
3.1
3 2 1 0
4
5
6
7
7(×4)
2.3
6
1.5
5
1.5
-10 -5 0 5 10
-10 -5 0 5 10
Sample Bias (mV)

Figure 5.3. Tip height dependent itProbe images of isolated C_6Br_6 molecule. (a) The schematic diagram of the experimental setup. During the itProbe measurement, the tunneling feedback is disabled at Z_0. Then the tunneling gap is reduced by ΔZ as indicated on the upper right corner of each image and the tip is held at that height for imaging. The 3D topography shown in (a) is the same as Fig. 5.1(b). (b) Scaled stick model of C_6Br_6 molecule to compare its size with measurement. Simultaneously measured d^2I/dV^2 [(c-g) and (m-r)] and dI/dV [(h-l) and (s-x)] itProbe images at 1.5 mV as a function of tip-sample distance. The images are 12 Å × 12 Å and 64 pixels × 64 pixels for (c-x).

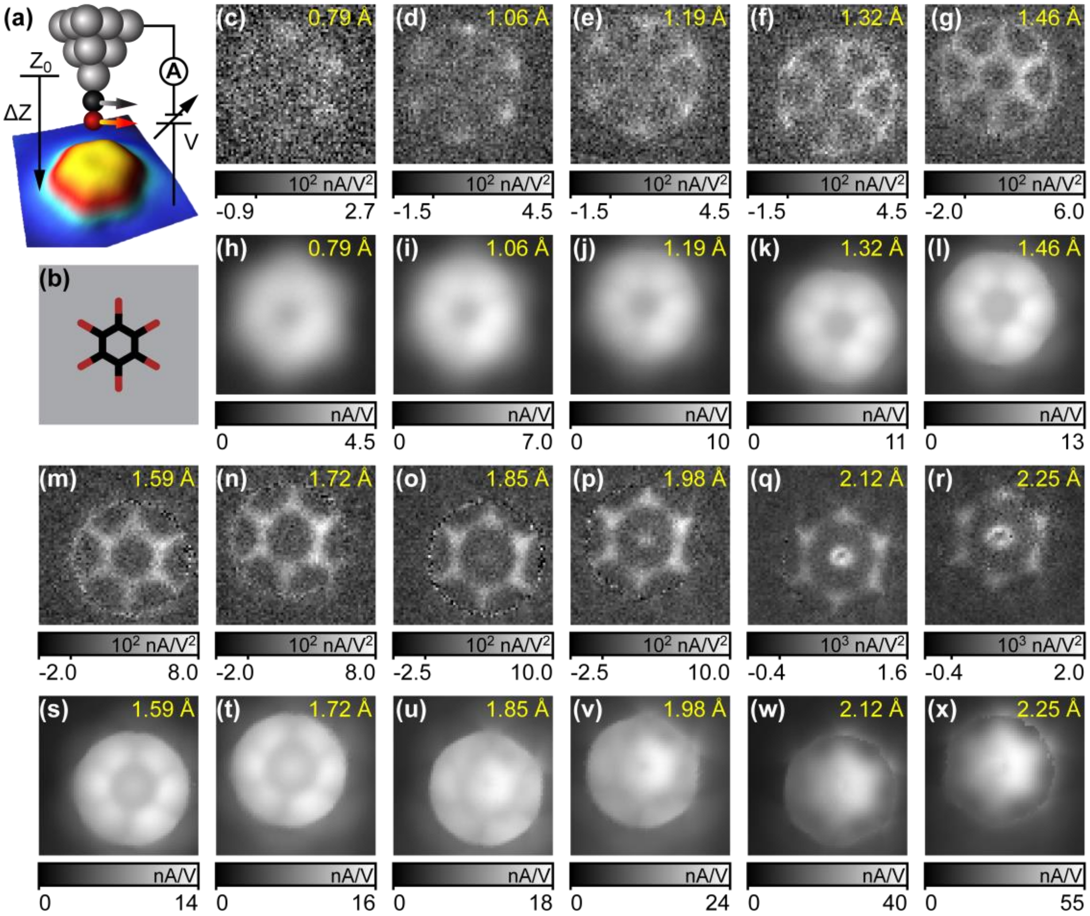
(a)
Z_0
ΔZ
A
V
(b)
(c) 0.79 Å
(d) 1.06 Å
(e) 1.19 Å
(f) 1.32 Å
(g) 1.46 Å
10² nA/V²
-0.9 2.7
-1.5 4.5
-1.5 4.5
-1.5 4.5
-2.0 6.0
(h) 0.79 Å
(i) 1.06 Å
(j) 1.19 Å
(k) 1.32 Å
(l) 1.46 Å
nA/V
0 4.5
0 7.0
0 10
0 11
0 13
(m) 1.59 Å
(n) 1.72 Å
(o) 1.85 Å
(p) 1.98 Å
(q) 2.12 Å
(r) 2.25 Å
10² nA/V²
-2.0 8.0
-2.0 8.0
-2.5 10.0
-2.5 10.0
10³ nA/V²
-0.4 1.6
-0.4 2.0
(s) 1.59 Å
(t) 1.72 Å
(u) 1.85 Å
(v) 1.98 Å
(w) 2.12 Å
(x) 2.25 Å
nA/V
0 14
0 16
0 18
0 24
0 40
0 55

Figure 5.4. Constant height simulation results using the Hartree potential model. (a) Raw itProbe images without scaling. (b) STM conductance images. (c) itProbe images scaled with calculated STM conductance. Here Z_{CO} is defined as the vertical displacement of the oxygen atom of the CO to C_6Br_6 molecular plane. (d) Projection of the oxygen atom relaxation displacement in the XY plane at Z_{CO} = 3.15 Å. (d) Projection of CO HT eigenvectors in the XY plane at Z_{CO} = 3.15 Å. A scaled C_6Br_6 model is superimposed with (d) and (e). Red (blue) segments correspond to the lower (higher) eigenvalues.

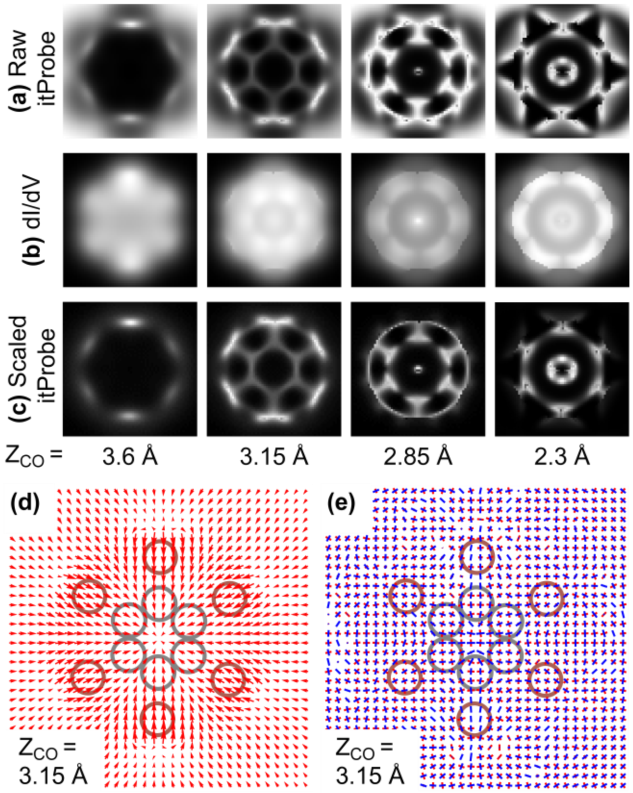
(a) Raw itProbe
(b) dI/dV
(c) Scaled itProbe
Z_{CO} =
3.6 Å
3.15 Å
2.85 Å
2.3 Å
(d)
Z_{CO} =
3.15 Å
(e)
Z_{CO} =
3.15 Å

Figure 5.5. Simulated d^2I/dV^2 itProbe images as a function of tip-sample distance with different model parameters. (a) Point charge model result with charge = -0.04 e on the CO-tip. (b-f) Hartree potential model results with different charges on the CO. In the case of charge = 0 e in (e), electrostatic interaction is not included in the model, pairwise LJ potential is the only interaction considered. Z_{CO} is defined as the distance from oxygen atom in the CO to the C_6Br_6 molecular plane.

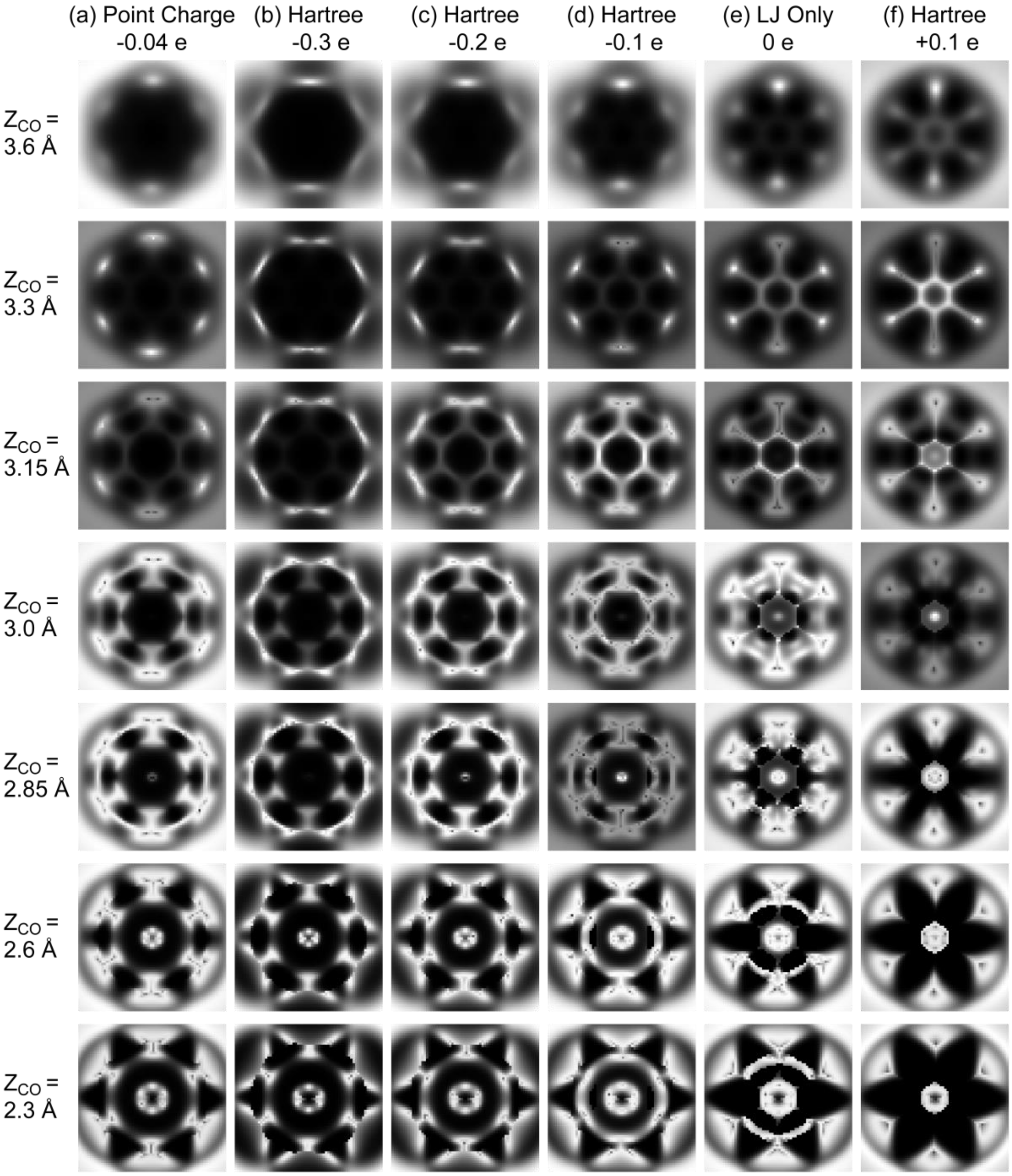
(a) Point Charge
-0.04 e
(b) Hartree
-0.3 e
(c) Hartree
-0.2 e
(d) Hartree
-0.1 e
(e) LJ Only
0 e
(f) Hartree
+0.1 e
Z_{CO} =
3.6 Å
Z_{CO} =
3.3 Å
Z_{CO} =
3.15 Å
Z_{CO} =
3.0 Å
Z_{CO} =
2.85 Å
Z_{CO} =
2.6 Å
Z_{CO} =
2.3 Å

Figure 5.6. Simulated d^2I/dV^2 and dI/dV itProbe images as a function of tip-sample distance. (a) Constant height dI/dV simulation with the angular independent s-wave tunneling model. (b) dI/dV simulation with the angular dependent p-wave model. (c) Raw d^2I/dV^2 itProbe image without scaling with conductance. (d) and (e) are the d^2I/dV^2 itProbe images scaled with calculated conductance with s-wave and p-wave model respectively. (f) Selected d^2I/dV^2 itProbe images from (d) and (e) which are boxed. A scaled C_6Br_6 molecule model is superimposed on top of each calculated images for comparison.

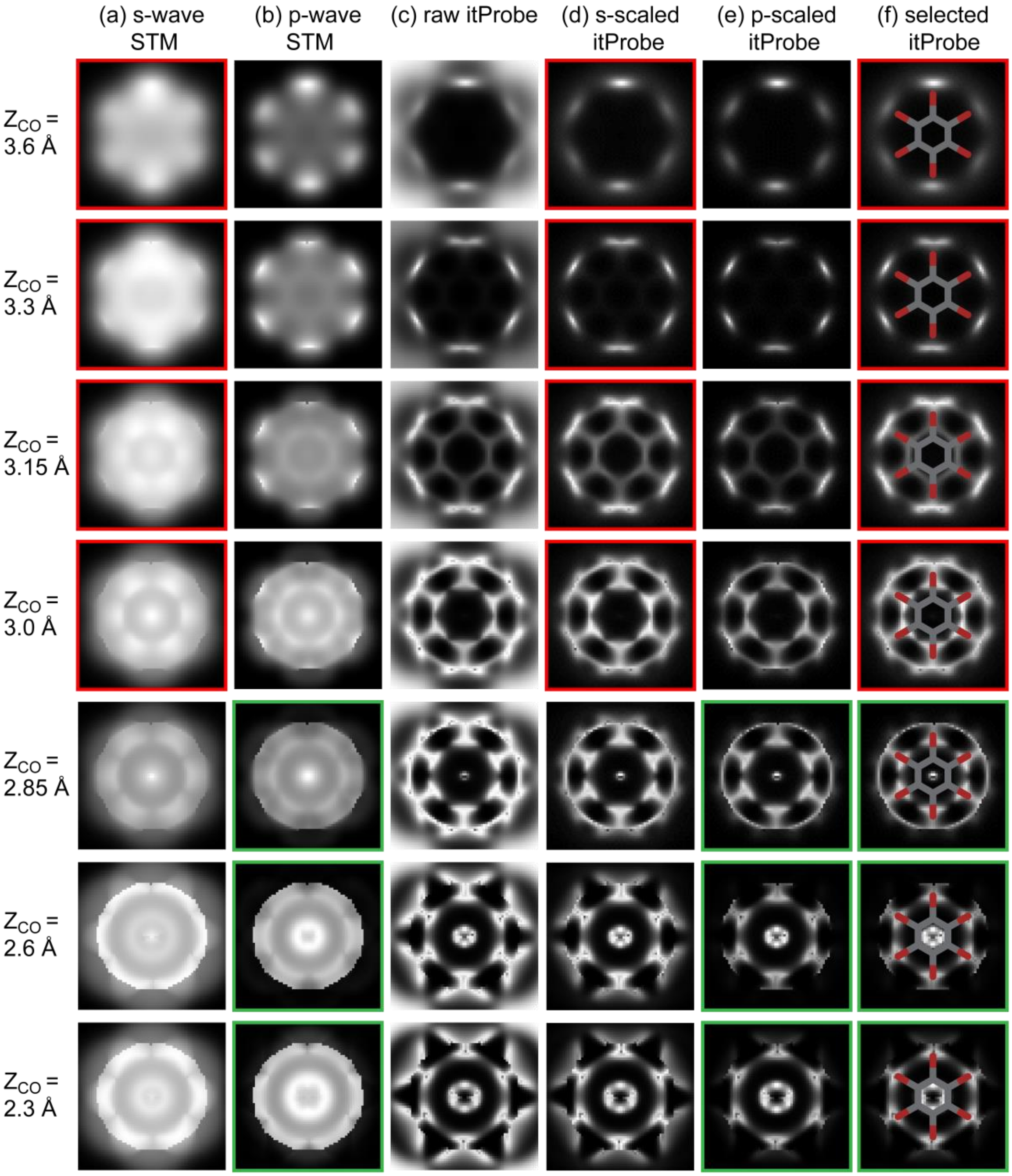
(a) s-wave STM
(b) p-wave STM
(c) raw itProbe
(d) s-scaled itProbe
(e) p-scaled itProbe
(f) selected itProbe
Z_{CO} = 3.6 Å
Z_{CO} = 3.3 Å
Z_{CO} = 3.15 Å
Z_{CO} = 3.0 Å
Z_{CO} = 2.85 Å
Z_{CO} = 2.6 Å
Z_{CO} = 2.3 Å

Figure 5.7. The interplay between CO tilting and hindered translational vibration as a function of tip-sample distance. (a) CO tilting angle. (b) Oxygen atom relaxation displacement vectors projected onto the C_6Br_6 molecular plane. (c) Projection of CO hindered translation eigenvectors onto the C_6Br_6 molecular plane. Red and blue segments correspond to the lower and higher vibrational energies respectively. They are overlaid with a scaled C_6Br_6 model to locate the atom positions.

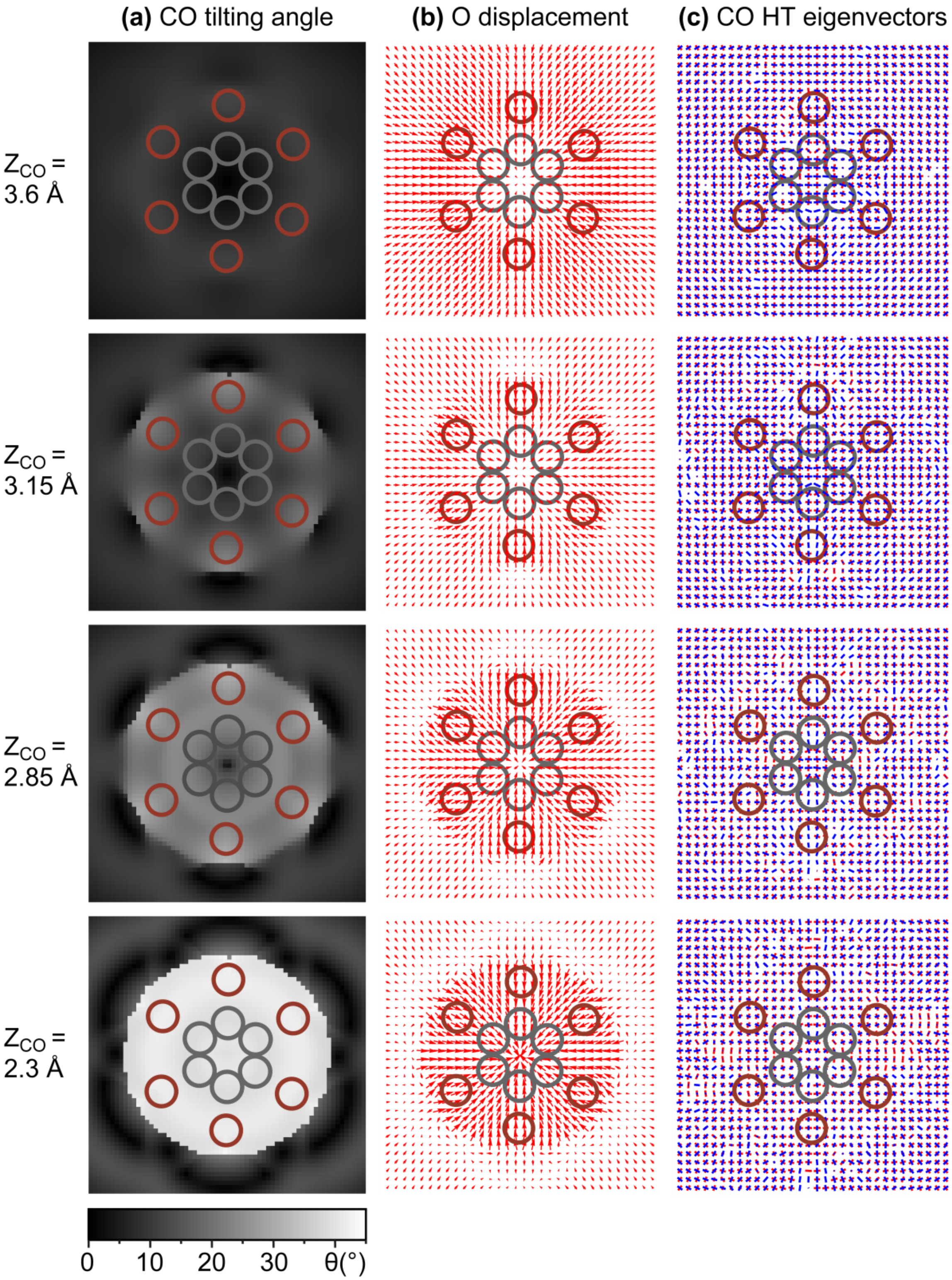
(a) CO tilting angle
(b) O displacement
(c) CO HT eigenvectors
Z_{CO} = 3.6 Å
Z_{CO} = 3.15 Å
Z_{CO} = 2.85 Å
Z_{CO} = 2.3 Å
0
10
20
30
θ(°)

Bibliography

[1] L. Gross, F. Mohn, N. Moll, P. Liljeroth, and G. Meyer, Science **325**, 1110 (2009).

[2] R. Temirov, S. Soubatch, O. Neucheva, A. C. Lassise, and F. S. Tautz, New J. Phys. **10**, 53012 (2008).

[3] C. Chiang, C. Xu, Z. Han, and W. Ho, Science **344**, 885 (2014).

[4] L. Gross, F. Mohn, N. Moll, B. Schuler, A. Criado, E. Guitián, D. Peña, A. Gourdon, and G. Meyer, Science **337**, 1326 (2012).

[5] D. G. de Oteyza, P. Gorman, Y.-C. Chen, S. Wickenburg, A. Riss, D. J. Mowbray, G. Etkin, Z. Pedramrazi, H.-Z. Tsai, A. Rubio, M. F. Crommie, and F. R. Fischer, Science **340**, 1434 (2013).

[6] J. Zhang, P. Chen, B. Yuan, W. Ji, Z. Cheng, and X. Qiu, Science **342**, 611 (2013).

[7] C. Weiss, C. Wagner, C. Kleimann, M. Rohlfing, F. S. Tautz, and R. Temirov, Phys. Rev. Lett. **105**, 86103 (2010).

[8] G. Kichin, C. Weiss, C. Wagner, F. S. Tautz, and R. Temirov, J. Am. Chem. Soc. **133**, 16847 (2011).

[9] D. Yuan, Z. Han, G. Czap, C.-L. Chiang, C. Xu, W. Ho, and R. Wu, J. Phys. Chem. Lett. **7**, 2228 (2016).

[10] M. Ternes, C. P. Lutz, C. F. Hirjibehedin, F. J. Giessibl, and A. J. Heinrich, Science **319**, 1066 (2008).

[11] Z. Sun, M. P. Boneschanscher, I. Swart, D. Vanmaekelbergh, and P. Liljeroth, Phys. Rev. Lett. **106**, 46104 (2011).

[12] A. J. Weymouth, T. Hofmann, and F. J. Giessibl, Science **343**, 1120 (2014).

[13] P. Hapala, G. Kichin, C. Wagner, F. S. Tautz, R. Temirov, and P. Jel ńek, Phys. Rev. B **90**, 85421 (2014).

[14] P. Hapala, R. Temirov, F. S. Tautz, and P. Jel ńek, Phys. Rev. Lett. **113**, 226101 (2014).

[15] B. C. Stipe, M. A. Rezaei, and W. Ho, Rev. Sci. Instrum. **70**, 137 (1999).

[16] B. C. Stipe, M. A. Rezaei, and W. Ho, Science **280**, 1732 (1998).

[17] C. Moreno, O. Stetsovych, T. K. Shimizu, and O. Custance, Nano Lett. **15**, 2257 (2015).

[18] J. van der Lit, F. Di Cicco, P. Hapala, P. Jelinek, and I. Swart, Phys. Rev. Lett. **116**, 96102 (2016).

[19] P. Hapala, M. Švec, O. Stetsovych, N. J. van der Heijden, M. Ondráček, J. van der Lit, P. Mutombo, I. Swart, and P. Jel ńek, Nat. Commun. **7**, 11560 (2016).

[20] Z. Han, G. Czap, C. Chiang, C. Xu, X. Wei, Y. Zhang, R. Wu, and W. Ho, (unpublished).

[21] J. A. Stroscio and R. J. Celotta, Science **306**, 242 (2004).

[22] Y.-H. Zhang, P. Wahl, and K. Kern, Nano Lett. **11**, 3838 (2011).

[23] H. Kim and Y. Hasegawa, Phys. Rev. Lett. **114**, 206801 (2015).

[24] L. Gross, N. Moll, F. Mohn, A. Curioni, G. Meyer, F. Hanke, and M. Persson, Phys. Rev. Lett. **107**, 86101 (2011).

[25] W. L. Jorgensen, Http://dasher.wustl.edu/ffe/distribution/params/oplsaa.prm (2008).

[26] N. J. van der Heijden, P. Hapala, J. A. Rombouts, J. van der Lit, D. Smith, P. Mutombo, M. Švec, P. Jelinek, and I. Swart, ACS Nano, Article ASAP, acsnano.6b03644 (2016).

[27] C. Xu, C. Chiang, Z. Han, and W. Ho, Phys. Rev. Lett. **116**, 166101 (2016).

Chapter 6

Development of a 55 L/day Helium Liquefaction System with Two Gifford-McMahon Cryocoolers*

6.1 Abstract

We have developed a small-scale helium liquefaction system based on commercial Gifford-McMahon cryocoolers. The liquefaction system contains two stages of cryogenic helium gas purifiers and two identical liquefiers connected in parallel with a vacuum-jacketed transfer line. The liquefaction rate of the whole system reaches more than 55 L/day on average for one complete liquefaction-extraction cycle. Here we describe the design, operation and performance of the system.

---

* This chapter by Z. Han, C. Xu, C. Chiang, A. Yu, G. Czap and W. Ho is prepared for submission to *Review of Scientific Instruments*.

6.2 Article

Helium is a nonrenewable resource and plays an irreplaceable role for cryogenic purposes in scientific research and medical applications. However, the limited production and increased demand of helium in recent years led to a worldwide shortage of helium supply and dramatic price increases [1,2]. It has become economically necessary to recycle and liquefy helium for guaranteed continuous cryogenic operations. Although the Collins type helium liquefaction plant [3] has a high liquefaction rate (~100 L/hour), it is too large for most research labs with daily liquid helium (LHe) consumption around 10-50 L. In addition, the initial investment and maintenance costs are high. Developments in magnetic regenerative materials [4–8] made 4 K cryocoolers commercially available that can be used to liquefy helium gas to meet the need for small LHe users.

In the last two decades, significant efforts have been made to develop small-scale helium liquefiers based on pulse-tube cryocoolers [9–14] or Gifford-McMahon (GM) cryocoolers [15,16]. However, there is still a considerable room to improve the performance in terms of liquefaction energy efficiency compared to Collins type helium liquefiers. Different designs and operation strategies have been applied to enhance the liquefaction rate of these systems [11,12,16], such as arrangement of helium gas flow path [9–13], attachment of heat exchangers on cold head [11,12] and adjustment of helium operation pressure [16]. In the meantime, cryogen-free cryostats with cryocoolers have been introduced in an attempt to replace the conventional continuous-flow and bath-cryostats that rely on LHe cooling. However, the vibration-induced low frequency noise presents a large obstacle for their use in vibration sensitive applications, such as low temperature scanning probe measurements [17].

The purity of the helium gas is crucial for the efficient operation of cryocooler-based helium liquefiers. It directly determines the liquefaction rate and decontamination service frequency. Hence the recycled helium gas needs to be purified before use to reach the best performance. Most commercially available cryogen-cooled purifiers are set as separated modules. The purified gas is warmed up and stored at room temperature before liquefaction which wastes the cooling power of the purifiers.

We developed an efficient and reliable small-scale helium liquefaction system to support our low-temperature scanning tunneling microscopes, which integrates the helium gas purifier with the liquefier as a complete system. It produces >55L/day of LHe which covers our daily consumption for one continuous-flow cryostat. The system includes two stages of liquid nitrogen-cooled gas purifiers and two separate helium liquefiers connected in parallel. Each liquefier is equipped with a 4K GM cryocooler. The first stage purifier is easy to regenerate and the rest of the system can operate for several months without interruption. Purified cold helium gas is directly fed into the liquefiers through a vacuum-jacketed (VJ) transfer line. A heat exchanger made of copper foam is attached on the first cooling stage to enhance the efficiency of heat transfer. By controlling the operation pressure of the liquefiers, the liquefaction rate can be optimized. In this communication, we describe the design, operation and performance of the system.

As shown in Fig. 6.1, the helium liquefaction system herein consists of a gas purification system, liquefiers, gas transfer line and flow control system. The purification system includes two stages of cryogenic gas purifiers connected in series. The first stage purifier is served as the pre-purifier and the second stage is served as the main purifier. Two independent helium liquefiers are connected to the main purifier through a T-shape VJ transfer line which features valves to optionally isolate either liquefier.

Recycled helium gas is compressed and stored in high-pressure cylinders as shown in Fig. 6.1. It is first purified and precooled through two purifiers successively. Then the purified cold gas is distributed into two helium liquefiers through the VJ transfer line and liquefied inside the helium Dewar where the cryocooler locates. A LabVIEW program is monitoring and controlling the liquefaction parameters. During the liquefaction process, the liquefier Dewar pressure is maintained at a constant value by automatically adjusting the helium gas flow using a PID algorithm which regulates the flow set point of the helium mass flow controller.

The helium liquefaction rate of cryocooler-based liquefiers highly depends on the helium gas purity. To ensure the best performance, the purity needs to be better than 99.99%. Room temperature helium gas collected from experimental apparatus is initially inflated to a vinyl-based polymer gas bag before compression into high-pressure cylinders. Small amounts of impurities from collection and compression processes, including water vapor, oil vapor and other gases, would condense on the cooling stage of cryocoolers which will weaken the heat exchange between the incoming helium gas and cooling stages. Furthermore, the cryocoolers have to be regenerated to resume liquefying which leads to long servicing times. Both of them reduce the overall liquefaction rate. In our design, the helium gas is first purified with the pre-purifier to remove most of the impurities and further purified with the main purifier. Both purifiers use the liquid nitrogen to condense and trap any impurities with higher boiling point than nitrogen.

The pre-purifier as shown in Fig. 6.2(a) is designed to be simple and easy to regenerate. It consists of two concentric tubes. The outer tube is inserted to a 35 L - 50 L liquid nitrogen Dewar and cooled by the liquid nitrogen surrounding it. The gas inlet is connected to the outer tube. As the helium gas passes through, most impurities including water vapor, oil vapor and other gases are condensed on the inner wall of the outer tube before reaching the bottom of the inner tube. The remaining gas flows through the inner tube that connects to the main purifier inlet. When there is a significant pressure drop between the gas inlet and outlet (> 10 psig), the pre-purifier needs to be regenerated. However, it takes less than one hour to remove the trapped impurities which clog the pre-purifier every 1-2 months.

The main purifier resides in a 200 L liquid nitrogen Dewar as shown in Fig. 6.2(b). The purifier chamber hangs from the top flange and is supported by the inlet and outlet tubes. The body is filled with porous materials, such as zeolite and activated charcoal. Particle filters are installed at the inlet and outlet tubes to retain zeolite pellets and powder inside the purifier chamber. The zeolite pellets are cooled by the liquid nitrogen bath surrounding the purifier chamber. As helium gas penetrates through the zeolite, most contaminants are trapped within the zeolite. Since the majority of the impurities have been removed by the pre-purifier, the main purifier can be operated continuously for more than six months without regeneration.

Purified helium gas from the main purifier is around 90 K. A T-shape VJ transfer line is inserted into the main purifier and connected to two liquefiers in parallel. The cold purified helium gas is distributed directly into two liquefiers through the VJ transfer line which minimizes the heat loss and reduces possibility of secondary contamination.

The reduction of inlet helium gas temperature to the liquefiers could significantly improve the liquefaction rate of cryocooler based liquefiers [18]. The liquefaction rate with 90 K helium gas is expected to be higher than the room temperature gas, since the cryocooler does not waste its cooling power to cool the gas from 300K to 90K. In addition, the cold helium gas can be applied to pressurize the liquefier Dewar to withdraw LHe. Two VJ valves on each side of the branch of the T transfer line are used to control the flow of helium gas, so that either liquefier can be isolated from the rest of the system.

The helium liquefier consists of a LHe Dewar, an adaptor flange, a two-stage GM cryocooler, electrical sensors and other attachments on the cold head as shown in Fig. 6.3(a). It utilizes the natural convective heat transfer to cool the helium gas to liquid.

The LHe Dewar is custom-made by Cryofab with a wide neck. The cooling stages of the cryocooler locate inside the neck; that's also the space where helium gas get cooled and condensed. There is also a side neck with smaller diameter which accommodates a superconducting LHe level sensor and LHe extract port.

The cryocooler is coupled to the helium Dewar with an adaptor flange. The cold head assembly with heat exchangers, sensors and other attachments can be easily installed or removed from the Dewar as a complete assembly with the adaptor flange. In order to minimize the radiation from the outside of the Dewar, the inner diameter of the neck needs to be as small as possible [12]. To shrink the neck diameter, the helium gas inlet, electrical feedthroughs for sensors, safety relief devices and the Dewar evacuation port are located to the side of the adaptor flange instead of entering from the topside. Three layers of radiation baffles are attached to the adaptor flange above the first cooling stage to reduce the thermal radiation load.

The Sumitomo RDK-415D2 cryocooler is used in our system. It is a double-stage GM cryocooler with a typical cooling power of 1.5 W on the second cooling stage at 4.2 K. A custom-designed open-cell copper foam heat exchanger is mounted on the first cooling stage to increase the heat load. The open-cell copper foam is highly porous and permeable with a high surface area-to-volume ratio. It is light but rigid with high thermal conductivity, which makes it an ideal material for a heat exchanger. The copper foam heat exchanger exerts resistance to the helium gas flow which increases the dwelling time for the gas inside the foam to increase the effectiveness of the heat exchanger.

The incoming helium gas is led into the copper foam heat exchanger through a sealed stainless steel tubing. Then the helium gas is pushed through the copper foam and diffuses across the first cooling stage to the second cooling stage driven by natural convection.

The gas is then further cooled down while it passes through the layers of regularly spaced annular fins attaching to the stainless steel cylinder between the first and second cooling stages. These fins are made of perforated copper sheets which minimizes the influence on the downward convection flow. The helium gas is finally cooled down to the liquefaction temperature by the second cooling stage. Some of the gas condenses and the rest flows downwards around the center of the Dewar following the natural convection pattern due to the thermal gradient and gravity. To increase the helium condensation surface area, the second cooling stage is finned and an additional finned heat exchanger is also thermally anchored to the second cooling stage.

A stainless steel thermal shield is attached to the bottom of heat exchanger housing, which extends all the way from the first cooling stage to the second stage. Kapton tape heaters are attached to the first and second cooling stages to accelerate the decontamination process in case servicing is necessary. Most of the contaminant is solid nitrogen, which melts when the first cooling stage heats above 63K.

All electrical measurements from sensors and controlling commands are accessible in a LabVIEW program. The inlet gas flow, the temperatures at the first and second cooling stages of both liquefiers, the pressure of the main purifier and both liquefiers are being monitored and recorded in real time. The LabVIEW program is also available for remote access on internet.

The pressure of the liquefier Dewars is controlled precisely by adjusting the inlet gas flow with a helium mass flow controller. The LabVIEW program uses the liquefier Dewar pressure as a feedback parameter to adjust the gas flow using a PID algorithm. Both liquefiers can be running individually or synchronously. When the two liquefiers are running together, the higher pressure of the two Dewars is set as the feedback parameter for safety considerations.

A typical liquefaction cycle lasts about 5 to 6 days for our system as shown in Fig. 6.4. The liquefaction cycle can be divided into three stages: (a) isobaric precooling stage that cools the incoming helium gas at 90 K to saturation temperature, which usually corresponds to the first day of the cycle, (b) liquefying stage that the saturated LHe is produced at a constant pressure, corresponding to the period ranging from day 2 to day 5; (c) depressurizing stage in which the gas flow is stopped and the saturated LHe is further cooled to a 4.2 K before extraction.

According to cooling load map of the cryocooler [16], the cooling power that can be extracted is highly correlated with its temperature. By increasing the operation pressure at stage (a) and (b), the helium gas can be liquefied at a higher temperature than 4.2 K while the cryocooler can also provide higher cooling power at higher temperatures. In addition, the enthalpy difference between gas and liquid states is also lower at higher pressure which reduces the heat needed to be removed to liquefy. Therefore the liquefaction rate is greatly enhanced at higher operation pressures [16]. For our system, the liquefiers are set to run at a constant pressure ~ 18 psig for stages (a) and (b) as shown in Fig. 6.4(c). During the complete liquefaction cycle shown Fig. 6.4(d), a total of 312 L of LHe is produced within 135 hours, which corresponds to an average liquefaction rate of 55.5 L/day.

LHe is transferred out to a movable Dewar one liquefier at a time. During a transfer, one liquefier Dewar is pressurized with purified and precooled helium gas from the cryogenic purifiers, while the other one is isolated by closing the corresponding VJ valve on the T-shape transfer line. Consequently the boiling off of LHe is significantly reduced compared with room temperature helium gas pressurization. The liquefier is allowed to run continuously during the transfer to further suppress the transfer loss of LHe. With consecutive transfer of 300 L LHe out of the two liquefiers, less than 10 L helium exhaust gas is generated.

More importantly, owing to the purification system we have implemented, we can continuously run the liquefiers for more than a half year without regeneration which greatly extends our effective working duty over a long period.

In conclusion, we present an efficient small-scale helium liquefaction system that provides > 55 L/day LHe to support our low temperature scanning tunneling microscope. It incorporates the gas purification and liquefaction as an integrated system connected with a cryogenic transfer line. The pre-purifier is simple but effective in removing most of the impurities in the helium gas which keeps the rest of system running without frequent regeneration.

Figure 6.1. Schematic diagram of the helium recycling system. It consists of the helium gas collection system, helium gas storage system and helium liquefaction system. The green arrows indicate the helium gas flow direction.

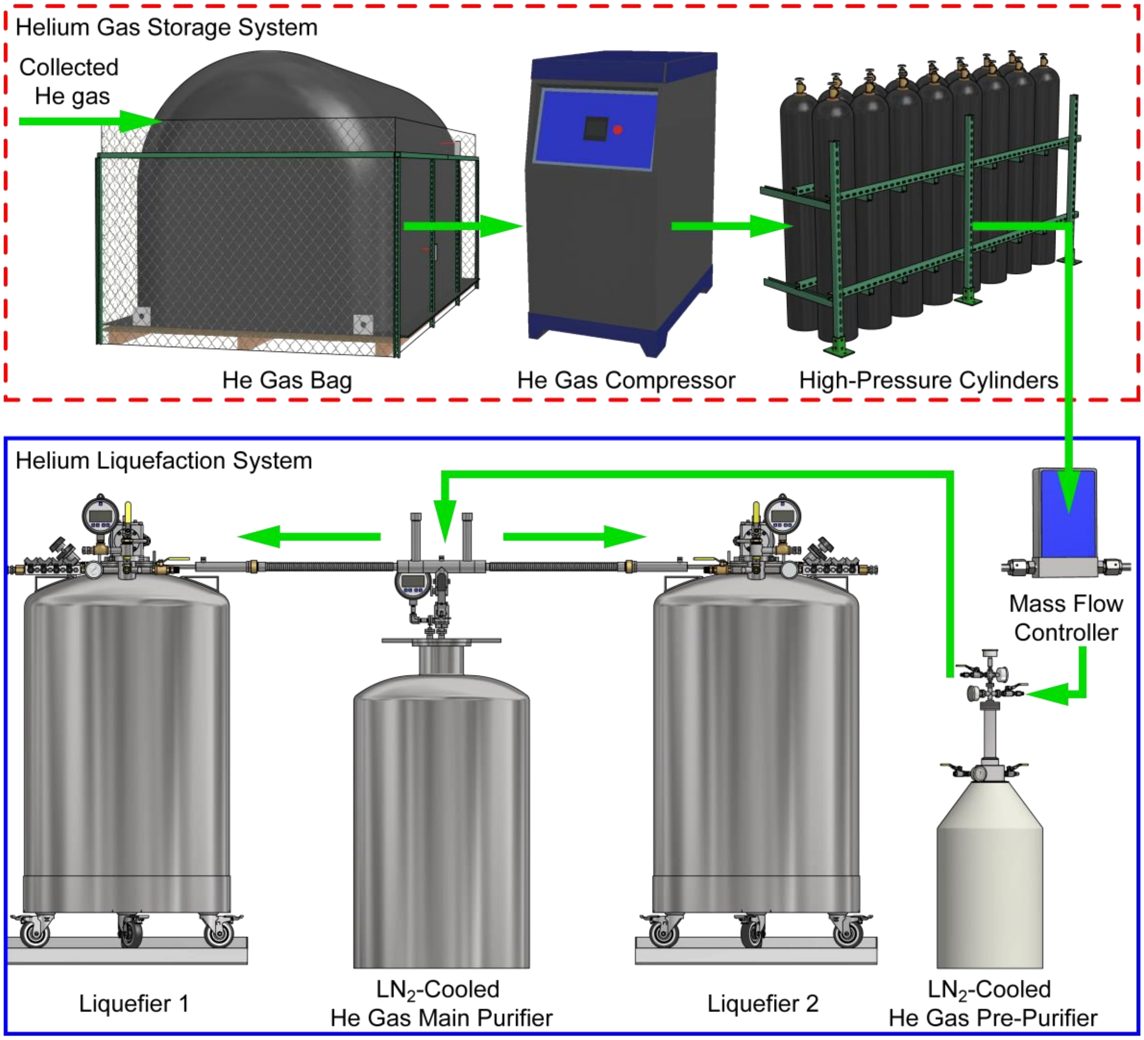
Helium Gas Storage System
Collected He gas
He Gas Bag
He Gas Compressor
High-Pressure Cylinders
Helium Liquefaction System
Mass Flow Controller
Liquefier 1
LN$_2$-Cooled He Gas Main Purifier
Liquefier 2
LN$_2$-Cooled He Gas Pre-Purifier

Figure 6.2. Schematic diagrams of the pre-purifier and main purifier. (a) Pre-purifier assembly which consists of (1) helium gas inlet, (2) helium gas outlet, (3) pressure gauge for inlet gas, (4) pressure gauge for outlet gas, (5) outer tube, (6) inner tube, (7) liquid nitrogen refilling port and (8) liquid nitrogen Dewar. (b) Main purifier assembly which includes (9) helium gas inlet, (10) helium gas outlet, (11) thermal baffles, (12) liquid nitrogen Dewar, (13) inlet tube, (14) outlet tube, (15) zeolite pellets and (16) main purifier chamber.

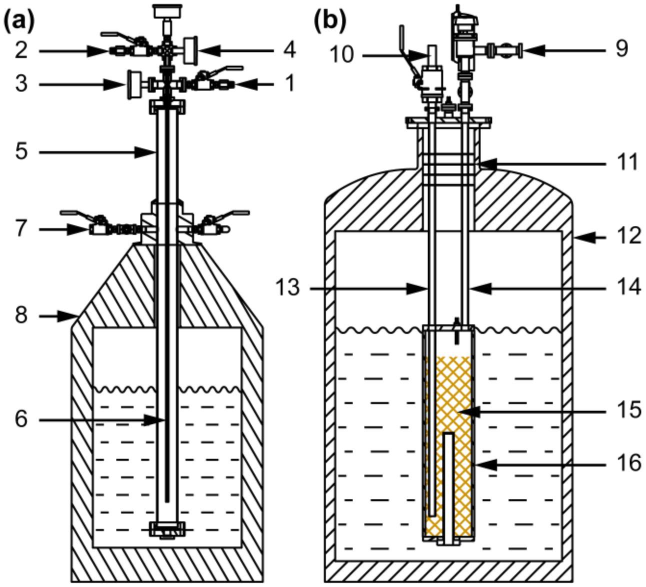
(a)
2
4
3
1
5
7
8
6
(b)
10
9
11
12
13
14
15
16

Figure 6.3. Schematic diagrams of helium liquefier and cold head assembly. (a) Helium liquefier assembly which contains (1) GM cryocooler, (2) LHe Dewar, (3) adaptor flange (4) side neck and (5) superconducting liquid level sensor. (6) Natural convection flows of helium gas inside the Dewar are denoted by blue dashed lines with arrows. (b) Cold head assembly. (7) first cooling stage, (8) finned second cooling stage, (9) sealed tube connection for incoming helium gas, (10) thermal baffle, (11) copper foam heat exchanger , (12) stacks of annular perforated copper fins, (13) stainless steel thermal shield, (14) helium condenser (extra heat exchanger). (c) Photo of cold head assembly without the stainless steel thermal shield.

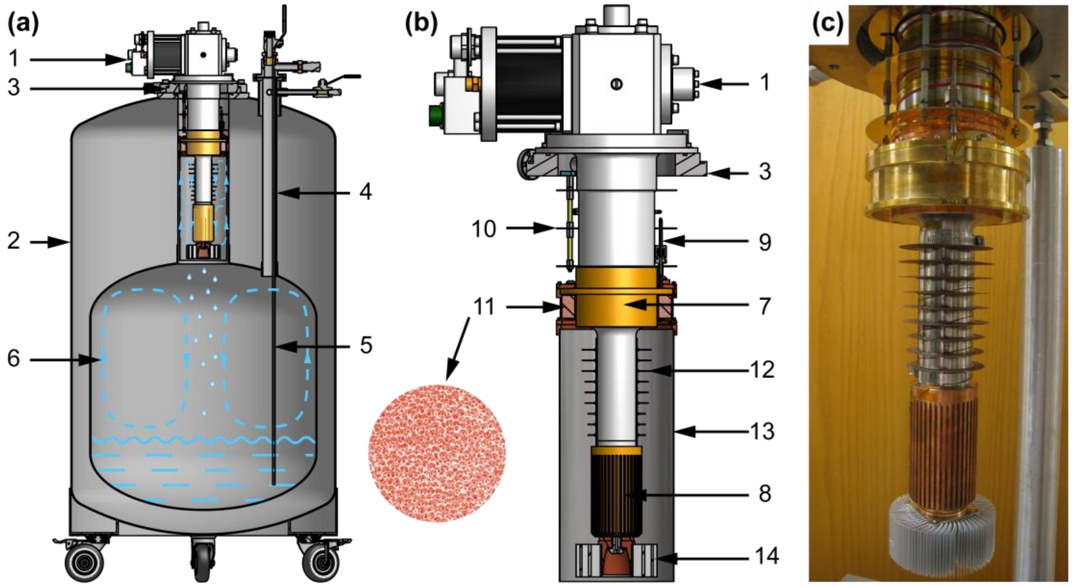
(a)
1
3
4
2
5
6
(b)
1
3
10
9
7
11
12
13
8
14
(c)

Figure 6.4. Performance of the helium liquefaction system. (a) Temperature evolution of the first cooling stage, (b) temperature of the second cooling stage and (c) liquefier Dewar pressure of one liquefier during a complete liquefaction cycle. The other liquefier shows very similar behavior. (d) The accumulated gas flow (red line) and instantaneous helium gas flow during the liquefaction cycle. The black arrow represents the start of the depressurization phase. The pink dashed line indicates the beginning of a LHe transfer out of the liquefier. The flow rate unit SLPM stands for standard liter per minute.

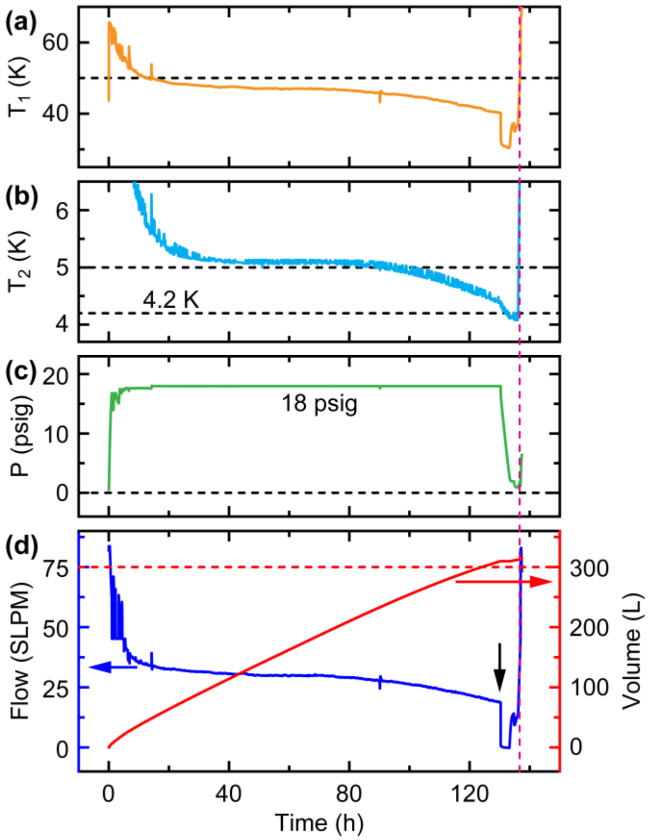

(a)
T₁ (K)
60
40
(b)
T₂ (K)
6
5
4
4.2 K
(c)
P (psig)
20
10
0
18 psig
(d)
Flow (SLPM)
75
50
25
0
Volume (L)
300
200
100
0
0
40
80
120
Time (h)

Bibliography

[1] W. P. Halperin, Nat. Phys. **10**, 467 (2014).

[2] W. J. Nuttall, R. H. Clarke, and B. A. Glowacki, Nature **485**, 573 (2012).

[3] S. C. Collins, in *Adv. Cryog. Eng.* (Springer US, Boston, MA, 1966), pp. 11–15.

[4] H. Yoshimura, M. Nagao, T. Inaguchi, T. Yamada, and M. Iwamoto, Rev. Sci. Instrum. **60**, 3533 (1989).

[5] M. Nagao, T. Inaguchi, H. Yoshimura, T. Yamada, and M. Iwamoto, in *Adv. Cryog. Eng.*, edited by R. W. Fast (Springer US, Boston, MA, 1990), pp. 1251–1260.

[6] T. Kuriyama, R. Hakamada, H. Nakagome, Y. Tokai, M. Sahashi, R. Li, O. Yoshida, K. Matsumoto, and T. Hashimoto, in *Adv. Cryog. Eng.*, edited by R. W. Fast (Springer US, Boston, MA, 1990), pp. 1261–1269.

[7] T. Kuriyama, M. Takahashi, H. Nakagome, T. Eda, H. Seshake, and T. Hashimoto, Jpn. J. Appl. Phys. **31**, L1206 (1992).

[8] T. Satoh, A. Onishi, R. Li, H. Asami, and Y. Kanazawa, in *Adv. Cryog. Eng.* (Springer US, Boston, MA, 1996), pp. 1631–1637.

[9] G. Thummes, C. Wang, and C. Heiden, Cryogenics (Guildf). **38**, 337 (1998).

[10] C. Wang, Cryogenics (Guildf). **41**, 491 (2001).

[11] C. Wang, Cryogenics (Guildf). **45**, 719 (2005).

[12] C. Wang and R. G. Scurlock, Cryogenics (Guildf). **48**, 169 (2008).

[13] C. Wang, Cryogenics (Guildf). **48**, 154 (2008).

[14] C. Wang, J. Phys. Conf. Ser. **150**, 12053 (2009).

[15] P. Schmidt-Wellenburg and O. Zimmer, Cryogenics (Guildf). **46**, 799 (2006).

[16] C. Rillo, M. Gabal, M. P. Lozano, J. Sesé, S. Spagna, J. Diederichs, R. Sager, C. Chialvo, J. Terry, G. Rayner, R. Warburton, and R. Reineman, Phys. Rev. Appl. **3**, 51001 (2015).

[17] S. Zhang, D. Huang, and S. Wu, Rev. Sci. Instrum. **87**, 63701 (2016).

[18] J. H. Baik, S. W. Karng, N. Garceau, Y. H. Jang, C. M. Lim, S. Y. Kim, and I. H. Oh, in *Adv. Cryog. Eng. Trans. Cryog. Eng. Conf. - CEC* (AIP Publishing, 2014), pp. 1357–1364.

Chapter 7

Concluding Remarks and Future Prospects

7.1 Concluding Remarks

In this dissertation, I have described quantitative characterization and real space imaging of intramolecular bonds and intermolecular interactions with single bond sensitivity by advancing three novel applications of a home-made sub-Kelvin scanning tunneling microscope (STM). Owing to the ultra-low temperature at 600 mK, the thermal broadening of STM inelastic electron tunneling spectroscopy (IETS) [1] drops below 0.3 meV and the overall energy resolution reaches about 0.6 meV or 5 cm^{-1}. This enhanced energy resolution readily offers a great opportunity to study subtle vibrational features induced by weak intermolecular interactions which was not accessible previously.

Intermolecular interactions can lead to intermolecular coupled vibrations. We demonstrated the detection of intermolecular coupled vibrations with STM-IETS for the first time. The coupled vibrational energy and the IETS intensity of a CO-CO junction are very sensitive to the intermolecular displacement as revealed in the z-dependent measurement. This unique property of intermolecular coupled vibrations suggests some potential applications, such as chemical identification of non-planar functional groups in a molecule and characterization of molecular adsorption anisotropy.

Intermolecular interactions can also induce shifts in molecular vibrational energy. Based on the detection of CO-tip vibrational energy variation by the STM-IETS, the inelastic tunneling probe (itProbe) technique has been developed to image the bonding structures of a single molecule and self-assembled molecular islands in real space [2]. The nature of intermolecular interaction responsible for the molecular self-assembly is illustrated with the aid of these sub-Ångström resolution itProbe images. Further exploration with itProbe by varying the tip-sample separation suggests the unique advantage of this technique to reveal the local lateral curvature of the potential energy surface between CO and probed molecules in three-dimensional space.

Combination of itProbe technique and high energy resolution STM-IETS at 600 mK gives rise to the detection of adsorption configuration and the associated low-energy external vibrational modes of a single benzene molecule on Ag(110) for the first time [3]. The precise structural imaging and vibrational spectroscopy of single molecules by the STM set a benchmark for testing density functional theory (DFT) calculation with different van der Waals correction methods.

Results obtained from these studies have provided new understanding into the nature of the chemical bond, particularly its relation to the charge density redistribution and the spatial variations of the potential energy surface in 3D. These first experiments suggest unprecedented opportunities to image and reveal chemistry at the atomic scale.

Last but not least, a small scale helium liquefaction system has been developed to recycle and liquefy helium gas. The efficient and steady performance of the system provides a strong support for our low-temperature STM experiments. The system is expanding now in an attempt to support the whole School of Physical Sciences here at UC Irvine.

7.2 Future Prospects

7.2.1 Further Studies of Intermolecular Coupled Vibrations

A phonon is a collective motion of atoms (or molecules) in a lattice which is the interatomic (or intermolecular) coupled vibration for a group of atoms (molecules). Phonons play a very important role for thermal conductivity and electrical conductivity of condensed matter. However, few studies have been done on the “zero dimensional (0D)” phonon which is the intermolecular coupled vibration. Chapter 2 describes the first experimental detection and characterization about the 0D phonon on single molecule level. There are still lots of interesting questions to be answered.

In Chapter 2 the intermolecular coupled vibration mode is described for a vertically arranged molecular tunneling junction. In a laterally arranged CO dimer, the intermolecular interaction may be also strong enough to induce coupled vibrations. The contrast inversion for a CO dimer on Cu(111) [4] indicates there is some electrical coupling between the two CO molecules. It is of fundamental interest to see how the evolution from 0D coupled vibrations to one-dimensional (1D) and two-dimensional (2D) phonons occurs by artificially positioning the CO molecules on a surface with tip manipulation. In addition to the spatially resolved STM-IETS characterization, IETS imaging can be conducted to visualize phonon density distribution in real space. Furthermore impurities/defects can be introduced into the CO 1D chain or 2D lattice to study the phonon scattering. A CO-tip can be used to bring some coupling into the system from a different dimension in z. It should be noted that 1D self-assembled CO chains with different lengths on the Cu(110)-(2×1)-O surface has been reported [5] which also serves as a good system to try.

The one-dimensional coupled harmonic oscillator model introduced in Chapter 1 provides a lot of fruitful insights into how the different parameters could affect intermolecular coupled vibrations. It can be used as a guide for experimental design to tune parameters such as the effect masses, spring constants and coupling strength. For example different types of molecules, functional groups or intermolecular interaction would lead to distinct spatial variations of the coupled vibrational mode. Therefore spatially resolved STM-IETS measurement and imaging would potentially provide a deeper understanding of the nature of different intermolecular interactions and the STM-IETS selection rules of hybrid molecular junctions.

7.2.2 Alternative Probe Molecules for the itProbe technique

As mentioned in Chapter 1, Hapala’s mechanical model [6,7] and Gross’s original simulation [8,9] both reproduce the major features in the high resolution scanning probe images. Hapala’s model assumes the interaction between the probe atom on the tip and surface molecule is centered at the location of individual constituent atoms in the molecule. Gross’s model assumes the CO-tip is “sharp” enough to directly trace the local electron density accumulation regions where the chemical bonds and atoms locate. To clarify these two models with itProbe technique, a different probe molecule with smaller van der Waals radius is need.

Active searching for the right candidate molecule is still underway and the criteria are primarily composed of three prerequisites: 1. the molecule must exhibit a low energy vibrational mode that is sensitive to intermolecular interaction; 2. the low energy vibrational mode has a decent IETS cross-section; and 3. the molecule can be transferred to the tip in a controllable and reproducible manner. Molecules terminated with hydroxyl or thiol groups can be the possible candidates.

The current itProbe technique is driven by molecular vibrational inelastic excitation. However, other inelastic excitations have also been demonstrated in STM-IETS, such as spin-flip excitations [10]. In principle a magnetic version of itProbe can be devised by transferring a magnetic molecule with free spin to the tip. This magnetic tip can then be applied to probe another magnetic molecule or atom on surface. By detecting of the spin-flip IETS as a function of tip positions, the spatial distribution of the magnetic coupling can be visualized in real space. The magnetic itProbe is also relying on selection of a proper molecule or nanostructure as the probe. In addition, a decoupling layer is required between the metallic tip and the spin center of the molecule to preserve the magnetic moment on molecule. Radicals with an unpaired electrons, such as (2,2,6,6-tetramethylpiperidin-1-yl)oxyl (TEMPO) molecules, as well as a chargeable organic molecule could be considered [11].

There is a simpler system to test the mechanisms behind magnetic itProbe. Instead of having a free spin on the tip to probe a fixed magnetic moment on surface, a reversed geometry is much easier to realize experimentally. The tip can be spin-polarized to create a strong local magnetic field over a magnetic molecule or atom on surface. The tip is coated with magnetic atoms by either thermal evaporation or by locally transferring atoms from the surface. The magnetic atoms and molecules are deposited on a decoupler such as a metal oxide surface and molecular layers to preserve the magnet moments. The local magnetic field or magnetic coupling will be characterized with the Zeeman splitting energy as a function of tip-sample separation. A chargeable molecule [12,13] on a decoupling layer may serve as tunable spin center for controlled experiments.

7.2.3 In-plane Transport Measurements on Two-Dimensional Materials with the STM

A class of two-dimensional (2D) materials made up of a single atomic layer have attracted extensive attention over the last decade since graphene was discovered in 2004 [14]. More and more materials in addition to graphene have been introduced into this category, such as borophene made of boron, germanene made of germanium, silicene made of silicon, phosphorene made of phosphorous and stanene made of tin [15]. These 2D materials have unique electronic properties since electron motion is confined in 2D space. While most studies of 2D materials with STM have been focused on the morphology and local electronic band structures with the out-of-plane tunneling electrons, it is highly desired to have the capability to perform in-plane transport characterization simultaneously with spatially resolved out-of-plane STM measurement. For example, the tip can be used as local gate to tune local the band structure of the 2D material which may tune the in-plane electron flow. Furthermore, the spatial dependent interplay between the in-plane conductive and the tunneling current as well as local gating can be characterized and imaged [16].

The schematic diagram for the proposed experimental setup is shown in Fig. 7.1. The 2D material, such as graphene, is supported on SiO_2/Si wafer. Two gold electrodes are connected across the 2D material served as the source and drain; another electrode is placed at the backside of the sample for the back gate. The source-drain voltage V_{sd} and the in-plane current are measured together. An out-of-plane sample bias V_b is applied to the drain and the tunneling current is collected by the tip. The 2D material can be back-gated with V_g or locally gated through the tip. In this configuration, at least three electrical connections need to be made to the sample. We designed a split sample holder for the proposed experiment. The more detailed description about the sample holder design can be found in the Appendix B.

7.2.4 Further Improvement on the Helium Liquefaction System

Our home-made helium liquefaction system is very reliable and efficient. However, there are still a few components that can be improved.

The main helium gas purifier can be converted into a cryogen-free gas purifier. In our current design, the main helium gas purifier is housed inside a 200 L nitrogen Dewar. The cooling power is provided by the surrounding liquid nitrogen. The cryogen-free gas purifier will have a few advantages compared to the current design.

1. The cryogen-free gas purifier is cooled by a single stage or double stage high power Gifford-McMahon cryocooler, so we don’t need to refill the liquid nitrogen anymore. More importantly we can replace the expensive custom made nitrogen Dewar with a more compact and cheaper vacuum chamber. In addition, the diameter of the

current purifier is limited by the neck size of the nitrogen Dewar. We can make the main purifier much bigger in the new design to extend the regeneration period.

2. The heat transfer between the liquid nitrogen and the zeolite inside purifier across the stainless steel wall is not very effective. The temperature of purified helium is around 90 K or higher. In the new design, zeolite will have much better thermal contact with the cooling stage(s) on the cryocooler through the surrounding helium gas. Therefore the purified gas will have lower temperature and higher purity which will potentially enhance the liquefaction rate.

3. The current design has very big cooling power from liquid nitrogen. However, lots of the cooling power is wasted when the liquid nitrogen is vaporized and vented as cold gas.

4. In the current design, we need to pull the purifier out of the liquid nitrogen Dewar to regenerate and install back afterwards. With the new design, the purifier can be baked right inside the vacuum chamber which can save a lot of time.

Some designs for the liquefier parts can also be simplified or replaced with other commercially available products.

1. The copper foam heat exchanger attached on the first cooling stage. Currently the copper foam is soldered into a thin-wall copper housing which is very difficult to machine. This piece would be much easier to make if the inner wall is removed. In the meantime the copper foam inner diameter should be modified to obtain a tight fit with the outer diameter of the first cooling stage on the cryocooler.

2. The annular fins attached to the stainless steel cylinder between the first and second cooling stages. This attachment is made of copper disks soldered on a grooved

stainless steel tube. It can be replaced with commercially available finned tube with small modification on the tube inner diameter.

Figure 7.1. Schematic diagram of experimental setup to perform in-plane transport measurements on 2D materials with the STM.

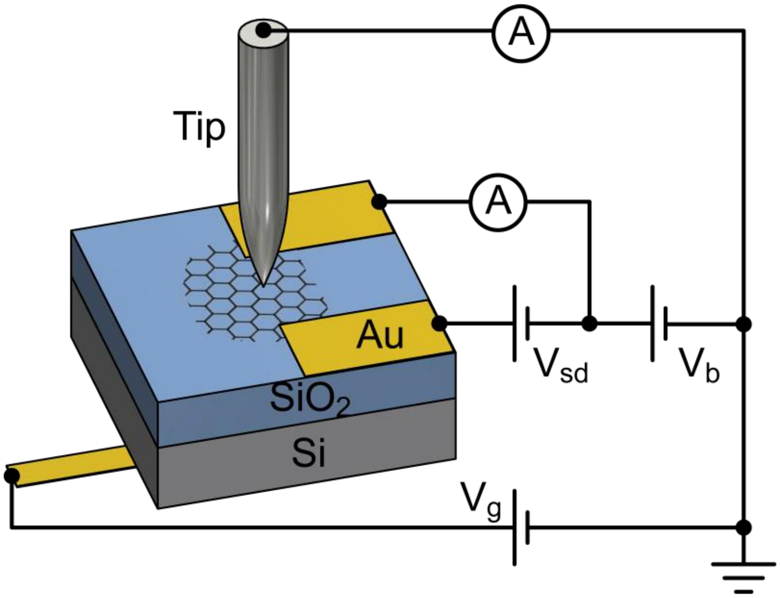
A
Tip
A
Au
V_{sd}
V_b
SiO_2
Si
V_g

Bibliography

[1] B. C. Stipe, M. A. Rezaei, and W. Ho, Science **280**, 1732 (1998).

[2] C. Chiang, C. Xu, Z. Han, and W. Ho, Science **344**, 885 (2014).

[3] D. Yuan, Z. Han, G. Czap, C.-L. Chiang, C. Xu, W. Ho, and R. Wu, J. Phys. Chem. Lett. **7**, 2228 (2016).

[4] A. J. Heinrich, Science **298**, 1381 (2002).

[5] M. Feng, C. Lin, J. Zhao, and H. Petek, Annu. Rev. Phys. Chem. **63**, 201 (2012).

[6] P. Hapala, G. Kichin, C. Wagner, F. S. Tautz, R. Temirov, and P. Jelínek, Phys. Rev. B **90**, 085421 (2014).

[7] P. Hapala, R. Temirov, F. S. Tautz, and P. Jelínek, Phys. Rev. Lett. **113**, 226101 (2014).

[8] L. Gross, F. Mohn, N. Moll, P. Liljeroth, and G. Meyer, Science **325**, 1110 (2009).

[9] N. Moll, L. Gross, F. Mohn, A. Curioni, and G. Meyer, New J. Phys. **12**, 125020 (2010).

[10] A. J. Heinrich, J. A. Gupta, C. P. Lutz, and D. M. Eigler, Science **306**, 466 (2004).

[11] C. Wagner, M. F. B. Green, P. Leinen, T. Deilmann, P. Krüger, M. Rohlfing, R. Temirov, and F. S. Tautz, Phys. Rev. Lett. **115**, 026101 (2015).

[12] S. W. Wu, N. Ogawa, and W. Ho, Science **312**, 1362 (2006).

[13] Y.-S. Fu, T. Zhang, S.-H. Ji, X. Chen, X.-C. Ma, J.-F. Jia, and Q.-K. Xue, Phys. Rev. Lett. **103**, 257202 (2009).

[14] K. S. Novoselov, A. K. Geim, S. V Morozov, D. Jiang, Y. Zhang, S. V Dubonos, I. V Grigorieva, and A. A. Firsov, Science **306**, 666 (2004).

[15] G. R. Bhimanapati, Z. Lin, V. Meunier, Y. Jung, J. Cha, S. Das, D. Xiao, Y. Son, M. S. Strano, V. R. Cooper, L. Liang, S. G. Louie, E. Ringe, W. Zhou, S. S. Kim, R. R. Naik, B. G. Sumpter, H. Terrones, F. Xia, Y. Wang, J. Zhu, D. Akinwande, N. Alem, J. A. Schuller, R. E. Schaak, M. Terrones, and J. A. Robinson, ACS Nano **9**, 11509 (2015).

[16] M. A. Topinka, R. M. Westervelt, and E. J. Heller, Phys. Today **56**, 47 (2003).

Appendix A

STM-IETS Calibration Software

During a STM-IETS measurement, the recorded first and second harmonic signals from a lock-in amplifier are in the unit of Volts. The voltage numbers only reflect the relative strength of the signal and they are relying on a lot of instrumental settings such as modulation amplitude and sensitive settings of the lock-in amplifier in addition to the current to voltage gain of the preamplifier. Therefore these data need to be calibrated to get the physical absolute value in order to compare among different spectra. A user-friendly LabVIEW software has been developed to calibrated the IETS as shown in Fig. A.1. It allows the users to select the data and perform the calibration at one place.

Normally, we record the tunneling current as well as the first and second harmonic data simultaneously during STM-IETS measurement. They will all be used as the input data files for the calibration. Only the tunneling current and second harmonic data are required. We can still perform the calibration if the first harmonic data is not available as will be mentioned bellow.

The principle behind the calibration is quite simple. In addition to a constant offset, the measured first harmonic (S_1) and second harmonic (S_2) signals are proportional to the real first derivative and second derivative of the current with respect to the sample bias (dI/dV and d^2I/dV^2).

$$\frac{dI}{dV}(V) = a_1 S_1(V) + b_1. \tag{A.1}$$

$$\frac{d^2I}{dV^2}(V) = a_2S_2(V) + b_2. \tag{A.2}$$

The purpose of the calibration is to find the best coefficients (a_1, b_1, a_2 and b_2) for the *dI/dV* and d^2I/dV^2. These coefficients can also be applied to calibrate the itProbe images with the same instrumental settings.

By integrating Eq. B.1 on both sides we get

$$I(V) - I(V_0) = \int_{V_0}^{V} dV \frac{dI}{dV}(V) = a_1 \int_{V_0}^{V} dV\, S_1(V) + b_1(V - V_0). \tag{A.3}$$

It can also be written as

$$I(V) = a_1 \int_{V_0}^{V} dV\, S_1(V) + b_1V + c_1. \tag{A.4}$$

Similarly, by integrating Eq. B.2 we get

$$\frac{dI}{dV}(V) = a_2 \int_{V_0}^{V} dV\, S_2(V) + b_2V + c_2. \tag{A.5}$$

This means we can use linear regression to fit the measured current with the integrated first harmonic signal to get the coefficients a_1, b_1, and c_1. Once we get the calibrated first derivative $a_1S_1(V) + b_1$, we can fit it with the integration of the second harmonic signal to obtain a_2, b_2, and c_2.

Alternatively, we can integrate $S_2(V)$ twice and fit that to the tunneling current in case we only record the current and second harmonic signals during the experiment.

$$I(V) = a_2 \int_{V_0}^{V} dV \int_{V_0}^{V} dV\, S_2(V) + \frac{1}{2}b_2V^2 + c_2V + d. \tag{A.6}$$

Figure A.1. Screenshot of the STM-IETS calibration software with LabVIEW.

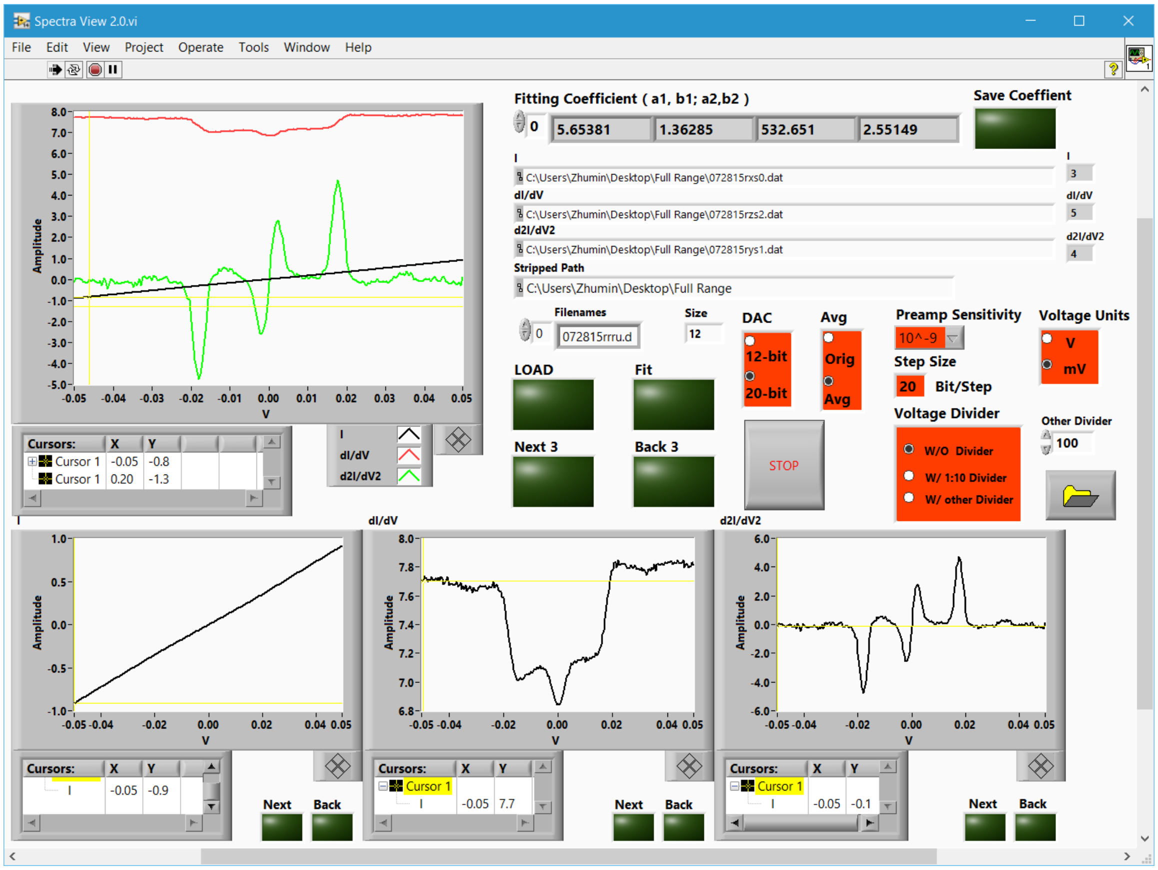

Fitting Coefficient (a1, b1; a2,b2): 0 | 5.65381 | 1.36285 | 532.651 | 2.55149

I: C:\Users\Zhumin\Desktop\Full Range\072815rxs0.dat — I: 3

dI/dV: C:\Users\Zhumin\Desktop\Full Range\072815rzs2.dat — dI/dV: 5

d2I/dV2: C:\Users\Zhumin\Desktop\Full Range\072815rys1.dat — d2I/dV2: 4

Stripped Path: C:\Users\Zhumin\Desktop\Full Range

Filenames: 0 | 072815rrru.d

Size: 12

DAC: ○ 12-bit ● 20-bit

Avg: ○ Orig ● Avg

Preamp Sensitivity: 10^-9

Step Size: 20 Bit/Step

Voltage Units: ○ V ● mV

Voltage Divider: ● W/O Divider ○ W/ 1:10 Divider ○ W/ other Divider

Other Divider: 100

Cursors:	X	Y
Cursor 1	-0.05	-0.8
Cursor 1	0.20	-1.3

Cursors:	X	Y
I	-0.05	-0.9

Cursors:	X	Y
Cursor 1		
I	-0.05	7.7

Cursors:	X	Y
Cursor 1		
I	-0.05	-0.1

Appendix B

Split Sample Holder Design for the in-Plane Transport Measurements with the STM

The wiring diagram of the in-plane transport measurement with our scanning tunneling microscope (STM) is shown in Fig. B.1. Our homemade STM scanner [1] is of the Besocke-type design [2]. It has four piezos with identical dimension and material. The sample holder contains three ramps which are supported by three equilaterally spaced outer piezos. The scanning tip is inserted in the socket inside the central piezo. During the measurement, the outer three piezos control the fine lateral motion of the sample and the inner piezo is responsible for the vertical motion of the tip.

In our existing wiring configuration, the tip is connected to a current preamplifier for current measurement and the sample is biased through tungsten balls mounted on the outer piezos. The three tungsten balls are typically electrically connected by the molybdenum sample holder. Here, we split the sample holder into three individual pieces with one ramp on each piece as shown in Fig. B.2. The three ramps are held together by a sapphire disk with six screws which serves to isolate the three ramps. A central hole on the disk improves the sample heating efficiency from the backside. The separated ramps can then be used for biasing and gating through the tungsten balls. As shown in Fig. B.2, the source and drain electrodes are connected to the ramps with two tantalum tabs on the top side of the sample. The back-gate is connected to the backside of the sample through a gold strip while the top side is isolated from the third tab with a sapphire hemisphere. A smaller sapphire plate is sandwiched between the sample and sample holder so that the Si wafer doesn’t contact any of the ramps directly.

A sample holder with asymmetric planar ramps often exhibits significant horizontal sliding during the tip approach. Since the typical dimension of a 2D material sample is around a few millimeters, the tip can easily miss this region if the sample holder slides too much. To solve this, the ramps are grooved to constrain the lateral displacement during tip approach and retrieve. The groove radius is 1/64” larger than the tungsten ball allowing us to translate the sample holder on the micrometer scale for repositioning the sample.

A Besocke-type scanner inherently has excellent thermal compensation which is ideal for STM inelastic electron tunneling spectroscopy (IETS). The travel range of the tip-sample distance is very limited by slip-stick motion of the sample holder. In our scanner, it can be adjusted to within 0.003”. This requires very tight tolerance both for the tip length and the distance from the ramp to substrate surface. The sample holder needs to be created with tight tolerances for a specific sample before being split into three pieces.

Figure B.1. Electrical wiring diagram of a Besocke-type scanner to perform an in-plane transport measurement simultaneously with out-of-plane tunneling experiment.

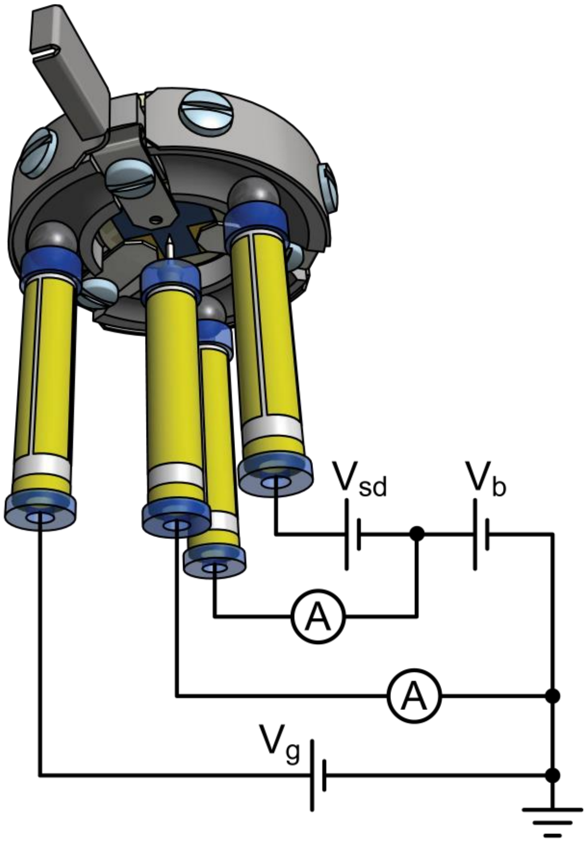
V_{sd}
V_b
A
A
V_g

Figure B.2. Mechnical drawings of the split sample holder assembly. (A) and (B) are the exploded views of a split sample holder from top right and bottom left to show how the components are stacked and assembled. (C) and (D) are the top view and bottom view of the final assembled sample holder.

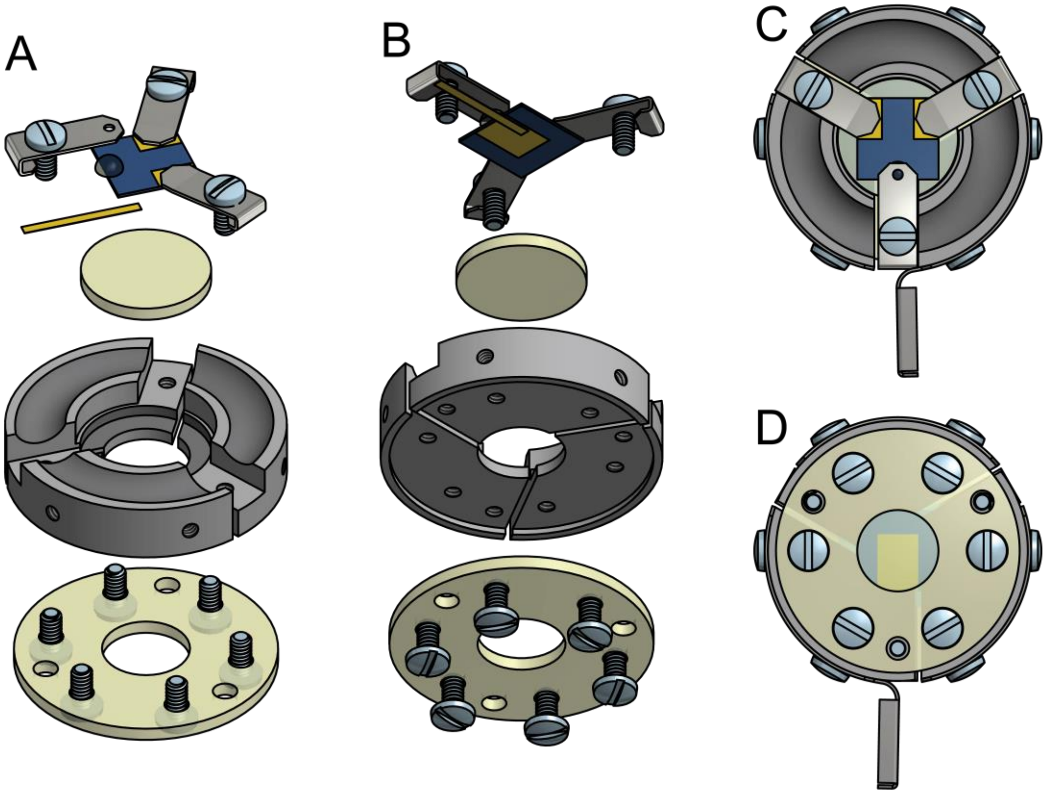
A
B
C
D

Figure B.3. Sample holder photos. (A) and (B) are the isometric views of a split sample holder from bottom right and top right respectively. This sample holder is not grooved and can be used for large 2D sample. (C) Top view of a sample holder with grooved ramps. (D) Normal sample holder with planar ramps.

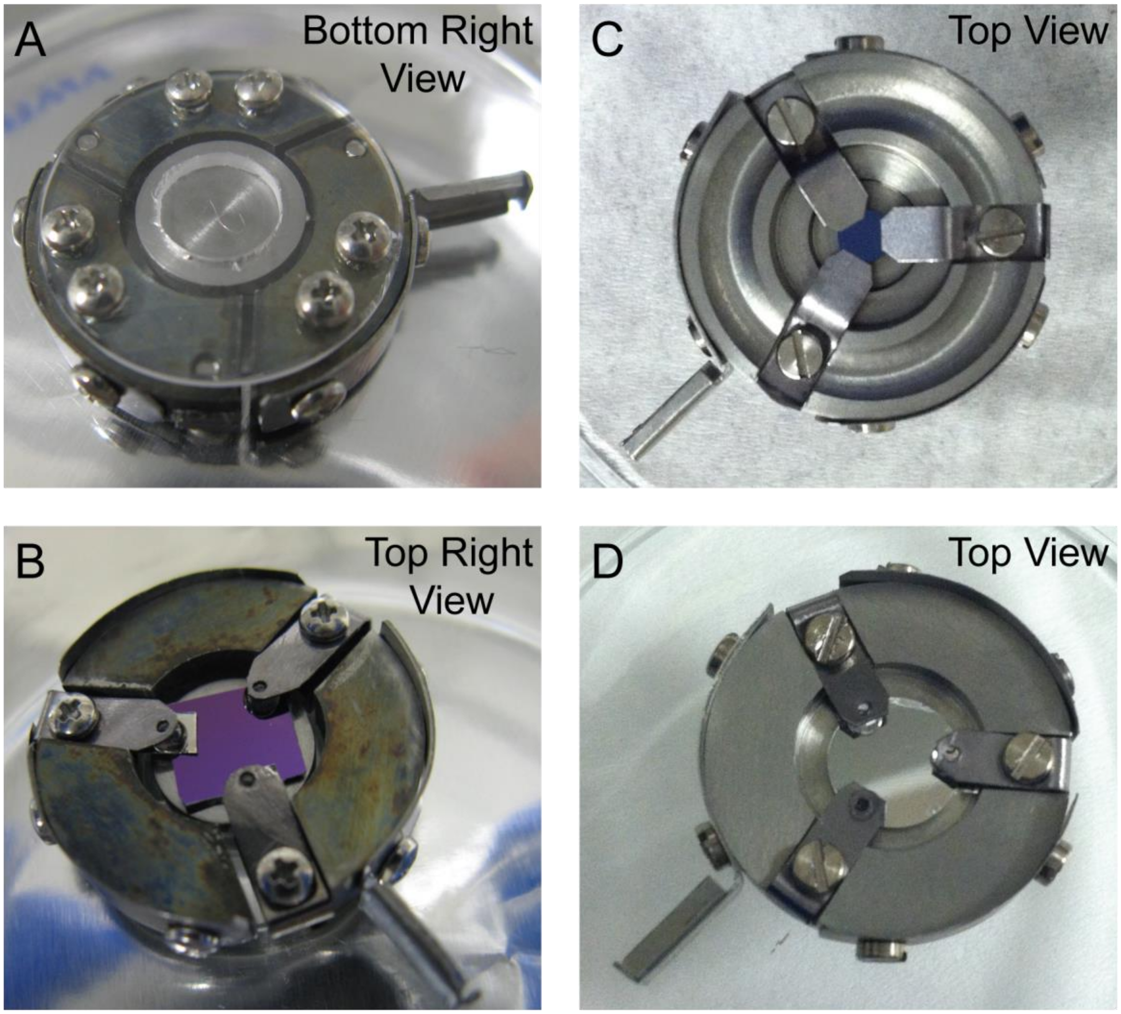
A
Bottom Right View
C
Top View
B
Top Right View
D
Top View

Bibliography

[1] B. C. Stipe, M. A. Rezaei, and W. Ho, Rev. Sci. Instrum. **70**, 137 (1999).

[2] K. Besocke, Surf. Sci. **181**, 145 (1987).